COMPLEX PLASMONIC BEHAVIOR IN ARCHIMEDEAN NANOSPIRALS

By

Jed I Ziegler

Dissertation

Submitted to the Faculty of the Graduate School of Vanderbilt University

In partial fulfillment of the requirements for the degree of

DOCTOR OF PHILOSOPHY

In

Physics

December, 2011

Nashville, Tennessee

Approved:

Richard F. Haglund, Jr., Department of Physics and Astronomy

David E. Cliffel, Department of Chemistry

Sandra J. Rosenthal, Department of Chemistry

Sharon M. Weiss, Department of Physics and Astronomy

Kalman Varga, Department of Electrical Engineering and Computer Science

ACKNOWLEDGMENTS

For providing the opportunity and shelter for my research, I would like to thank the Department of Physics and Astronomy and the Vanderbilt Institute of Nano Science and Technology (VINSE). Without the wealth of resources, personnel, and experience provided by these facilities, none of this work would be possible. I am also grateful for the time, direction, and constructive criticism that was generously offered by my Ph.D committee: Professors David E. Cliffel, Sandra J. Rosenthal, Sharon M. Weiss, and Kalman Varga. Furthermore, I thank my advisor, Professor Richard F. Haglund, Jr., for his patience, guidance, and support for my work, as well as the opportunity to freely explore and professionally grow in the direction of my choice. I would not be the physicist I am without his help.

I would also like to acknowledge the generous funding for this research, which was provided by the Office of Science, U.S. Department of Energy, under the grant number DE-FG02-01ER45916.

For their support, insight, and friendship, I thank those who helped shape my research and personal growth: Charles Adams, Joyeeta Nag, Davon Ferrara, Andrej Halabica, Kevin Tetz and Eugene Donev. For their guidance and generously offered knowledge, I thank Professors Tony Hmelo and Kirill Bolotin.

Finally, I want to thank my loved ones – my father, Dr. Herb Ziegler, my mother, Marilyn Ziegler, my sister, Kristin, and Brittany Caldwell – their tireless love and moral support pushed me forward through the successes and failures. Furthermore, I want to thank my parents for the example they set and for the intellectual aspirations that they instilled in me.

Thank you, all.

TABLE OF CONTENTS

Page

ACKNOWLEDGMENTS i

LIST OF FIGURES ii

Chapter

I. INTRODUCTION 1

1.1. Motivation..1
1.2. Exciting Particle Plasmon Resonances..2
1.3. Particle Plasmon Resonances in spherically symmetric systems 5
1.4. Symmetry breaking with elongation and protrusion 10
1.5. Symmetry breaking with ensembles 18
1.6. Symmetry breaking with arcs and bends 24

II. EXPERIMENTAL TECHNIQUES..30

2.1. Fabrication methods 31
2.2. Characterization techniques 34
2.3. Simulation techniques 37
  2.3.1. Finite-difference time-domain theory 38
  2.3.2. Simulation setup 42
  2.3.3. Analysis methodology 45

III. CHARACTERIZING THE LINEAR RESPONSE OF NANOSPIRALS 47

3.1. Characteristic near-field configurations 48
3.2. Tuning with the spiral winding number 57
3.3. Tuning with non-winding number parameters 62
3.4. Effects of array pitch and thickness 72
3.5. Conclusions 74

IV. QUANTITATIVE ANALYSIS OF NANOSPIRALS 76

4.1. Complications with spiral analysis 76
4.2. Path definition and interpolation 77
4.3. Figure of merit 82
4.4. Conclusion 86

V. POLARIZATION MODULATION IN NANOSPIRALS 88

5.1. Potential of polarization control 88
5.2. Rotating the linear polarization 89
5.3. Inward circular polarization 97
5.4. Outward circular polarization 102
5.5. Conclusion 105

VI. CONCLUSIONS AND FUTURE DIRECTIONS 107

6.1. Summary of characterization 107
6.2. Initial results for future work 108
    6.2.1. Competition between resonances 108
    6.2.2. Spatial locating via spectral modulation 111
6.3. Outlook 114

REFERENCES 115

LIST OF FIGURES

Figure		Page
1.1.	Schematic of optically drive, plasmonic oscillations ……………………	3
1.2.	Extinction spectra for nanospheres composed of various materials ……...	4
1.3.	Comparison between Mie theory and experiment ………………………..	6
1.4.	Energy-level diagram for plasmonic hybridization ………………………	7
1.5.	Extinction spectra for nanoshells of various inner and outer radii ………	9
1.6.	Extinction spectra for increasing nanodisk diameter ……………………	11
1.7.	Polarization dependent extinction spectra of a gold nanorod ……………	12
1.8.	Calculated extinction spectra of nanorods ………………………………..	13
1.9.	Calculated charge distributions and extinction spectra for nanocrosses ….	14
1.10.	Hybrid plasmon model applied to the nanostar ………………………….	15
1.11.	Calculated images of the electric field enhancements of a nanostar ……	17
1.12.	Extinction spectra for nanodimers with varied gap spacing ……………...	19
1.13.	Calculated electric field enhancement image for nanodimers ……………	21
1.14.	Calculated electric field enhancement image for nano-bowtie …………..	22
1.15.	Calculated scattering intensity profiles for a spiral array ………………...	23
1.16.	Calculated electric field enhancement images for a split ring ……………	25
1.17.	Simulated and experimental extinction spectra for split rings ……………	26
1.18.	Calculated electric field enhancement images of a S-shaped nanowire ….	27
2.1.	Scanning electron micrograph of a single nanospiral …………………….	31
2.2.	Scanning electron micrograph of over- and underdosed nanospirals …….	32
2.3.	Schematic of confocal extinction microscope ……………………………	36
2.4.	Visualization of a single Yee cell	40
2.5.	Simulated and experimental extinction spectra of nanospiral arrays …….	45
3.1.	Images of the three characteristic nanospiral configurations ……………	49
3.2.	Calculated extinction spectrum of a nanospiral array …………………….	50
3.3.	Comparison of the hourglass configuration to a chain of ellipses ……….	52
3.4.	Comparison of standing-wave configurations to nanorods ………………	54
3.5.	Line plot relating of effective mode area for nanospiral resonances ……	56
3.6.	Calculated electric field enhancement images of one nanospiral element ..	58
3.7.	Simulated extinction spectra for nanospiral arrays growing from 2π to 4π	59
3.8.	Plot of maximum field enhancement as winding number increases ……..	61
3.9.	Transmission spectra for different points within the array ………………	63
3.10.	Experimental extinction spectra for geometric parameters ………………	66
3.11.	Calculated extinction spectra for varied arm spacing and arm width ……	68
3.12.	Calculated extinction spectra for geometric tuning ………………………	69
3.13.	Calculated electric field enhancement images for nanospirals …………..	71
3.14.	Calculated electric field enhancement images for nanospirals …………..	72
3.15.	Simulated extinction spectra for arrays with increased array pitch ………	74
4.1.	Image of the index of refraction for a simulated nanospiral ……………..	78

4.2. Image of the edges of a nanospiral …………………………………….. 79
4.3. Calculated electric field enhancement image with edges marked ……….. 80
4.4. Comparison of line plots of the electric field enhancement ……………… 81
4.5. Comparison of σ to line plots of the electric field enhancement 84
4.6. Example of a hybrid focusing, standing-wave resonance ……………… 86
4.7. Line plot of the effective mode area for nanospiral resonances ………… 87
5.1. Simulated extinction spectra for rotated linear polarization …………….. 89
5.2. The hourglass configuration for different linear polarizations …………... 90
5.3. Maximum field enhancement for different linear polarizations ………… 92
5.4. Polarization mapping of the maximum field enhancement and extinction . 94
5.5. Experimental extinction spectra for different linear polarizations ……….. 95
5.6. Simulated extinction spectra comparing linear and circular polarizations . 96
5.7. The hourglass resonance excited by circular polarization ……………….. 97
5.8. Values of σ for right-handed circular and linear y-axis polarizations …… 98
5.9. Line plot and maximum field enhancements comparing right circular and linear y polarizations ……………………………………………………... 100
5.10. Experimental extinction spectra of linear and circular polarizations …….. 102
5.11. Values of σ for arrays excited by left-handed circular polarization ……… 103
5.12. Maximum field enhancement for left-handed circular polarization ……... 104
5.13. Line plots comparing linear and left-handed circular polarizations ……... 105
6.1. Extinction spectrum of a nanospiral array ……………………………….. 109
6.2. Normalized transmission spectra comparing single and dual peak excitation ……………………………………………………………… 110
6.3. Schematic of a nanospiral with position of PMMA nanodisks marked ….. 112
6.4. Calculated extinction spectra of a nanospiral with a PMMA nanodisk ….. 113

CHAPTER I

INTRODUCTION

1.1 Motivation

As technology advances, there is a general trend toward reduction of scale; currently this trend places the focus of new technologies in the nanometer scale, where interfaces and single molecules are dominant. Particle plasmon resonances are a resonant optical-coupling phenomenon that couples electromagnetic fields into nanoscale regions at otherwise impossible conversion efficiencies. These resonances couple photons to the free-electron gas of sub-wavelength, metal nanoparticles (NPs) and confines the resulting electric field enhancements into regions as small as single cubic nanometers. The diversity of plasmonic behaviors exhibited by a NP is strongly dependent on a number of factors, but the particle geometry presents the largest degree of control with the greatest diversity of excitable mechanisms. Specifically, breaking the geometric symmetry of a NP utilizes different coupling mechanisms to provoke additional resonances and unique spatial organization of the electric field enhancements.

Utilizing both simulations and experiments, I will describe and analyze the Archimedean spiral, which presents previously unobserved plasmonic behaviors. The combination of completely broken symmetry, smooth geometric organization, and nearly-circular structure produces a large number of distinct, complex plasmonic resonances with widely varying, functional near-field configurations generated by a number of distinct and incompatible mechanisms.

As an introduction to complex plasmonic geometries the following sections will focus on the correlation between increasing geometric complexity and the evolution of plasmonic behavior. Specifically, the focus will be on the effect of growing complexity of the lateral geometry of NPs that have been fabricated on solid substrates. Due to the complexity of the PPR mechanism, most analyses of PPRs of the various geometries must either be qualitative, restricted to special cases, or analytically derived from solving Maxwell’s equations for a discretized volume, which contains the particle. The specific methodology for these analytical solutions is covered in chapter 2, but for highly symmetric systems the model can be reduced to analytical equations that describe the spectral position and extinction intensity of the PPRs for the NP. The discussion of plasmonic behavior will begin with spherically symmetric system, which have the necessary high symmetry, and progress to highly complex geometries.

1.2 Exciting Particle Plasmon Resonances

Among the mechanisms and materials whose properties become significant at the nanoscale, particle plasmon resonances (PPRs) produced on metallic nanoparticles (NPs) are among the most promising and have attracted significant interest within the scientific community. For NPs with geometric dimensions much smaller than the incident wavelength, the incident light interacts with the NP as a quasi-static electromagnetic field. At specific wavelengths defined by the physical properties of the NP and its local environment, the polarizability α of the NP experiences a resonant enhancement. These wavelengths couple resonantly with the conduction electrons in the NP, forcing them to accumulate at an edge of the nanoparticle, as visualized in figure 1.1. This accumulation generates an electric dipole within the NP with an enhanced negative field from all conduction electrons at one edge and a similarly enhanced positive field at the opposing edge generated from the exposed, almost immobile ionic cores. The ionic cores exert a restoring force on the polarized electrons that, in turn, generates a resonant oscillation.

This resonant behavior results in two physical phenomena, one that is observable in the far field, $r >> \lambda_{res}$, and one that is confined to the near field region, located no more than tens of nanometers away from the NP surface. In the far field, the increased coupling between the NP and the incident beam increases the scattering and abortive coefficients. Together, these quantities describe the optical extinction due to the NP. In the near field (NF), the accumulation of the conduction electrons at the edges of the NP produces regions of massive induced electric fields. These fields, enhanced above those that exist without the driving field, are non-radiative and are confined to the NF of the NP. For the purposes of this work, the location of these regions on the NP surface and the degree of their enhancement will be referred to as the near-field structure (NFS).

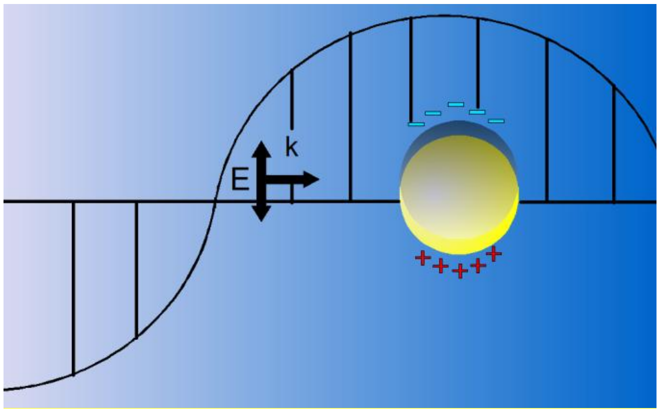

Figure 1.1: Schematic of optically driven, plasmonic oscillations.

The spectral characteristics and NFSs of the PPRs are governed by the size, shape, composition and surrounding environment of the NP.[1-3] The polarizability, which is defined by the dielectric function of the NP and its surrounding environment, establishes the maximum energy of the PPRs. Figure 1.2a shows how this limit defines the resonance of different types of metallic NPs in water. Increasing the value of the index of refraction for the surrounding dielectric decreases the restoring force on the electrons and red-shifts the spectral position of the resonance.

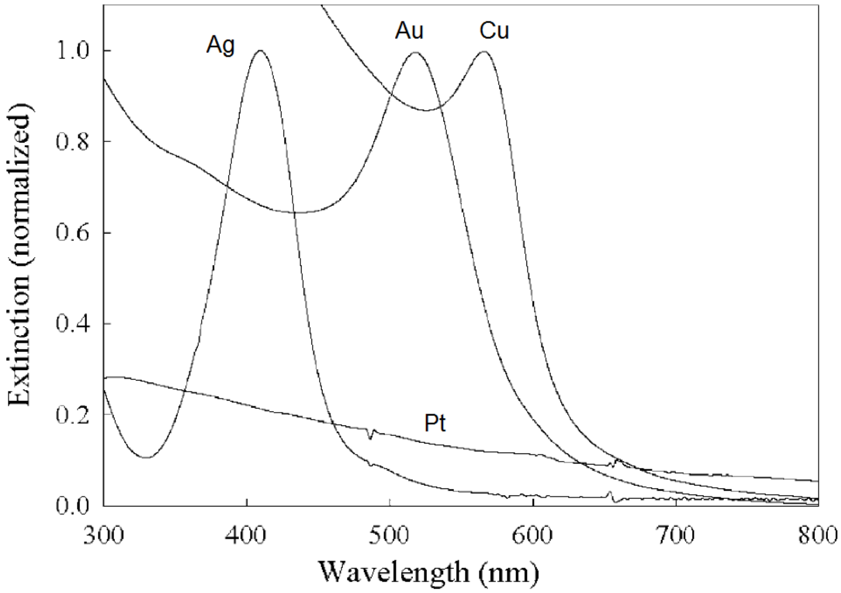

Figure 1.2: Extinction spectra for colloidal nanoparticles composed of Ag (diameter = 20nm), Au (diameter = 12nm), Cu (diameter = 12nm), and Pt (diameter = 8nm) in water. Figure from [4].

The last two governing parameters— scale and shape — of a plasmonic NP are geometric, which have received significant attention due to the large range over which the spectral and spatial features can be tuned. Together, these features can introduce significant spectral shifts for all resonances and more complex plasmonic behavior, such as additional resonances and more complicated, (*i.e.* non-dipolar) spatial configurations of the field enhancements.

1.3 PPRs in spherically symmetric systems

Spherical symmetry affords a massive simplification of the PPR phenomenon by allowing the entire NP to be treated as a single resonant dipole. For NPs much smaller than the driving field (r <<100nm), simple electro-statics can accurately approximate the plasmonic response of a nanosphere.

For particles larger than 50nm, the quasi-static approximation begins to fail due to differences in the phase of the driving field at different locations in the particle and retardation due to self-induced fields. Gustav Mie[5] presented a complete theory for large nanospheres by dividing the electromagnetic field into spherical multipoles and scattered field to define the light scattering and extinction of spherical NPs:

$$\sigma_{ext} = \frac{2\pi}{|\mathbf{k}|^2}\sum_{j=1}^{\infty}(2j+1)\mathrm{Re}\left(a_j + b_j\right) \tag{1.2}$$

$$\sigma_{sca} = \frac{2\pi}{|\mathbf{k}|^2}\sum_{j=1}^{\infty}(2j+1)\left(\left|a_j\right|^2 + \left|b_j\right|^2\right) \tag{1.3}$$

where σ_{scat} and σ_{ext} are the scattering cross-sections for the scattering and extinction, respectively for driving fields with wave vector k. The terms a_j and b_j are

$$a_j = \frac{m\psi_j(mx)\psi'_j(x) - \psi'_j(mx)\psi_j(x)}{m\psi_j(mx)\eta'_j(x) - \psi'_j(mx)\eta_j(x)} \tag{1.4}$$

$$b_j = \frac{\psi_j(mx)\psi'_j(x) - m\psi'_j(mx)\psi_j(x)}{m\psi_j(mx)\eta'_j(x) - m\psi'_j(mx)\eta_j(x)} \tag{1.5}$$

where $m = n/n_m$ with n and n_m the index of refraction for the particle and the surrounding medium, respectively, $x = |k|r$ is a size parameter defined by the NP radius, r, and ψ, η

and ψ', η' are the cylindrical Riccati-Bessel functions and their derivatives with respect to the argument in parentheses, respectively. The index j labels the multipole order, which for a sphere is j = 1. Higher harmonics do exist but the high geometric symmetry limits the spectral response to the dipole resonance. Plasmonic resonances that are not optically excitable are referred to as *dark resonances*.

The agreement between these cross sections and experimental results for Au NPs of different sizes is shown in figure 1.3. This illustrates the applicability of Mie theory for analytically describing the far-field behavior of these highly symmetric systems, but this theory only extends to spheres. Ellipsoids can be treated by expanding the radial parameter to $r_a \neq r_b \neq r_c$ and then recomputing the cross sections, but for particles fabricated on substrates, which become flattened with sharper edges, or particles with reduced geometric symmetry, these approximations become far too complicated.

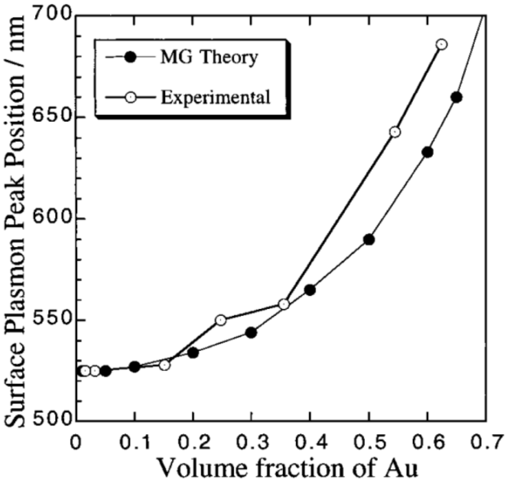

Figure 1.3: Peak positions for resonances from a face-centered cubic lattice of 13nm gold NPs embedded in a SiO2 film with increasing packing density. The filled dots represent experimentally acquired data and the white dots represent peaks positions calculated from Mie theory. Figure used from [6].

The complication of reduced symmetry mandates a rigorous application of Maxwell's equations using complicated and computationally intensive algorithms to simulate the plasmonic response for most geometries. However, it has been shown that the energy of PPRs generated from complex geometry can be calculated by a method similar to that used to calculate energy levels in molecules. [7] This methods, named the hybridized plasmon (HP) method computes the energies of complex PPRs using the prior knowledge of energy levels of multiple, simpler geometries that, when combined produce the more complex geometry. An example is the nanoshell, which can be decomposed into a void in a metallic surface and a nanodisk (figure 1.4).

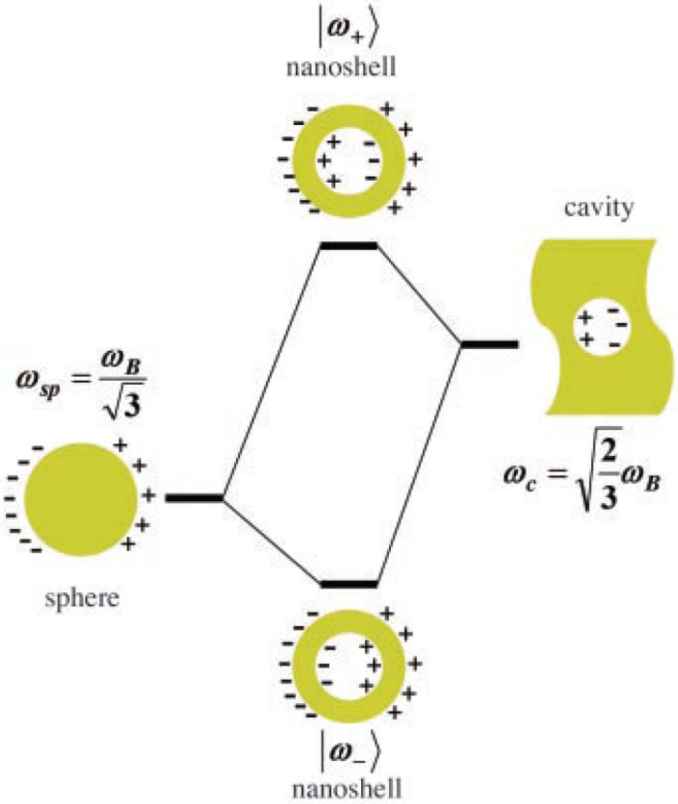

Figure 1.4: An energy-level diagram of a hybridized nanoshell and its constituent geometries describing the plasmon hybridization method. The two nanoshell plasmons are an antisymmetrically coupled (antibonding) ω_+ plasmon resonance and a symmetrically coupled (bonding) ω_- plasmon resonance. Figure used from [7].

The nanoshell retains spherical symmetry but the void in the center adds an interface where plasmonically induced surface charge collects. Independently, the two constituent structures have a well-characterized plasmonic response, defined by a single dipole resonance. When the two structures are in close proximity, their respective resonances couple; the coupling strength will be a function of their separation. This intra-particle coupling hybridizes the plasmons, similar to molecular hybridization, resulting in a pair of symmetrically and anti-symmetrically coupled plasmon resonances, which are designated as bonding and anti-bonding resonances, respectively. These two states relate to the relative phase of the plasmonic oscillation for each constituent structure. The spectral position of these resonances is modulated by the degree of coupling, which can be tuned by changing either the inner or outer shell radius without reducing the symmetry of the system. The lower-energy bonding resonance is easily detectible in the extinction spectrum, as shown in figure 1.5, but the high-energy, anti-bonding resonance is usually much weaker and broader due to interband transitions in the gold. Due to these complications, the anti-bonding resonance is not experimentally detected for NPs smaller than 200nm in diameter.

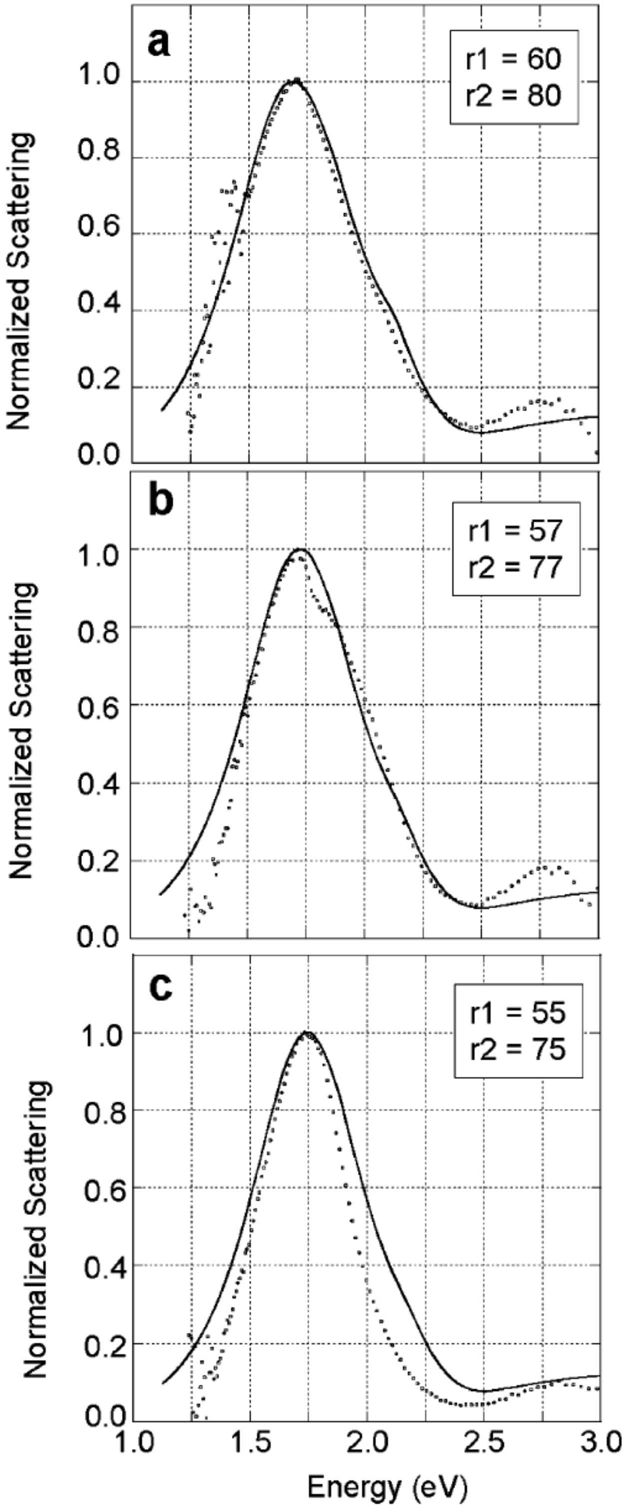

Figure 1.5: Measured and calculated scattering spectra for single nanoshells in water on ITO substrates. Calculated spectra were generated by Mie theory assuming n = 1.33 for the surrounding medium. Inner and outer radii for each nanoshell are displayed in the figure. Figure used from [8].

The HP model is a highly adaptable method for determining resonances in complex NPs, but there is a fundamental limit set by the requirement of a decomposable geometry. Only geometries with multiple surfaces, referred to as multiply connected, can be decomposed into distinct simple geometries. This limitation excludes a number of geometric categories, including those generated by protrusion or elongation, such as stars, crosses or rods, and geometries with curvature, such as half-shells and bent or wound ribbons. Without the HP model, the mechanisms that produce additional resonances must be considered separately. Furthermore, the HP model does not describe the NFS of a resonance, rather it assumes simple harmonic oscillations that occur across the entire geometry. In the following sections, the geometries and mechanisms that produce these more complex plasmonic responses will be discussed phenomenologically, while acknowledging those geometries to which the HP model can be applied.

1.4 Symmetry breaking with elongation and protrusion

Progression from spherical to more complex geometries requires a brief consideration of how NPs are produced. Chemical synthesis methods produce three-dimensional structures, such as cubes, ellipsoids, and stars[9], while lithographic methods primarily produce two-dimensional structures with a finite thickness. In both cases, progressively reducing symmetry begins with elongation or compression along a single axis. For three-dimensional geometries, this produces the nanoellipsoid; for two-dimensional shapes, this produces the rectangular prism, or nanorod, or nanodisk. The plasmonic behavior is defined by the geometry as it appears normal to the incident beam, so each dimensionality is similar. This work is focused on lithographically fabricated structures; therefore this introduction will favor discussion of two-dimensional shapes, beginning with the reduction of symmetry from a circular nanodisk to a nanorod.

The plasmonic response of a nanodisk illuminated normal to its face is similar to that of the nanospheres. As the NP diameter increases, the dipole resonance red-shifts (figure 1.6) just as the PPR of the nanosphere red-shifts with increasing diameter. This red-shift is related to increased non-radiative damping and more rapid dephasing of the plasmon oscillation due to an increase in electron collisions and scattering over the longer distance. Also similar to the nanosphere, the spatial organization of the NF (the near-field structure, or NFS) comprises large field enhancements on the edges of the disk parallel to the polarization of the incident beam.

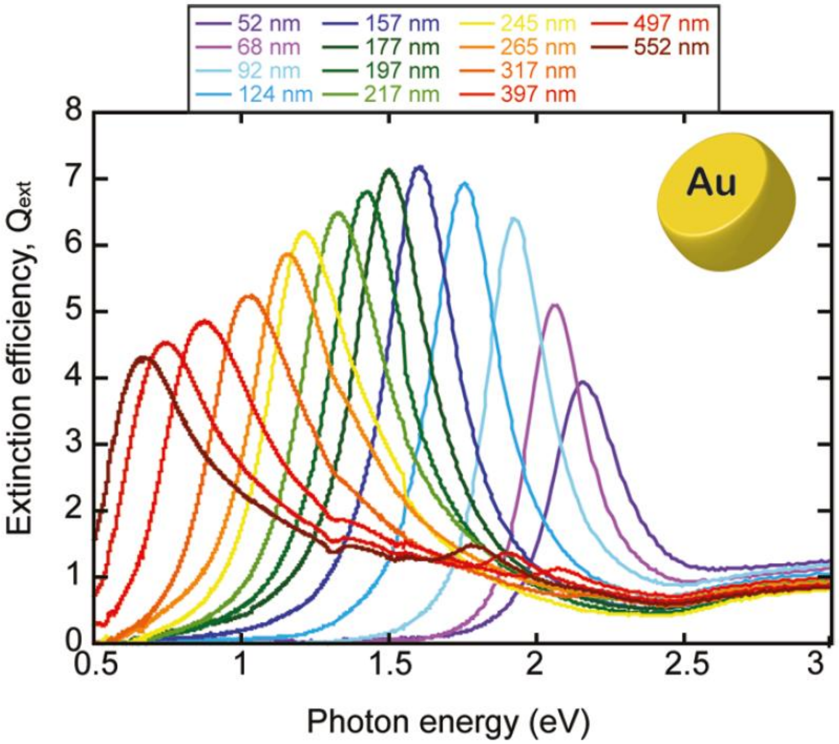

Figure 1.6: Measured extinction spectra for 20nm thick nanodisks with increasing diameter. Figure used from [10].

Progressing from the nanodisk to the nanorod, the anisotropy of the rectangular shape generates a polarization dependence on the plasmonic behavior.[11] Polarization parallel to the short axis excites a resonance whose spectral position and linewidth is similar to that of a nanodisk of a similar diameter. The long axis generates a strongly red-shifted resonance, with a significantly narrower linewidth and higher intensity. Figure 1.7 displays this behavior for a nanorod with a 4:1 aspect ratio and width of 11nm.

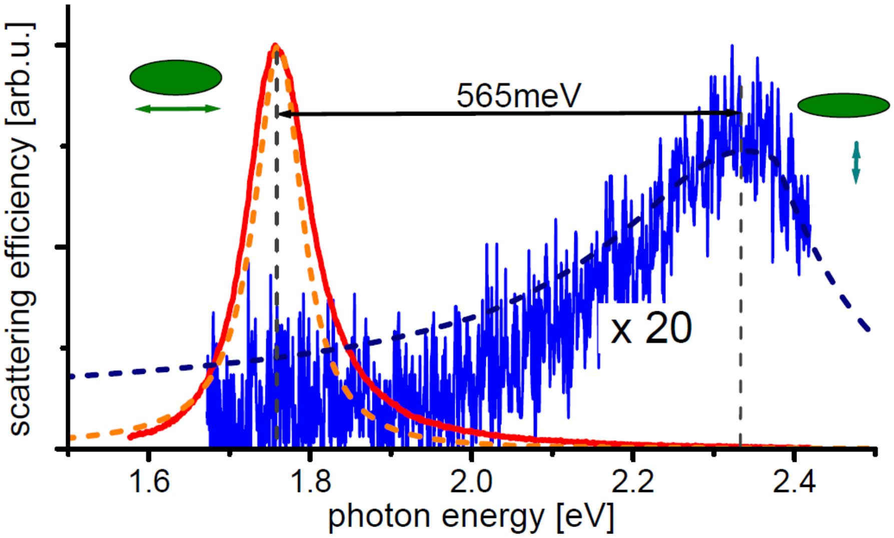

Figure 1.7: Polarized scattering spectrum of nanorods with a 2.9:1 aspect ratio. The calculated (dashed lines) and experimental (solid lines) spectra of the short axis (blue lines) are multiplied by a factor of 20 compared to the long axis (red lines). Figure used from [12].

As the aspect ratio of the ellipse increases, the short axis resonance blue shifts slightly and the long axis red-shifts. Furthermore, the lineshape of the long axis sharpens while the short axis slowly broadens. The relation between the geometric extension of the NP, on one hand, and the lineshape and spectral shift, on the other, arise from the same mechanisms as those that cause the red-shift with increasing nanodisk radius. However, unlike the nanodisk, the excited plasmon modes depend on polarization: the short-axis mode goes dark for light polarized along the perpendicular axis. For the long-axis resonance, the PPR red-shifts with increasing aspect ratio, making it possible to tune resonances to wavelengths that would require micron scales in a circular geometry. Furthermore, the spectral linewidth of the resonance narrows due to increased polarizability, which decreases the dephasing time of the plasmon oscillation.[13] The effect of increased aspect ratio on the long axis resonance, with the short axis remaining constant, is displayed in figure 1.8.

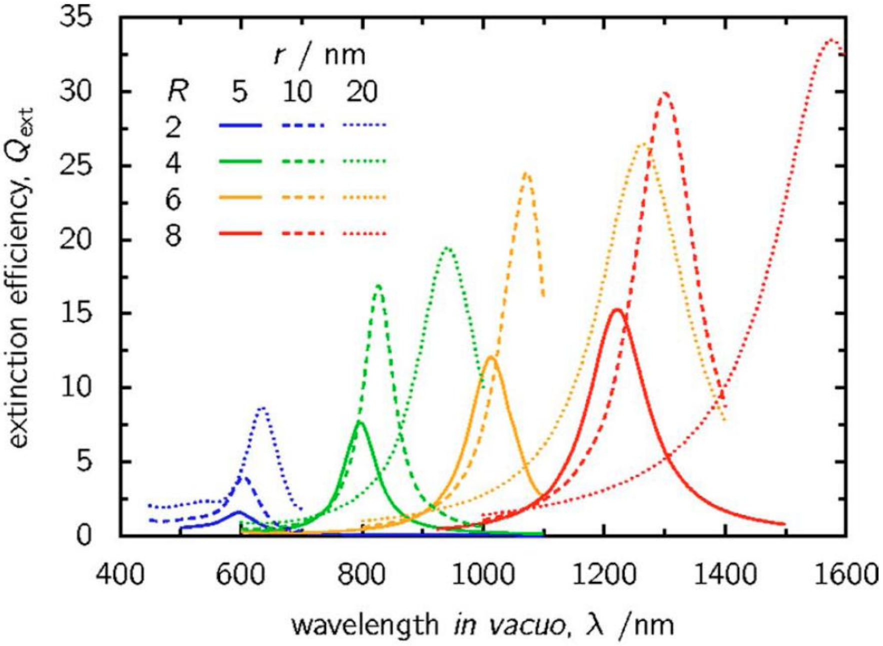

Figure 1.8: Calculated extinction spectra of the longitudinal resonances for nanorods of differing widths, r, and aspect ratios, R. Figure used from [14].

This technique of increasing the number of resonances by reducing symmetry can be extended by creating more branched features of different lengths. However there exists a limit as the new features and protrusions begin to crowd together. Beyond this limit, geometric features become convoluted with the body of the NP, and lose their unique contributions to the spectral features of the PPR. The nanocross demonstrates the convolution of resonances from the cross composed of two and three nanorods, excited by light polarized as shown in figure 1.9.[15] Here the structure allows for different phases of the plasmonic oscillations at the different tips, but the symmetry of the system darkens the higher energy resonances. Only when the symmetry is further broken by off-normal illumination are the selection rules relaxed to allow excitation of the alternative resonances.

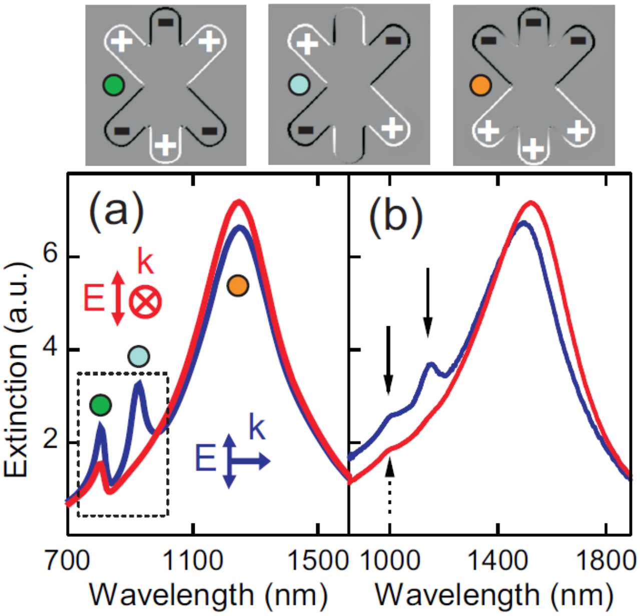

Figure 1.9: Calculated charge density distributions of the two antisymmetric modes (two top left panels) and single symmetric mode (top right panel) of the cross made of three nanorods. a) Simulated and b) experimental extinction spectra for the system. The red line represents normal incidence and the blue represents illumination from the side. Figure used from [15].

The HP model cannot be applied to the nanocross since the individual arms are not associated with distinct resonances, but instead are incorporated into the collective oscillations of the PPR. However, the HP model can be applied in some specialized cases, such as the nanostar.[9] As shown in figure 1.10, nanostars can be broken into a set of tips associated with oscillations along different axes, depending on the incident polarization, and a core. The unique lengths and widths of the different tips determine the possible resonances that can hybridize with the core.

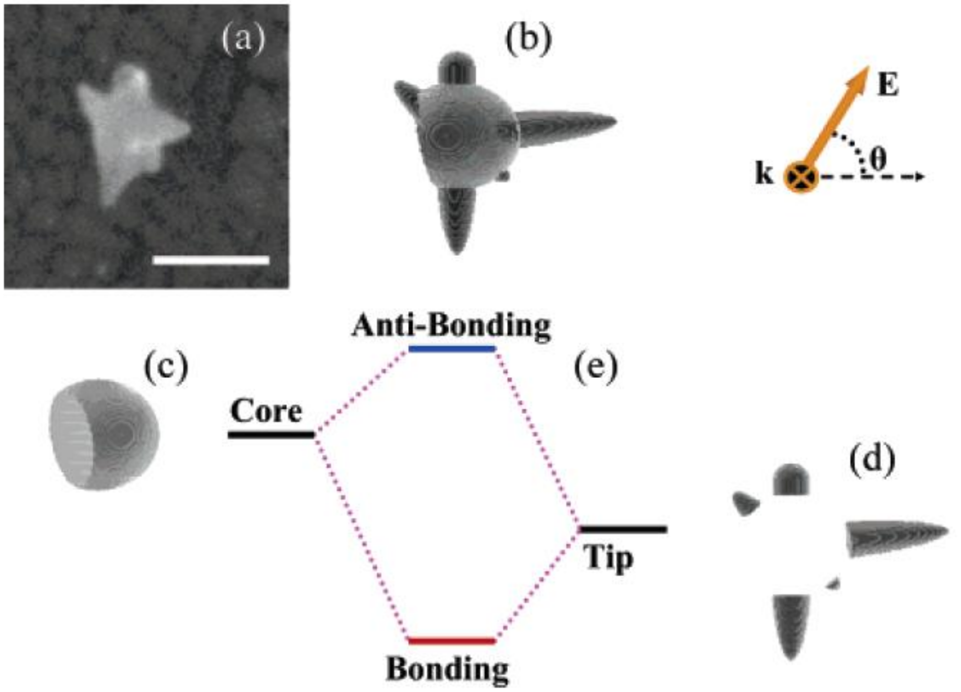

Figure 1.10: a) Scanning electron micrograph of a nanostar. The scale bar is 100nm. b) A graphically generated image of the nanostar. c-e) An energy diagram of the decomposed nanostar into c) a core and d) the tips. Figure used from [9].

This decomposition into a basis set comprising a core and tips demonstrates how breaking symmetry in this fashion can be used to construct a basis set of structural elements that affect the plasmonic spectral response through hybridization. In these branching structures, an additional mechanism is observable in the NFS (figure 1.11). This mechanism, known as the “lightning-rod effect” [16, 17], is generated when the field lines at one pole of an oscillation are highly compressed by a small radius of curvature. This effect is also observed in geometries such as nanotriangles [18-21] and nanoellipses with high aspect ratios [13, 22] and presents a number of applications for techniques such as surface enhanced Raman spectroscopy and PPR sensors.

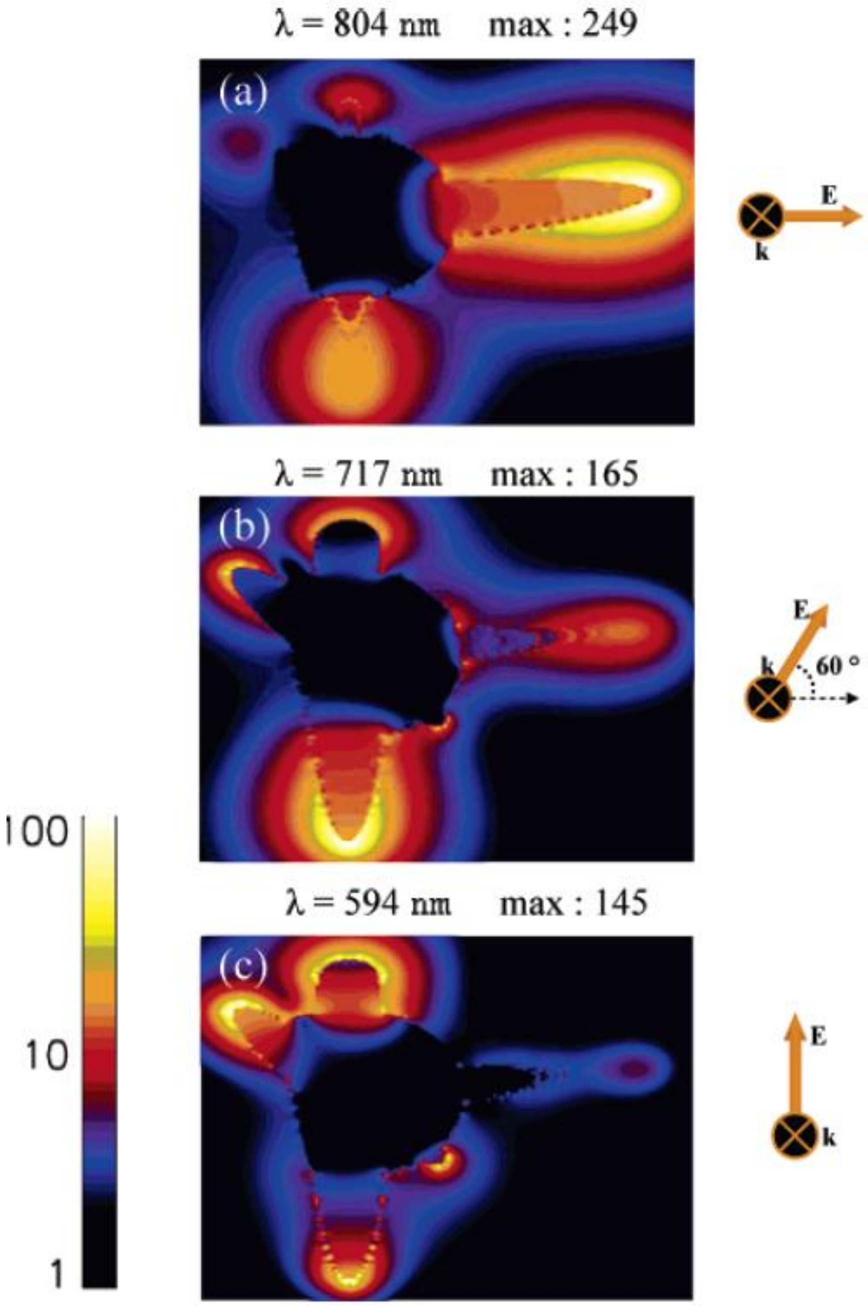

Figure 1.11: Calculated images of the electric field enhancements for the nanostar at the a)804nm, b) 717nm, and c) 594nm resonances. The polarization angles are indicated to the right of the relevant image. The maximum field enhancement for a single point is indicated above each image. Figure used from [9].

1.5 Symmetry breaking with ensembles

The method of adding protrusions to generate complicated plasmonic responses can be extended until the NP has no geometric symmetry, but the lack of order produces extreme convolution as a side effect. As a result these systems have few excitable resonances and simple multipole NFSs. To expand beyond simple multipole NSFs and a limited number of resonances, ensembles of NPs can be placed in close proximity where the mechanism of inter-particle coupling and multiple geometries with distinct plasmonic responses present a larger array of resonances and NFSs.

The simplest ensemble is the homogenous dimer composed of two metallic nanodisks. When NPs are separated by distances comparable to the wavelength of the individual NP resonances, long-range far-field coupling occurs.[23-28] The mechanism governing far-field coupling is similar to that of diffraction gratings, with a preferred wavelength defined by the spacing. For plasmonic array coupling, the array pitch defines a preferred resonance toward which all NP resonances shift and which, if they overlap, generates an enhancement. For NP spacing that is equal to, or less than, the diameter of the NPs, NF coupling dominates the plasmonic response.[29] The strength of this coupling is strongly dependent on separation distance (figure 1.12). For NP spacing between these two limits, both mechanisms must be considered.

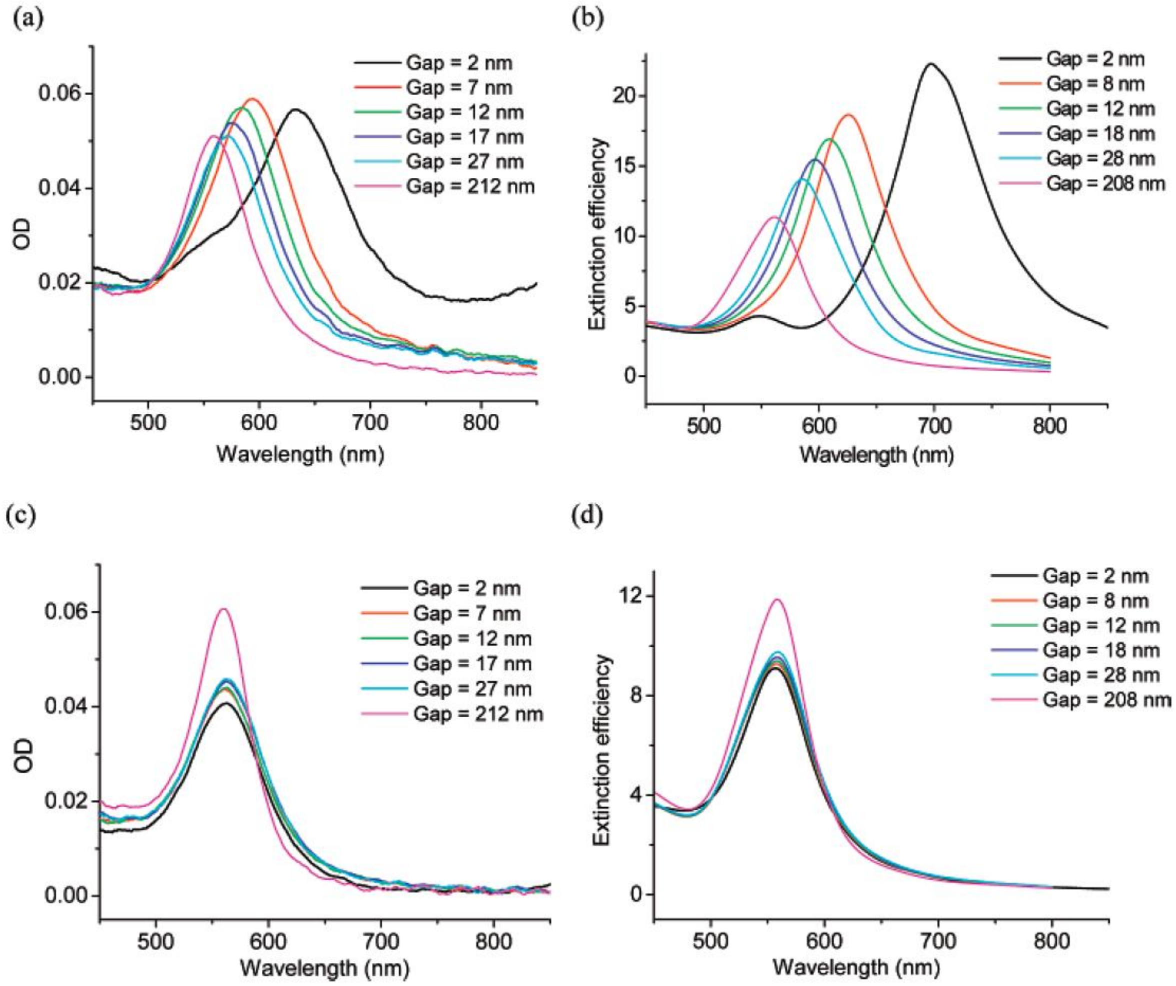

Figure 1.12: Spectra of dimers composed of nanodisks with a diameter of 88nm and a thickness of 25nm. a,c) Experimentally acquired absorption spectra and b,d) simulated extinction spectra were taken for polarizations a,b) parallel and c,d) perpendicular to the dimer axis. Figure used from [29].

For dimers with separations much smaller than the resonant wavelength, the coupled resonances hybridize in a manner similar to the void-plus-sphere of the nanoshell. Applying the hybrid plasmon model to the dimer system, four resonances are formed by the coupling of the dipole resonances of each disk, two parallel (→ → and ←→) and two perpendicular (↑↑ and ↑↓) to the dimer axis (long axis). [30, 31] Only the lower-energy bonding resonances are excitable at normal incidence. Since the net dipole moment is equal to zero, the higher-energy, antibonding resonances remain dark without additional symmetry breaking. As the separation is increased, the coupling decreases and the bonding and anti-bonding separations increase, with the bright bonding resonances red-shifting and the dark resonances blue-shifting.

To increase the excitable complexity of the system, the symmetry must be broken further. This can be achieved with either heterodimers or multimers, both of which will be briefly discussed. Heterodimers can include different materials [32, 33] or sizes [34] with the same geometry or different geometries. The former simply brighten some of the dark resonances, so the treatment above describes the interaction sufficiently. The latter can add a new dimension to the coupled system, either with increased resonances or more complicated NFSs. Plasmonic hybridization results in a significant increase in the number of non-degenerate, excitable resonances when lower symmetry NPs, such as nanorings [35], are coupled. NF coupling can also be used to enhance the focusing feature of the individual geometries. All NF coupling results in a field enhancement within the gap betweem the NPs (figure 1.13a), but using focusing geometries, such as triangles (figure 1.13b), can significantly increase this enhancement. Adding different orientations of the same geometry [36] or alternate geometries [37] also breaks the symmetry of any of the constituent NPs, resulting in hybridization.

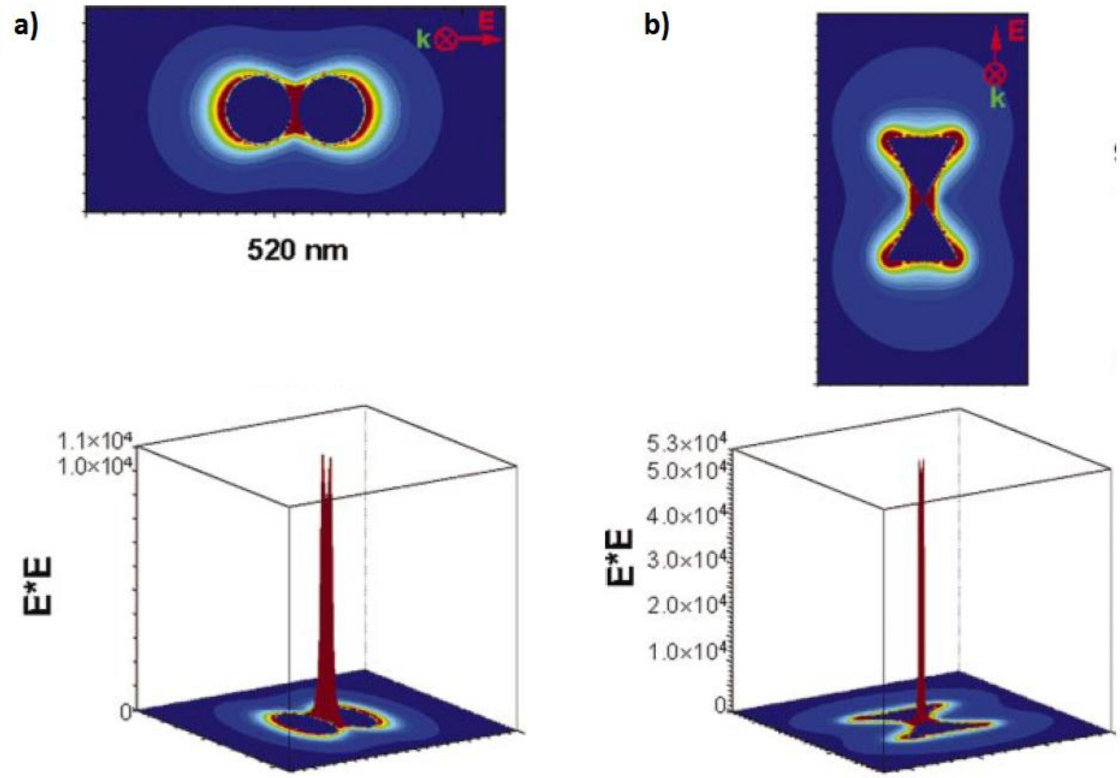

Figure 1.13: a) Electric field enhancement image of a dimer of 36nm silver spheres separated by 2nm. This resonance is excited along the dimer axis at 520nm. b) Electric field enhancement image of a dimer of 36nm silver equilateral triangular prisms (side length=60nm, thickness 12nm) separated by 2nm. This resonance is excited along the dimer axis at 932nm. Figure used from [22].

Coupling larger groups of NPs can expand this behavior and, unlike single particles that convolute and darken resonances as the complexity increases, these larger systems can generate a large number of resonances from hybridization between the numerous constituent structures. [38] However, the NFS is still limited to primarily dipole and quadrupole configurations due to the symmetry of the ensemble. This limitation can be overcome by breaking the symmetry formed by the placement of the constituent elements. A simple example of this technique is observed in ensembles, such as the heptamer [39] or ring-disk [40] system, with the central NP slightly offset from the coordinate system of the other structures. In these systems, the broken symmetry shifts bright high-energy resonances over dark, higher order harmonics, generating Fano resonances and exciting new NFSs.

Reducing symmetry by random reconfiguration will produce some additional phenomena, but spatially organized placement generates tailored behavior for specialized applications. Basic examples include plasmonic lenses made of self-similar nanodisks of decreasing size [41] or bowties composed of crossed nanotriangles with a single element offset.[42] These structures focus plasmonic energy into a predefined region, as shown in figure 1.14 for the offset nano-bowtie. This form of organization lends to applications such as NF couplers to/from quantum dots or luminescent proteins.[43]

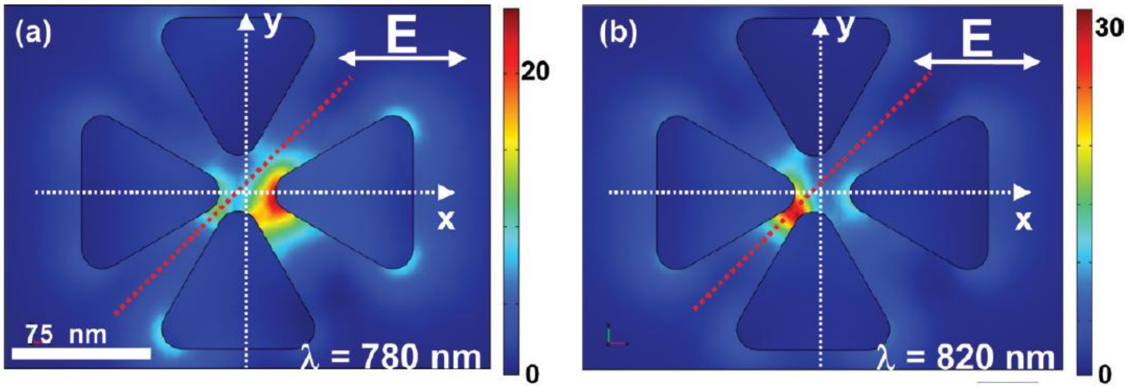

Figure 1.14: Calculated electric field enhancement images of a nano-bowtie with symmetry broken by shifting the vertical bowtie by (x,y) = (-5nm, +5nm) excited at the resonances located at a) 780nm and b)820nm. Figure used from [42].

This method can also be applied to an entire array of NPs using deterministically aperiodic spacings. By alternating the inter-particle spacing in an irregular organized pattern, the resonant spectrum and NFS can be fully controlled over an extended lateral surface. By continuously varying the spacing throughout the array, a white-light continuum absorber can be produced.[44, 45] Alternatively, by breaking the square lattice structure, ensemble shapes can be formed for specialized purposes, as in the example of the spiral array. As shown in figure 1.15, an array of nanospheres organized into a Vogel spiral is able to produce multiple optical vortices at 10μm above the array.[46]

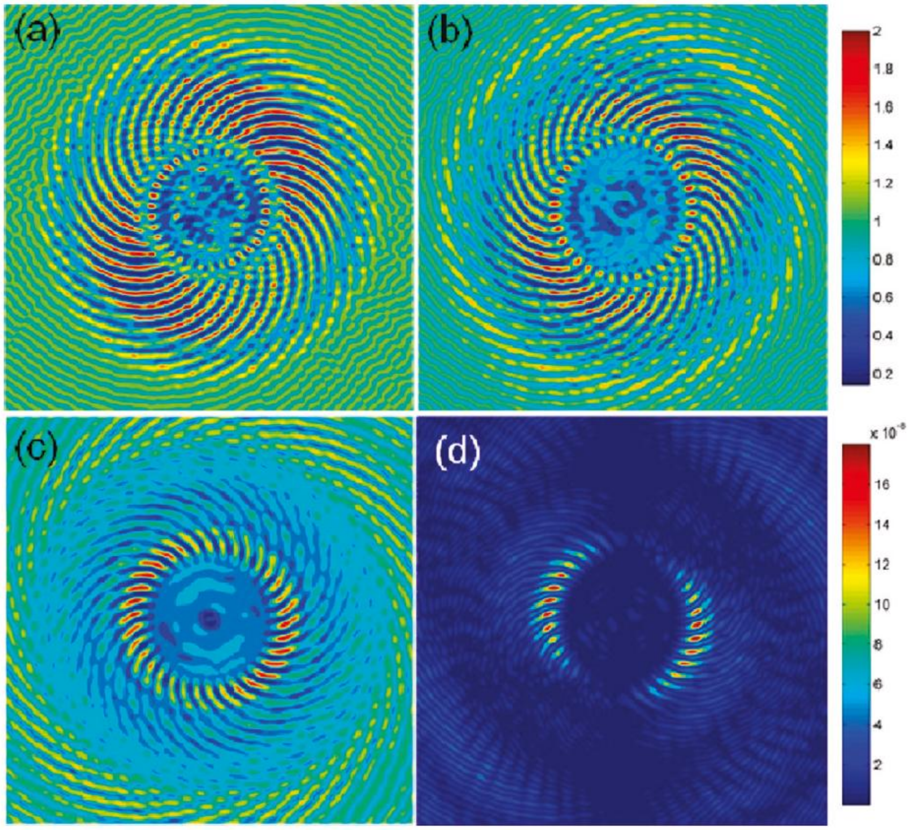

Figure 1.15: Calculated scattering intensity images of an array of 1500 gold nanospheres with 200nm diameter organized into an α_2-spiral. The array was excited by linearly polarized light at its 650nm resonance. Scattered intensity profiles are calculated at a) 1, b) 3 and c) 10um from the plane of the array. d) Image of the magnitude of the azimuthal component of the pointing vector normalized to c^2 at 10um above the array plane. Figure used from [46].

Considered together, ensemble systems demonstrate a diverse potential potential for applications due to their easy spectral and spatial tuning, multiple resonances, and access to a wide variety of mechanisms. However, the price of this expanded diversity is a significantly enlarged surface area that excludes applications that require compactness and a NFS that is limited by the complexity of the constituent NPs. To preserve the advantages of ensemble systems while remaining laterally compact a new facet of symmetry breaking must be explored. This new facet uses arced or bent geometries to break symmetry while retaining a holistic order and prompting intra-particle coupling.

1.6 Symmetry breaking with arcs and bends

Symmetry breaking with arced structures, such as split rings, S-shapes and spirals, has a unique advantage over symmetry breaking that uses linear perturbations and branching. By winding a NP on itself, controlled intra-particle coupling occurs between sections of the structure that are significantly separated along the path of connection. Furthermore, neighboring, but unconnected, sections of a NP generate gaps where preferred coupling occurs, which adds features to the NFS of a resonance that are not multi-polar. A simple example of this is the nanoscale split ring.

The split ring has nearly circular symmetry that makes much of its behavior comparable to the nanoring, with the exception of the gap at one point. Similar to the nanoring, the split ring supports multiple resonances and a large surface area, normal to the incident light, which enhances the extinction coefficient of resonances. Furthermore, the NFS of the nanoring is similar to the split ring, when the polarization of the incident light is parallel to the gap. However when the polarization is aligned perpendicular to the gap spacing, in the near field the gap acts as an intra-coupling feature with the same coupling strength and NF enhancement as that of a closely spaced dimer (figure 1.16).[47]

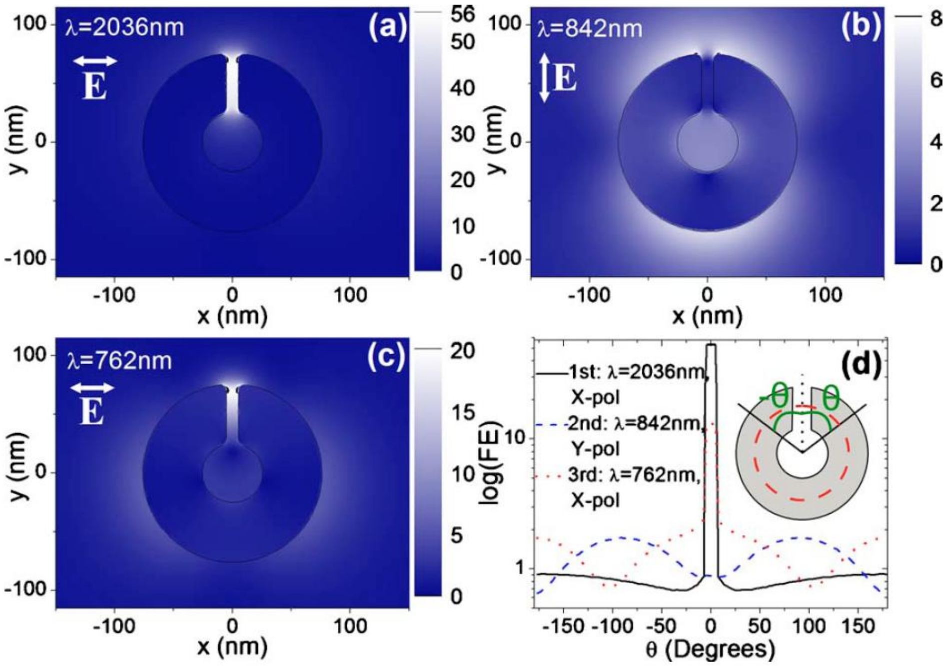

Figure 1.16: Image of the NF enhancements for the split ring with a gap of 10nm at the three bright resonances: a) 2036nm, b) 842nm, and c) 762nm. The white arrows indicate the polarization that excites each resonance. d) Line scan of each resonance as a function of angle along a circle of radius equal to the center of the split ring. Figure used from [47].

The concept of specialized locations within a larger structure is a key feature of arcing geometries that can be replicated and expanded to increase the complexity of the NFS and extinction spectrum. Furthermore, these geometries present multiple methods to tune the spectral and spatial response by modifying the gap.[48-51] For the split ring, decreasing the gap size between fully cut edges results in a red shift of the primary peak similar to the tuning of a dimer.[48] However, as the gap closes a second resonance becomes excitable for light polarized parallel to the gap.(figure 1.17) This is a response to the near-circular symmetry of the closing gap. The gap can also be gradually broken by offsetting the void in a nanoring. This method adds Fano resonances as the low energy dipole resonance broadens and shifts to overlap higher order multipoles. Also, the narrowed region compresses the electron oscillations, resulting in a significantly increased NF enhancement similar to the lightning-rod effect, without the structural weakness of a protruding point.[51] This behavior can be replicated on the same NP by adding gaps, which adds additional points of localized enhancement that are favored by different polarizations.[52] These new features can be tuned individually, by modifying the spacing between an individual gap, or as an ensemble, by rotating the relative angular separation between the gaps.

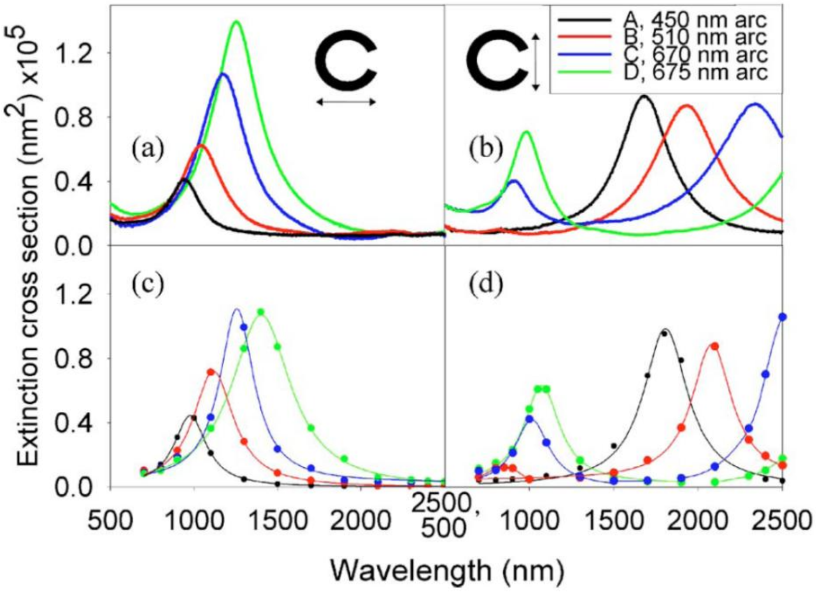

Figure 1.17: Extinction spectra of a split ring with varied length and constant radius of curvature, to tune only gap spacing. a,b) Experimental and c,d) simulated spectra were excited by white-light polarized a,c) perpendicular and b,d) parallel to the gap. Figure used from [48].

The increased spectral and spatial control of the split ring has demonstrated the applicability of plasmonic complexity in a wide range of fields, including metamaterials [53-57] and highly reproducible surface enhanced Raman substrates [58, 59] Further decreasing the symmetry extends this complexity and increases the potential for specialized applications. These specialized systems are capable of performing more numerous and complex functions within a single compact NP. An example of the potential of specialized complexity is found in the nanoswastika. The chirality of the geometry, matched with the large lateral surface area offering increased optical interaction, can be tailored to convert incoming light into torque. Correctly optimized, a single nano-motor can move a dielectric weight more than 4000 times its own volume under illumination by linearly polarized light.[60]

Another example is the nanoscale, which is a structure composed of a nanowire with many S-shaped curves.[61] Unlike the other structures, the nanowire is not subwavelength on all dimensions, but the “S” features interact locally and generate PPR behaviors. The chirality of this structure, coupled with its large surface area, interacts differently with incoming circularly polarized light, depending on handedness. In the far field, transmitted light with a similar chirality to the structure is transmitted preferentially compared to its counterpart. In the near field, the NFS displays an unexpected behavior as the points of enhancement are located at convex surfaces or along straight sections, which can be switched by altering the direction of circular polarization. (figure 1.18)

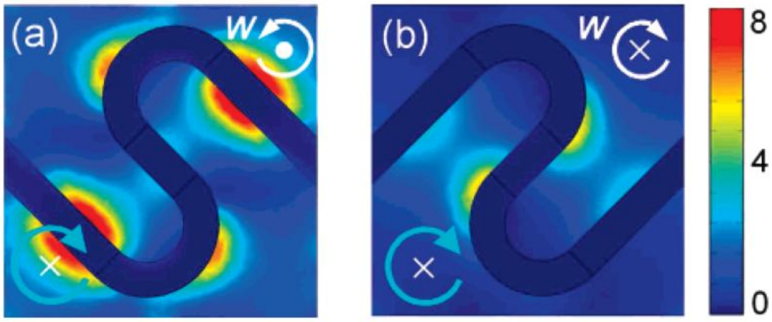

Figure 1.18: Calculated image of the electric field intensity in the plane of a single S-shaped nanowire for a) clockwise and b) counter-clockwise excitation at its 630nm resonance. Figure used from [61].

These geometries are examples of how reciprocating features increase the unique spectral and spatial features available in a single, compact NP. The antithesis of reciprocating geometries is the spiral, which is the primary motivation for this dissertation. A spiral arm spacing, between successive turns, and arm width that are much narrower than the incident light presents a laterally extended surface of continuous plasmonic coupling. This continuous intra-particle coupling through curved features generates strong NF enhancements and localized plasmon hybridization while the total lack of geometric symmetry ensures that no resonance remains dark. Furthermore, the extended size and order of the spiral allows for non-localized phenomena, similar to deterministically aperiodic ensemble systems, without the spatial separation between the simple, constituent nanoparticles that simplifies the spectral and spatial optical response. Finally, the chirality of the structure exhibits phenomenology similar to that of structures such as the S-shaped wires and nanoswastikas.

Previous research with large, micron-sized spiral structures has shown their potential as high-efficiency optical focusing elements [62, 63] and miniaturized polarization analyzers[64]. However, the lateral extent of these spirals was much larger than the resonant wavelength. This dissertation considers spirals whose lateral dimensions are smaller than the wavelength of any of their resonances. Furthermore, focus of this work is on spirals whose winding numbers are large enough to have a clearly defined inner section, which is completely surrounded by additional winding(s), without being so large as too convolute all plasmonic activity into a single, broad resonance.[65] The resulting NPs are found to have an expansive and complex plasmonic response that includes unique NFSs, multiple resonances, and significant tunability by polarization, as well as by the geometric parameters.

This dissertation systematically characterizes and organizes these features into an understandable and controllable nano-optical system. Chapter 2 discusses the fabrication and characterization techniques used to make and analyze arrays of nanospirals. Chapter 3 analyzes the spectral features and NF organization of the nanospiral arrays. This includes establishing the characteristic configurations of the NF enhancement as well as the correlation between the geometric parameters and the plasmonic response. Chapter 4 reviews the method that was developed to quantitatively analyze and characterize the variety of plasmonic features generated by the nanospiral array. In chapter 5, the effects of varied incident polarization states are discussed. Finally, chapter 6 presents the conclusions concerning the organization and potential of the nanospiral arrays, as well as initial investigations into applications of the nanospiral.

CHAPTER II

EXPERIMENTAL TECHNIQUES

Analysis of a complex geometry, such as the spiral, requires complex methods for characterizing the physical and plasmonic structure. This section reviews the computational and experimental techniques used in this work. The experimental measurements featured in this work focus on the production and imaging of the nanospiral arrays, as well as characterizing the far-field response via extinction measurements. The computational work presents the steady state near-field (NF) enhancements of the plasmonic resonances that are not experimentally observable by direct methods. All spirals considered in this work were based on arrays of the Archimedean spiral, which is defined, in polar coordinates, by:

$$r = a + b\theta \tag{2.1}$$

where b defines the spacing between successive turns and a rotates the entire spiral. For clarity, sections of the spiral that are located along the same radial vector will be referred to as *neighboring sections*. The key advantage to this type of spiral is the constant separation between successive turns that simplifies fabrication and constrains the scope of the variable parameters to arm width, arm spacing and winding number.

2.1 Fabrication methods

Production of specialized two-dimensional shapes with nanoscale features requires top-down lithographic techniques. The optimal method currently available is electron beam lithography (EBL), which boasts the highest resolution and smallest feature sizes; however, there are certain complications that arise in the fabrication of curved nanostructures. The electron-beam dosing can vary drastically with radius of curvature, which decreases as the spiral arm winds inwards. As a result, there are minor differences in arm width throughout the nanospiral. The extent of this arm-width variation is no greater than ±6nm, though the general trend is a slow narrowing of the arm as the angle varies from 3.75π to 1π. The inner 1π region, where the curvature is high, may also have a slightly thicker width and may sharpen at the inner end. An example of this is pictured

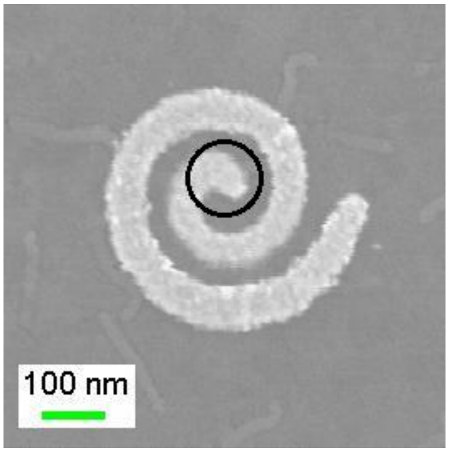

Figure 2.1: A scanning electron micrograph of a 4π spiral with an arm width of ~73nm and arm spacing of ~40nm. The central region is marked where the intended geometry is often distorted by electron beam lithographic techniques.

in figure 2.1 with the relevant area circled on the structure. Though this variation is observable with SEM imaging, the resulting geometry is still spiral and, for the purposes of these studies, these aberrations do not result in a decrease in resonances or extinction intensity compared to drawn spirals with smooth, uniform arms.

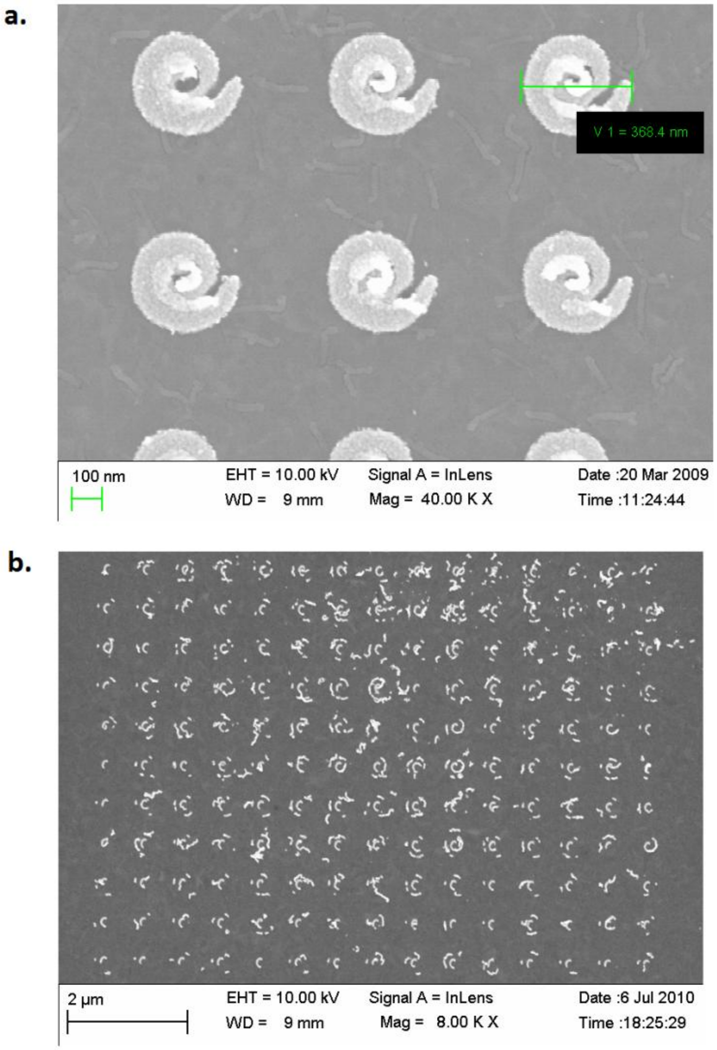

Figure 2.2: SEM images of a) an array of overdosed and b) underdosed nanospirals.

A second major issue arises from the compactness of the nanoscale spiral that places limitations on total dose. Figure 2.2 illustrates the effect of overdosing and one effect of underdosing, respectively. Overdosing results in a filled structure that has a plasmonic response of a slightly perturbed disk, which thus voids all interesting intra-particle phenomena as well as the large population of resonant modes. Underdosing exposes the fragile nature of a geometry with such a large aspect ratio; in figure 2.2b the 4π spiral has an arm length of approximately 1.6 μm and an arm width of approximately 30-40 nm. This asperity, when exposed to the wet chemistry phase of the lift-off process, results in a disintegration of the spiral into bent ellipses with lengths smaller than 1/8th π.

In order to minimize these complications, all nanospiral arrays in this work were produced with dosing parameters set between 100 and 150 μC/cm^2, with an acceleration voltage of 10KeV and a step size of 4nm. The lithographic mask, composed of poly(methyl methacrylate) (PMMA), was deposited via spin-coating in layers whose thickness vary between 110nm and 160nm depending on the particle sample. All arrays were produced on Si or ITO-covered (~27nm thick) glass substrates with no special treatment beyond a four-step, organic clean process. Following the lithographic patterning on a specialized e-beam lithography system (Raith e_Line system), the samples were developed in a 3:1 MIBK:isopropal alcohol solution, then deposited with 20nm of Au via either thermal evaporation or electron-beam evaporation. There was no observed difference between the two methods for the purposes of this study. Finally, the lithographic mask was removed in a wet-phase etchant (Remover PG by MicroChem Inc.) at ~60^o C. Multiple samples were produced with this procedure to fabricate arrays of nanospiral with geometric parameters ranging between 30-70nm, for arm width, 30-50nm for arm spacing and 2-6π for winding number. Excepting arrays that were specifically produced to probe the response due to varied array pitch, all arrays were produced in

10um x 10um pairs, one with a pitch of 650nm and one with a pitch of 1µm. Following fabrication all samples were characterized via scanning electron microscopy (SEM) in the same Raith EBL system to ascertain the geometric parameters of the successfully produced arrays. These images were also used as the input geometries for some of the computational studies.

2.2 Characterization techniques

Experimental analysis of nanospiral plasmonic behavior focuses on white-light extinction spectroscopy. The extinction spectrum of an array represents the decrease in the transmitted intensity at resonant wavelengths due to absorptive and scattering processes that comprise the far-field response of PPRs. The standard experimental method for acquiring an extinction spectrum requires two white-light transmission spectra, one through the spiral array and the substrate, I_{total}, and the other though the substrate alone, I_s, which are given by

$$I_s = \eta_I I_0 e^{-\alpha_s(\lambda) z_s} \tag{2.2}$$

$$I_{total} = \eta_I I_s e^{-\alpha_{total}(\lambda) z_{spiral}} \tag{2.3}$$

where η_I is the transmission efficiency of the instrumentation, I_0 is the spectrum of the source, and $\alpha_{total}(\alpha_s)$ and $z_{total}(z_s)$ are the attenuation and thickness, respectively, of the NP/substrate (substrate). The exponential term is related to the extinction coefficient of the array, $Q_e = \rho C_e z_{spiral}$, by

$$Q_e = \rho C_e z = \rho(\alpha_{spiral} z_{spiral} - \alpha_s z_s) \tag{2.4}$$

where C_e is the extinction coefficient per particle and ρ is the particle density. Thus by normalizing I_{total} by I_s we calculate the transmission spectrum for the array given by

$$T_{spiral} = \frac{I_{total}}{I_s} = e^{-Q_e} \tag{2.5}$$

which can be solved for the extinction coefficient for the array:

$$Q_e = -\ln(T_{spiral}) \tag{2.6}$$

For the nanospiral arrays, white-light transmission spectra were acquired with a 50μm core, multi-mode fiber coupled to a tungsten lamp, for illumination, connected to a WITec confocal microscope (WITec alpha NSOM) using Nikon 60x illumination and collection objectives leading to a Princeton Instruments spectrometer (Acton SpectraPro 300i) with a thermoelectrically cooled, pixelated charge-coupled detector (Roper Scientific, model 7344-0001, 1340x100 pixels) by a 100μm core, multi-mode fiber. A schematic of the optical system is displayed in figure 2.3

With this configuration, the area of illumination was smaller than the arrays and the collection area was less than 1μm. All measurements were set to span the spectral range of 500nm to 1400nm. Spectra were taken at slightly different locations within the array (± approx. 400nm along both x and y array axes). These data sets showed no significant change in the location of resonant peaks and only minor changes in intensity, which affect all peaks equally and confirm the assumption that all extinction spectra represented contributions of a small ensemble of geometrically similar spirals.

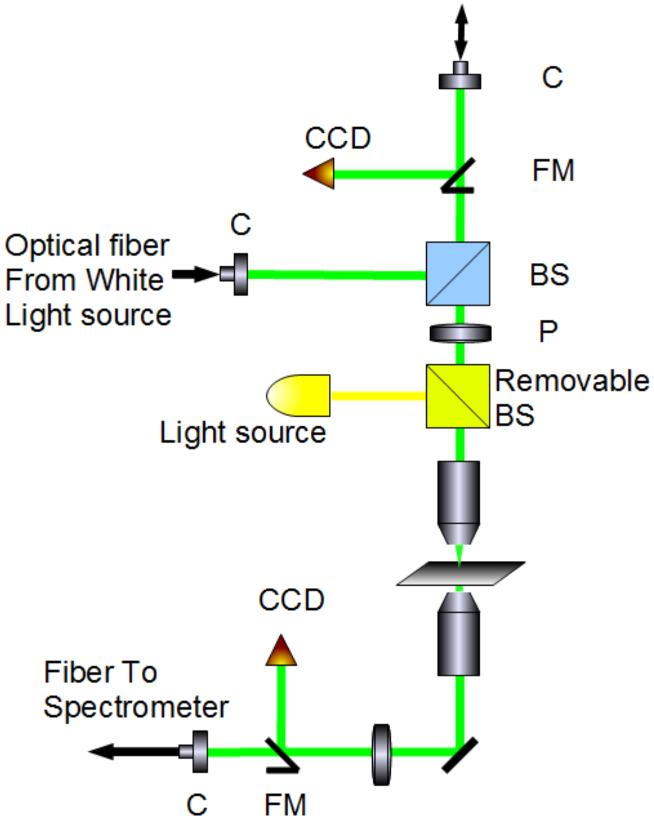

Figure 2.3: Schematic representation of the confocal microscope used for all experimental spectra. Collimators, C, beam splitters, BS, polarizers, P, and flip mirrors, FM, are all placed in the same sequence as they are in the microscope casing.

The microscope is configured to modulate the polarization of the incident white-light, or monochromatic, source between any angle of linear polarization and both circular polarizations, as well as of unpolarized light. The linear polarizer covers the entire spectral range of the experiments. However, the circular polarization, achieved with a linear polarizer followed by a quarter-wave plate, is composed of two spectral ranges. One quarter-wave plate, which generates a consistent phase shift from 500nm-700nm, was used to generate a set of shorter wavelength transmission spectra and a second, which generates a consistent phase shift from 690nm-1400nm, was used to generate the corresponding longer wavelength, transmission spectra.

All experimental spectra were processed with programs written with Matlab® ® software, which were developed to convert transmission spectra into extinction spectra, with smoothing functions to reduce detector noise. For the circularly polarized spectra, this process included a step in which the spectra from the short and long wavelength quarter-wave plates were stitched together at 750nm, with an offset applied to the longer wavelength spectra to avoid discontinuities.

2.3 Simulation techniques

The limitation for resolving optically-induced electric field phenomena is significant enough that few methods are available to view the spatial configuration of the near-field enhancements generated by plasmonic resonances. These few methods, primarily near-field scanning microscopies, are further complicated by imaging based on interfering with or coupling to the excited plasmon that would result in a non-trivial perturbation in a system, which is already quite complex. A possible exception is scanning cathodoluminescence microscopy, but this method may produce a distorted image due to the extremely localized excitation spot size, which is usually 5-10nm, and was not available for the studies in this thesis. As a result, computational methods that produced spatially resolved mapping of the electric field on nanoparticle surfaces are utilized to visualize the plasmonic activity and characterize resonant modes.

Due to the complexity and broad spectral response expected for the nanospiral geometry, the simulation algorithm must define the electromagnetic behavior in a three-dimensional volume and treat a broad spectral range. The methods for stimulating this behavior divide into two categories, differential and integral, which are defined by the form in which Maxell's equations are solved. Integral methods, such as methods of moments or transmission-line matrix methods, can simulate a broadband excitation but are limited to discretizing only the conducting surface. All differential methods discretize the simulation region, and certain types simulate broadband excitation. Finite-element methods (FEMs) are examples of the integral method and are typically calculated in the frequency domain. Methods such as finite-difference time-domain (FDTD) incorporate the ability to treat broad-band excitation by calculating in the time domain. FEMs are limited in their application, since solutions are generated for every frequency at steady state, so transient states and non-linear interactions are not treated. For FDTD, the electric and magnetic fields are functions of time that incorporate transient effects and simultaneous solution of the frequency domain at each time step. Furthermore, wide acceptance within the plasmonics community and an availability of commercial solvers makes FDTD the optimal method for analysis of the nanospiral system. This work primarily uses a commercially licensed FDTD engine produced by Lumerical Inc.

2.3.1 Finite-difference time-domain theory

FDTD simulations require two steps, first defining the discretized simulation space and second, running the FDTD algorithm over all pixels, until a preset time-step is reached. Most of the specifics of the first step were used in this work will be discussed in the next section; understanding the second step requires a discussion of how the algorithm is run and how it treats the simulation volume. This algorithm is based on Yee’s formalism [66] that starts with the component form of Maxwell’s curl equations:

$$\frac{\partial E_x}{\partial t} = \frac{1}{\mathcal{E}}\left(\frac{\partial H_z}{\partial y} - \frac{\partial H_y}{\partial z} - \sigma E_x\right) \tag{2.7}$$

$$\frac{\partial E_y}{\partial t} = \frac{1}{\mathcal{E}}\left(\frac{\partial H_x}{\partial z} - \frac{\partial H_z}{\partial x} - \sigma E_y\right) \tag{2.8}$$

$$\frac{\partial E_z}{\partial t} = \frac{1}{\mathcal{E}}\left(\frac{\partial H_y}{\partial x} - \frac{\partial H_x}{\partial y} - \sigma E_z\right) \tag{2.9}$$

$$\frac{\partial H_x}{\partial t} = -\frac{1}{\mu}\left(\frac{\partial E_z}{\partial y} - \frac{\partial E_y}{\partial z} - \rho_m H_x\right) \tag{2.10}$$

$$\frac{\partial H_y}{\partial t} = -\frac{1}{\mu}\left(\frac{\partial E_x}{\partial z} - \frac{\partial E_z}{\partial x} - \rho_m H_y\right) \tag{2.11}$$

$$\frac{\partial H_z}{\partial t} = -\frac{1}{\mu}\left(\frac{\partial E_y}{\partial x} - \frac{\partial E_x}{\partial y} - \rho_m H_z\right) \tag{2.12}$$

where E and H are the electric and magnetic field, respectively, ε is the electric permeability, μ is the magnetic permittivity, σ is the electric conductivity, and ρ_m is the magnetic resistivity. The simulation volume is divided into discrete pixels with this set of equations applied to the edges and interfaces, as displayed in figure 2.4. This spatial organization is known as the Yee cell and, when replicated in an extended lattice, ensures all electric (magnetic) field components are surrounded by four magnetic (electric) field components.

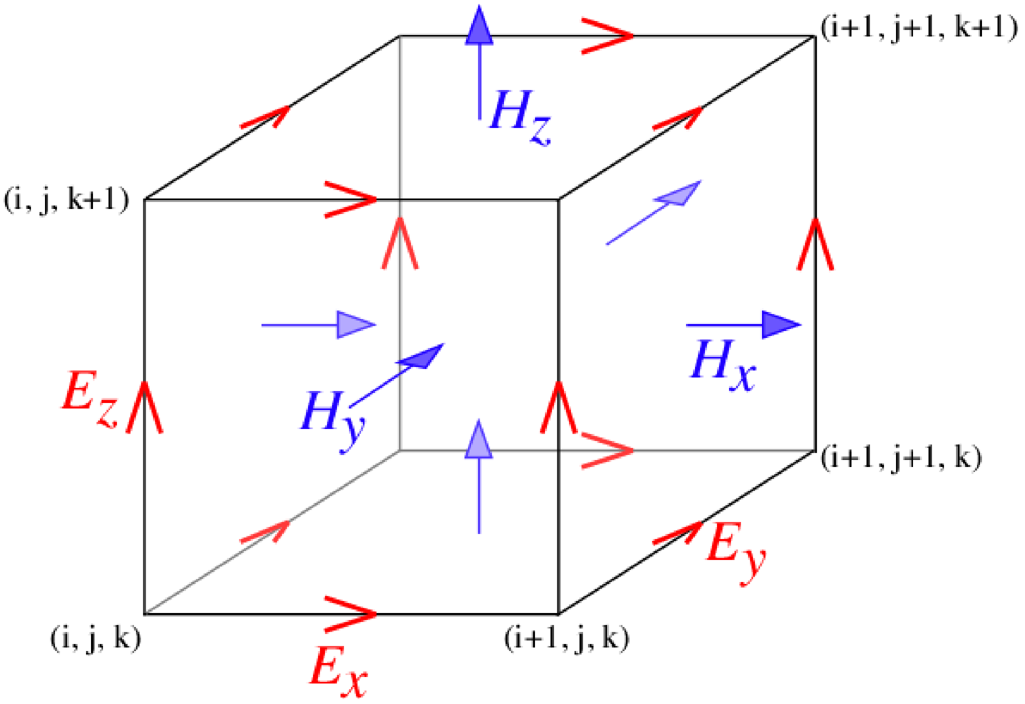

Figure 2.4: A visualization of a single Yee cell centered on a material lattice point. The electric and magnetic field vectors are positioned along the edges and faces of the simulation cell, respectively, at which the FDTD algorithm calculates electromagnetic fields that act on that lattice point. Image used is taken from http://ab-initio.mit.edu/wiki/index.php/Image:Yee-cube.png.

The discretization of these electromagnetic-field components assigns this set to every coordinate (*i*,*j*,*k*) in the simulation volume, (*i*Δ*x*, *j*Δ*y*, *k*Δ*z*), and incorporates a time dependence, (*n*Δ*t*). This results in centered finite-difference expressions, an example of which is

$$\begin{aligned} E_z^{n+1}\left(i,j,k+\frac{1}{2}\right) &= \frac{1-\frac{\sigma\left(i,j,k+\frac{1}{2}\right)\Delta t}{2\varepsilon\left(i,j,k+\frac{1}{2}\right)}}{1+\frac{\sigma\left(i,j,k+\frac{1}{2}\right)\Delta t}{2\varepsilon\left(i,j,k+\frac{1}{2}\right)}} E_z^{n}\left(i,j,k+\frac{1}{2}\right) \\ &+ \frac{\Delta t}{\varepsilon\left(i,j,k+\frac{1}{2}\right)}\left(1+\frac{\sigma\left(i,j,k+\frac{1}{2}\right)\Delta t}{2\varepsilon\left(i,j,k+\frac{1}{2}\right)}\right)^{-1} F_H \end{aligned} \tag{2.13}$$

where

$$F_H = \frac{H_y^{n+\frac{1}{2}}\left(i+\frac{1}{2},j,k+\frac{1}{2}\right) - H_y^{n+\frac{1}{2}}\left(i-\frac{1}{2},j,k+\frac{1}{2}\right)}{\Delta x} + \frac{H_x^{n+1/2}\left(i,j-\frac{1}{2},k+\frac{1}{2}\right) - H_x^{n+1/2}\left(i,j+\frac{1}{2},k+\frac{1}{2}\right)}{\Delta y}$$

These equations are iteratively stepped through time till the preset simulation time is reached. The stability and accuracy of the algorithm is based on correctly choosing the minimum time-step, the spatial step size, and correct boundary conditions at the edges of the simulation volume. The time-step is correlated to the spatial step size; for Lumerical, this is defined by the inequality[67]

$$c_{max}\Delta t \leq \left(\frac{1}{\Delta x^2}+\frac{1}{\Delta y^2}+\frac{1}{\Delta z^2}\right)^{-1/2} \tag{2.14}$$

where $c_{\max}$ is the maximum electromagnetic wave phase velocity. Besides being linked to the time-step, the spatial step size must also consider the complications due to anisotropic movement of an electromagnetic wave along the diagonals of the lattice. To limit this perturbation, either non-rectangular mesh types or very small sizes can be used. Lumerical is limited to rectangular meshing, so all simulations are set with nanometer step sizes. Step sizes of 1nm, 2nm, and 4nm were compared for the simulations in this dissertation; all these step sizes produced spectra that were virtually indistinguishable.

A large variety of boundary conditions have been developed for FDTD simulations, but for the purposes of these studies, only two were used: periodic boundary conditions, and perfectly matched layers. The former simply replicates the field components at opposing faces of the Yee cell, thus simulating the behavior of an array of homogeneous structures with uniform illumination that is desired for this dissertation. The latter boundary condition acts as a perfect absorber, bending the fields that penetrate the interface by slowly increasing the dielectric function. By bending the field vectors, we avoid scattering back into he simulation volume. These are appropriate for the top and bottom of the simulation volume, which would normally be the regions where the optical signals are injected or collected for transmission or reflection measurements.

2.3.2 Simulation setup

When applying the FDTD method to the nanospiral experiments, multiple phases were required; first, a simulation area had to be generated that matched the physical parameters of the fabricated systems; second, simulation parameters were tuned such that extinction spectra from the simulations matched whose from the corresponding experiments; and finally, any dissimilarities between the two that could not be corrected had to be accounted for.

The first phase, designing the simulation system, utilized the CAD program that accompanies the simulation software. The lateral nanospiral shapes were initially generated by importing SEM images of fabricated nanospirals, which were processed with a high-pass filter to separate the structure from the substrate. These shapes were then projected into the third dimension to the same thickness as the fabricated nanospirals, 20nm. The optical properties of the nanospiral were set by defining the dielectric function of the structure to be that of Au, based on the measured dielectric functions by Johnson and Christie.[68] The substrate was defined by two stacked planes of 27nm thick InSnO (ITO) and SiO_2, whose thickness extended beyond the simulation region. The lateral extent of the simulation was set to 650nm with periodic boundary conditions on all interfaces, excepting the two, normal to the substrate surface that were defined as perfectly matched layers. The internal meshing constant was set at 4nm for the region directly surrounding the particle, and an adaptive meshing for the remaining volume. The optical input was generated from a plane set 100nm above the substrate surface in the form of a 2fs, broad-band pulse. This ultrafast light-pulse duration defined the bandwidth of the source to be 400nm to 1400nm.

The simulation output was generated from two laterally oriented monitors, one (monitor 1) placed 100nm below the nanoparticle, within the SiO_2, and one (monitor 2) placed on the plane positioned one pixel above the nanoparticle surface. Both monitors recorded the steady-state values of the transmission and electromagnetic-field data over a spectral region of 500 to 1400nm for a period of approximately 200fs, or until the field intensities decayed below 10^{-5} of the incident field. Monitor 1 was positioned well beyond the volume that would see a local-field enhancement around the nanoparticle such that drops in the normalized transmission at that plane would represent extinction, mimicking the experimental extinction spectra. Monitor 2 was positioned to view the near-field structure induced by plasmonic activity on the surface normal to the incident pulse.

The second phase of the simulation was devoted to setting parameters that were not well defined, specifically the ITO layer. While the ITO thickness was well established, the dielectric function of ITO is known to vary between different depositions even in the same deposition system. All samples produced in this work use substrates from a single deposition from Delta Technologies (product number CB-90IN, ~27nm ITO on Corning 1737 glass substrates), so they were assumed to have similar dielectric properties. Using a white-light ellipsometer, whose range of spectral sensitivity spans 400nm to 900nm, we established the dielectric function for the ITO that was supplemented with estimated values based on rough trends illustrated in the literature. Iterations of the simulation were then run while modifying the estimated values to match with the experimental spectra.

This tuning was continued until all of the spectral peaks observed in the area of interest from the experimental spectra were detectable. Two primary dissimilarities persisted: a difference in extinction coefficients, especially at longer wavelengths and a red-shift for resonances at spectral positions beyond 900nm (figure 2.5). The former issue is the result of reduced, non-uniform transmission efficiency that is not replicated in the ideal illumination-detection system of the simulation. This is especially notable at wavelengths longer than 800nm, where the quantum efficiency of CCD camera in the spectrometer begins to drop significantly. The latter issue relates to a mismatch between the applied ITO dielectric function and the actual dielectric function. Due to close agreement between the spectra, compounded with the issue of intensity matching, we settled on this dielectric function in order to advance the primary studies of this dissertation.

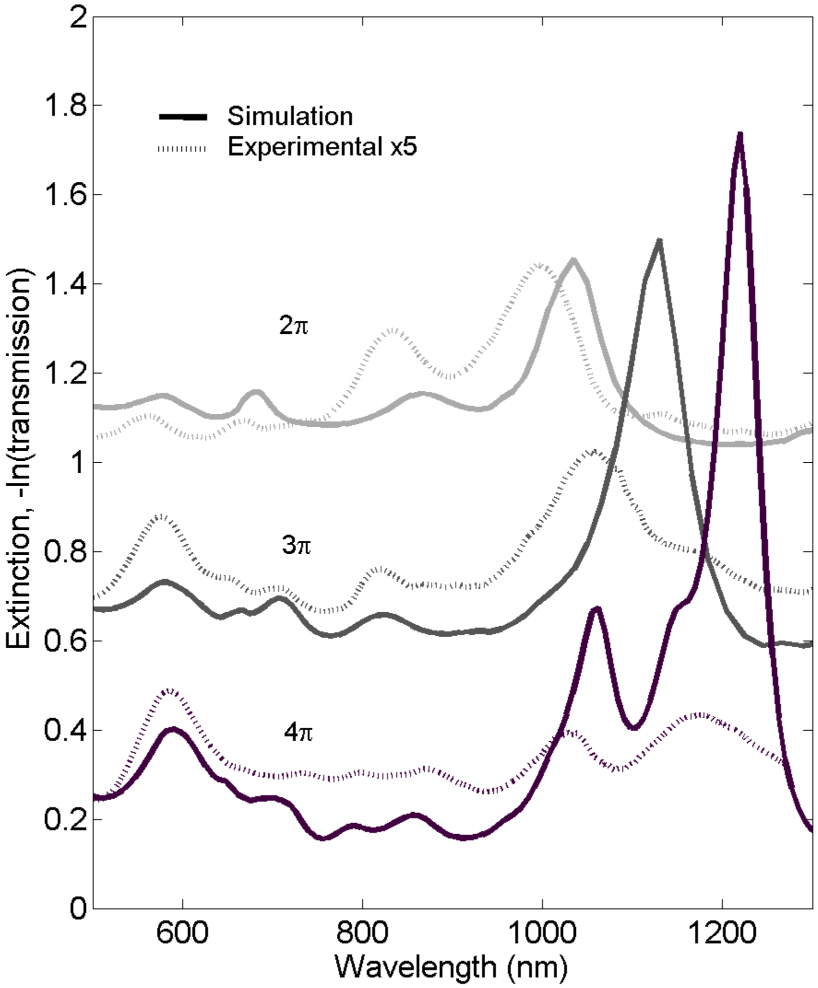

Figure 2.5: Extinction plots of fabricated spirals with winding numbers 2π, 3π, and 4π. Each spiral is represented by an experimentally acquired extinction spectrum, scaled by a factor of five for clarity, and a simulated extinction spectrum, generated from an SEM image of each spiral.

2.3.3 Analysis methodology

The raw data provided by the simulation represent the spectral and near-field response of the system. The spectral data were primarily used to verify a match to the experimental work, though the easy manipulation of geometric parameters in the simulations was a specific advantage and time-saver when exploring the effect of single parameter variations in the fabricated Archimedean spirals. Analysis of this data set was accomplished with simple peak fitting and comparison using functions available in Matlab® . Similarly, analysis of position and intensity of the maximum field enhancement and visualizing of the near-field energy organization is possible with simple functions.

For further quantitative comparison of the NF structure, specialized programs were developed to produce a set of basis vectors for the spiral. The primary basis vector travels along the spiral arm such that enhancements can be correlated with the corresponding winding number. Chapter 3 focuses on the development, functionality and potential of this program.

CHAPTER III

CHARACTERIZING THE LINEAR RESPONSE OF THE NANOSPIRAL

Arrays of nanospirals produce more plasmonic resonances, generated by a wider range of mechanisms, than any other lone geometry previously researched. Even ensembles of plasmonic particles or the addition of different materials, such as molecules or quantum dots, fail to compare to the plethora of plasmonic activity produced by nanospiral arrays. To understand and apply the potential of the nanospiral and similarly complex plasmonic systems, a basic organization of the plasmonic behavior must be established. For the nanospiral, this includes establishment of how parametric variation tunes the spectral and near-field (NF) response, characterization of a basis set of NF configurations that encompass the observed NF variation, and definition of the nomenclature that is required for further discussion. This will be obtained from phenomenological analysis of simulated and fabricated nanospiral arrays.

This chapter will achieve these goals by limiting the scope of investigation to a single, linear polarization, aligned with the y-axis as defined in figure 3.1, and exploring the variation of spiral arm width, spacing, and winding number. This polarization produces similar behavior to other linear polarizations but includes a smaller number of excited resonances, which will simplify this initial characterization. A study of simulated and fabricated nanospiral arrays will be reviewed for spirals whose geometric parameters will not extend beyond the following: 2π to 4π winding number, 20-80nm arm spacing and 20-80nm arm width. Outside of these limits the number of resonances and the set of different, characteristic NF configurations decrease to single, heavily red-shifted resonance. Also included will be brief discussions concerning the variation of array pitch and spiral thickness but, due to the lack of connection to the spiral geometry and the simplicity of their affects, these parameters will not be varied in any other section unless mandated by additional structures.

3.1 Characteristic near-field configurations

Nanospiral arrays whose lateral extend is below 500nm present a prolific plasmonic system with numerous resonant modes that correspond to unique near-field configurations. Compared to simpler geometries, these configurations are not limited to multi-pol organization but they do represent a logical, geometrically driven organization that relate to specific mechanisms and characteristic ordering of significantly enhanced regions of the electric near-field intensity. These configurations are characteristic of the spiral geometry and can be classified by the organization of the maximum local field enhancement into three main categories. Using an SEM image of a fabricated 4π spiral pictured in figure 3.1a) as a model, figure 3.1b-d displays examples of three structures that are characteristic of the spiral response at any winding number: a radially oriented "*hourglass*" mode (figure 3.1b); a *standing-wave* mode (figure 3.1c) analogous to longitudinal modes of a nanorod [69, 70]; and a *focusing* mode (figure 3.1d) that centers the majority of the confined energy at either or both ends of the spiral.

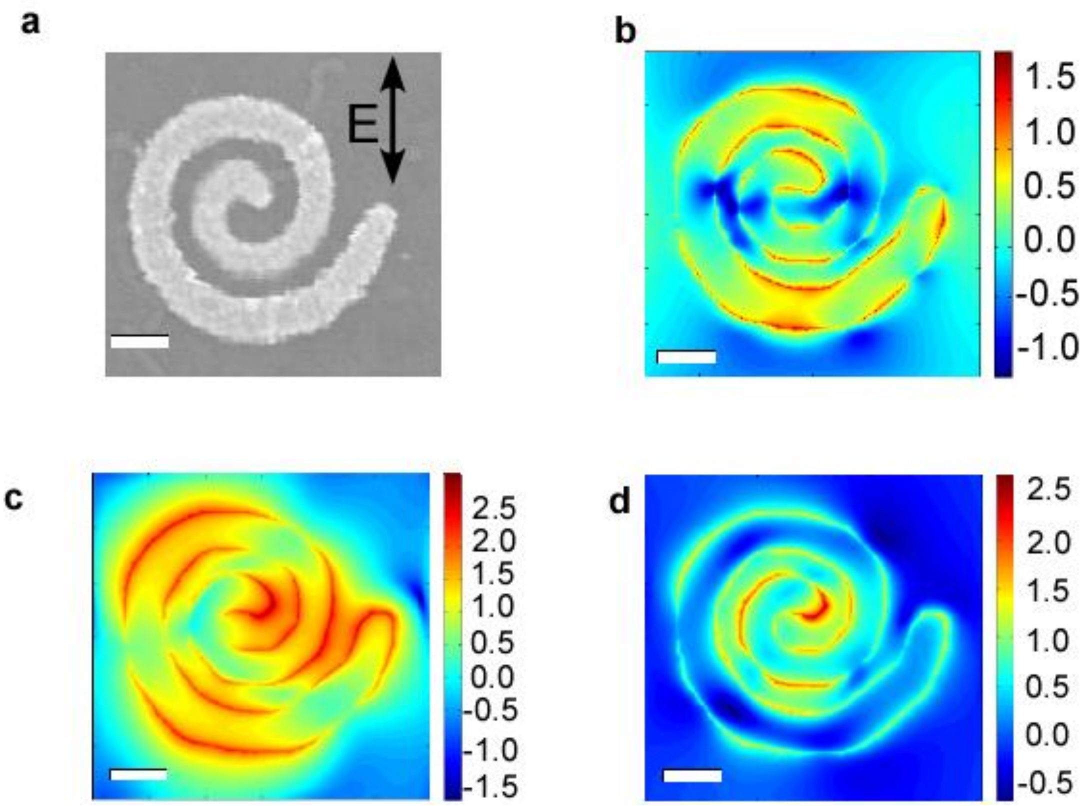

Figure 3.1. a, Micrograph of the experimentally produced 4π spiral used as the model in simulation and examples of the near-field distribution of each mode configuration for the 4π spiral: b**,** hourglass (601 nm), **c**, focusing (867 nm), and d, standing-wave (1,233 nm). Scale bar is 100 nm wide and the color bar is scaled to $\log_{10}$(normalized transmission).

Each configuration dominates a specific region of the extinction spectrum, with the hourglass at the lowest wavelength, followed by the focusing configuration and then standing-wave configuration. At the border of the focusing and standing-wave regions, there exists transitional region where existing resonances display an organization generated by a linear combination of the surrounding two configurations. This region may vary depending on specific geometric parameters, but for most spiral in this study this region usually is located between 900nm and 1000nm. As an example, figure 3.2 displays an extinction spectrum for the nanospiral array from figure 3.1a), with regions separated for each characteristic configuration, as well as marks for the specific examples used in figure 3.1.

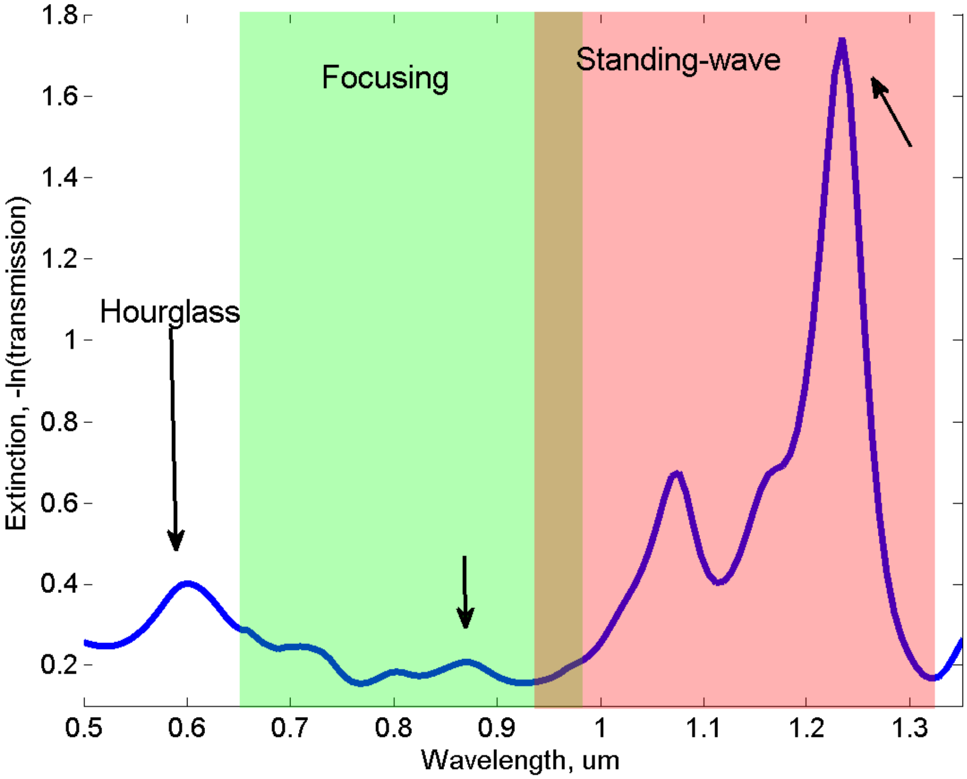

Figure 3.2: An extinction spectrum of a simulated 4π spectrum with the regions where resonances are predominantly hourglass, focusing and standing-wave configurations. Markers annotate the position of each resonance pictured in figure 3.1.

The “hourglass” configuration is represented by only a single resonance at the shortest wavelength, around 580 nm. The spectral position of this configuration is exceptionally insensitive to variation of any geometric parameter, compared to the other configurations and is the only one whose NF organization aligns to the incident polarization. The nodes of NF enhancement are localized by direct coupling between neighboring azimuthal sections of the spiral arm oriented parallel to the incident polarization, similar to the characteristic transverse mode generated by lines of nanodisks.[71] Indeed, simulations of the plasmonic responses of ellipses with their long axes perpendicular to the electric-field polarization, show significant agreement with the hourglass configuration, with both spectral and spatial features overlapping (Figure 3.3).

The parameter that defines the spectral position of the chain is the average diameter of the ellipses parallel to the line of structures. The resonant frequency is stabilized against aberrations within the ensemble by near-field coupling, acting as strongly coupled dipole oscillators whose resonances are locked by longer range coupling across the entire ensemble.[72] This behavior, when found in the nanospiral, distinguishes the hourglass configuration from the others by its spectral and near-field stability and the fact that the mechanism for its generation as arises from an ensemble of sub-regions within the spiral that act independently to couple to each other. This is opposed to the behavior of the other two configurations, which are defined by the entire geometry.

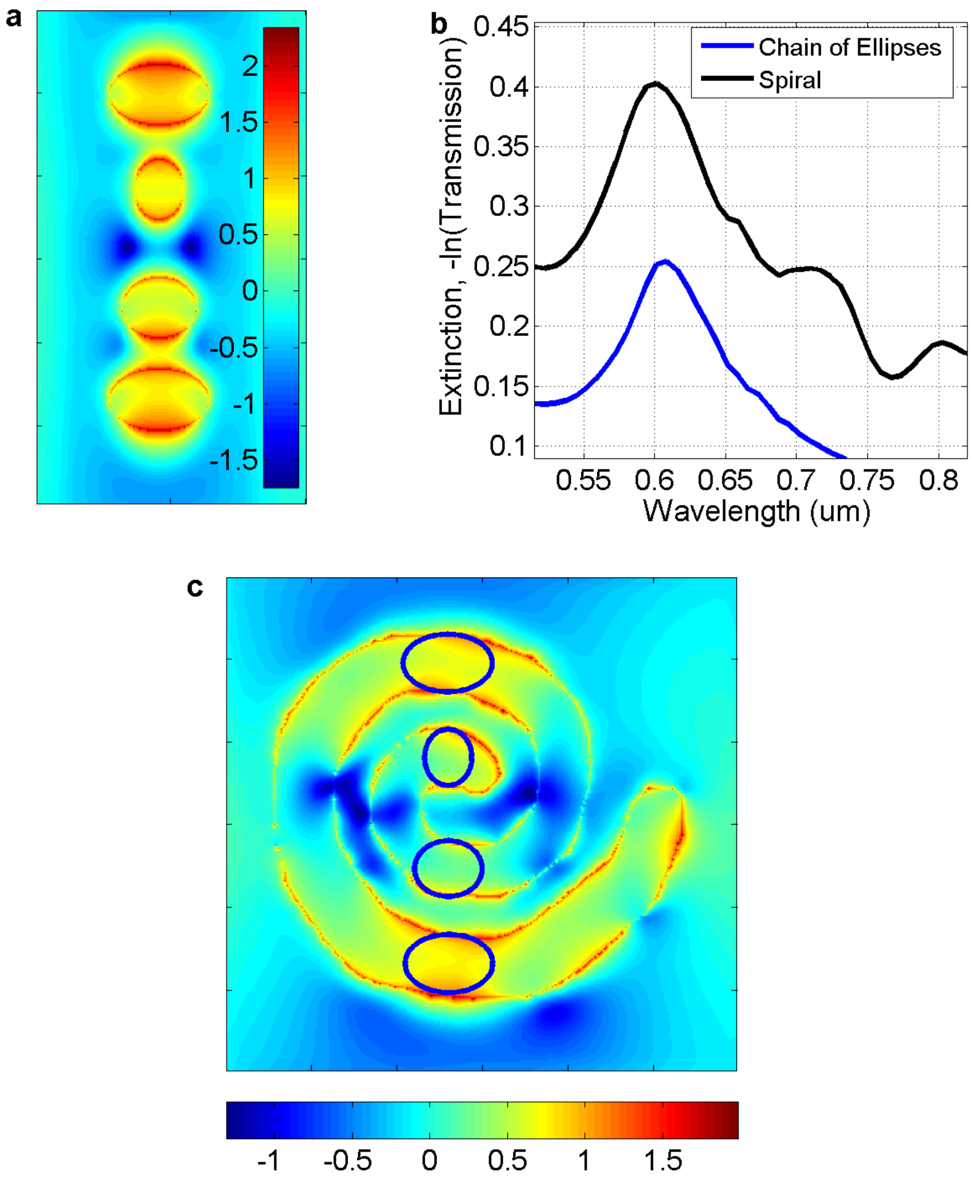

Figure 3.3: a) The NF enhancement image for a chain of nanoellipses at the 601nm resonance. b) Extinction spectra for the simulated chain of nanoellipses and 4π nanospiral, with the same arm spacing and arm width as the spacing and short axis length of the chain of nanoellipses. c) The NF enhancement image of a nanospiral illuminated with y-axis polarized white light at 601nm. Blue outlines annotate the relative position of those represented in a).

The standing-wave configuration exhibits a plasmonic response resembling the harmonic modes of nanorods with high aspect ratios. Similar to the nanorod, the nanospiral has numerous multipole resonances that decrease in wavelength as they increase in harmonic order and that red-shift as the winding number (length) increases. Unlike nanorods, the asymmetry of the system introduces even and odd harmonics and reduces the spectral region where these resonances are bright. As a result, the standing-wave elements can include an odd number of nodes and the spectral position tunes from a relatively low extinction/dark state near 900nm to a maximum extinction around 1150nm before returning to a dark state around 1200nm. Furthermore, the strain induced by bending the analogous nanorod resonance results in blue-shifts for the even harmonics, compared to the nanorod, and red-shifts the odd harmonics, compared to where they would be expected in the nanorod. Such an effect is expected as the complexity of the reconfiguration would prefer the asymmetric odd harmonics, though the radiative dampening would increase due to the curvature, and increase the energy of the non-prefered, even harmonics. Figure 3.4, pictures the spectral reorganization of the standing-wave resonances for the 3π, 3.5π and 4π nanospirals and their analogous nanorods. Considering the near-field structure (NFS), both the even and odd harmonics of the spiral resonances have significantly higher field intensities than the analogous nanorod resonances, which is attributed to the forced bending and circulation of the electronic osciallations as they follow the spiral arm. As an example, the nanorod resonance displayed in figure 3.4 presented maximum localized enhancement factor of 76 compared to 1317 for the analogous spiral mode of a 4π spiral.

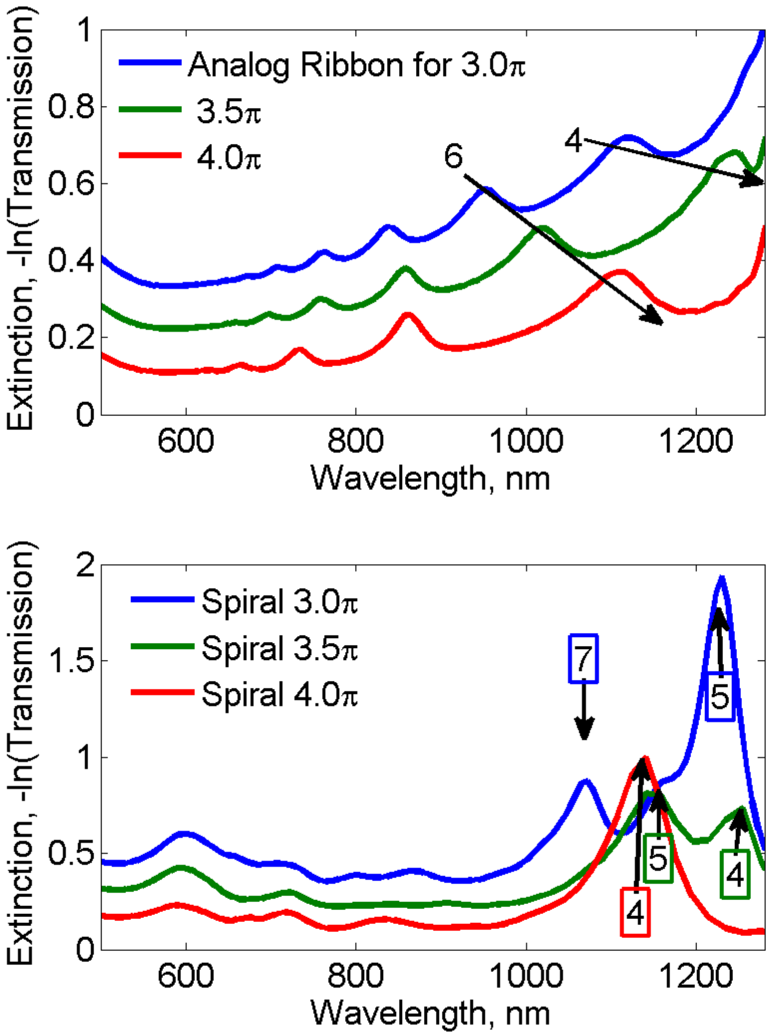

Figure 3.4: a) Extinction spectra for simulated nanorods whose lengths are equivalent to the 3π (1615nm), 3.5π (1308.5nm), and 4π (936.9nm) nanospiral with arm spacing of ~40nm and arm width of ~73nm. The spectral position of the resonances with 6 and 4 NF enhancement nodes, as the shift with growing length, are annotated. b) Extinction spectra for simulated arrays of 3π, 3.5π, and 4π nanospirals with arm spacing of ~40nm and arm width of ~73nm. Each the standing-wave resonances are annotated with number of NF enhancement nodes.

Finally, the focusing configuration is completely defined by the spiral geometry, and has no obvious analog to simpler plasmonic structures. Some plasmonic focusing geometries use sharpened points (triangle/bowtie[73]), Fresnel lenses[74] or self-similar chains of nanospheres[75] to generate a single focusing mode. The nanospiral, on the other hand, focuses the near-field enhancements into standing-wave nodes along the spiral arm that increase in total enhancement as it approaches the center. Generally, resonances that have the focusing configuration confine a significant portion of the total NF enhancement into the 0 to 2π region of the nanospiral. Due to the reduced surface area of the inner 2π region, compared to the outer 2π to 4π region, this accumulation of NF enhancement results in a significant increase for the enhancement factors within this area as opposed to the enhancement factors with the same total energy spread equally throughout the nanospiral. Variation between specific organizations of different focusing resonances is primarily distinguished by the number of enhanced standing-wave maxima that are located in the inner region and the enhancement factors of the inner end of the spiral arm. These variations depend on the specific resonant wavelength and the geometric parameters of the spiral.

Attempts to determine the generating mechanism of the focusing configuration were made, both by overlapping samples of the two other characteristic configurations and analyzing the evolution of the near-field distribution as the linear polarization is rotated. Sampled resonances of the focusing and standing-wave configurations showed no significant rotation, while the hourglass reconfigured, which suggested that the hourglass configuration had no significant role in the focusing mechanism. Higher harmonics analogous to those of nanorods do exist within this region, but superposition with the hourglass configuration did not produce focusing behavior and the comprehensive reorganization of NF enhancement nodes makes direct comparison between the focusing and standing-wave configurations uninformative.

Given this large set of distinct mode structures, it is tempting to use the popular quantitative figures of merit to characterize the system. The quality factor, Q, and the effective mode area, A_{eff}, that together describe the efficiency of a resonator system were calculated for each mode configuration from the simulation and experimental data. The Q-factor for modes of the 4π spiral were all found to be rather low and relatively close together, between 8 and 35 making them totally useless to distinguish configurations. Using the notable variation in lateral dimensions between 2π and 4π, we analyzed the A_{eff} of resonances whose NFS and spectral position remained similar and relatable as the winding number grew (figure 3.5). We found that each group of relatable resonances had

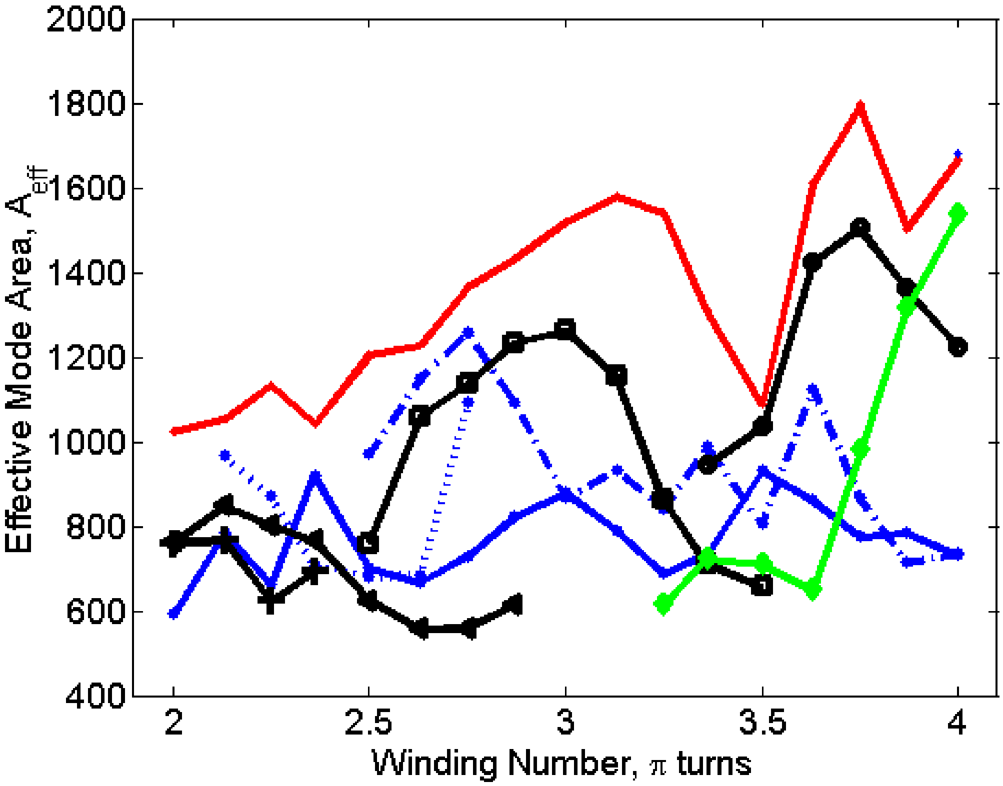

a

Figure 3.5: A line plot relating the effective mode area of a resonance to the winding number of the nanospiral array that generated it. The red line indicates the hourglass resonance, the blue lines indicate the focusing resonances and the black line indicate the standing-wave resonance. The green line represents the element that transitions from focusing to standing-wave configuration.

distinct progression but the focusing and standing-wave configurations vary within the same values without any clearly distinguished regions. To this end, analysis of the individual modes using the Q-factor or A_{eff} fails to capture the unique aspects of the different configurations.

3.2 Tuning with the spiral winding number

Geometrically, there are three parameters that define the spiral, winding number, arm width and arm spacing. Of these three, winding number is the most easily controlled by EBL processing and avoids complications from the other two parameters that arise from the modulation of near-field coupling between neighboring arm segments, which is considered the root of the complexity in this system. Interestingly, by isolating the geometric variation from NF coupling modulation exposes a plethora of geometrically motivated phenomena and a clear picture of how the spiral geometry organizes its plasmonic resonances.

At this point, a new classification must be defined to discuss the plasmonic evolution with growing winding number. As briefly alluded to in the last section, there exists a connection between certain resonances as parameters are varied where the NFS remains closely relatable and the resonance only shifts slightly. An example progression of NFSs, as winding number is increase, is displayed in figure 3.6. These quasi-invariant organizations, which will heretofore be called *elements*, can relate resonances that spectrally shift or spatially compensate significantly as parameters are varied significantly. The existence and organization of elements help illustrate the underlying plasmonic organization that is imposed by the spiral geometry.

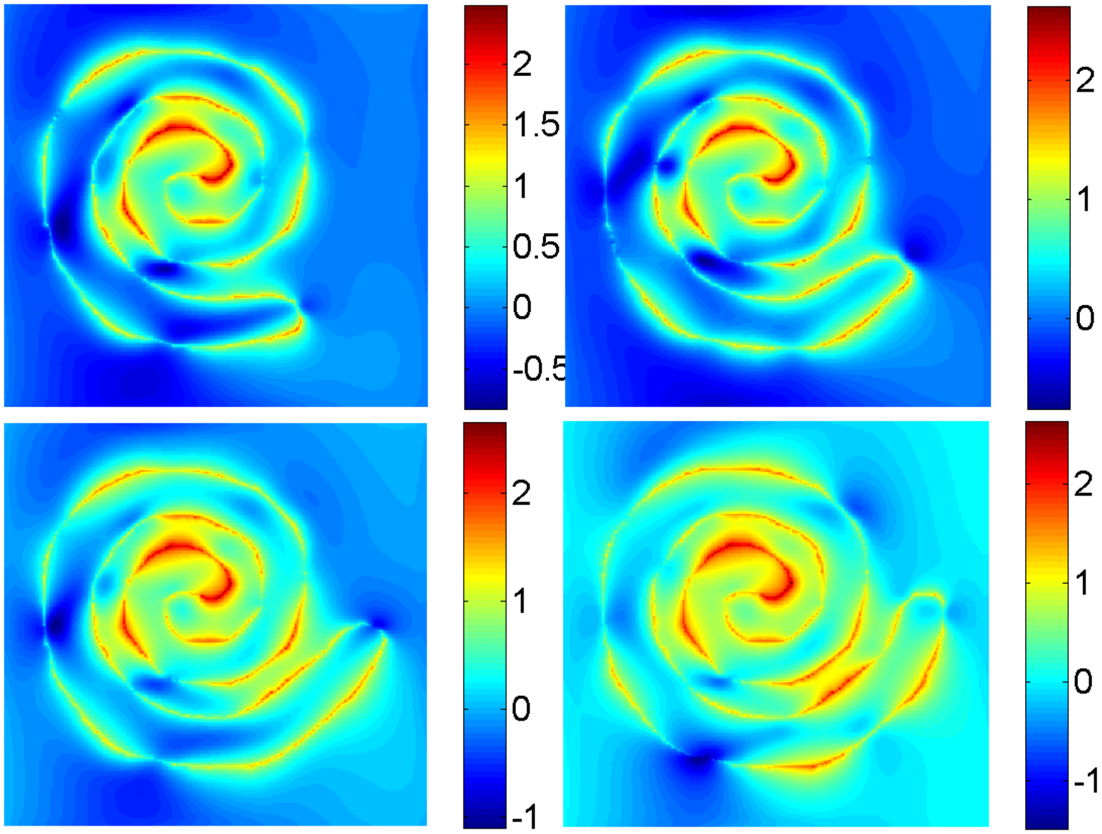

Figure 3.6: NF enhancement images of a single element that is positioned between 709nm and 718nm for simulated nanospiral arrays with winding numbers from 2π to 4π. The images represent the evolution of this element for the a)3.63π, b) 3.75π, c) 3.87π, and d) 4π nanospirals. Each spiral was excited by white light in the linear polarization aligned with the *y*-axis.

By viewing the evolution of the spiral from 2π to 4π in eighth π steps, elements become easily distinguishable and reinforce earlier assertions concerning the isolation of spectral regions to preferred characteristic configurations. For the spiral parameters chosen in these experiments, there are ten such elements, whose growth and shifting are mapped in figure 3.7. The solid line refers to the singular hourglass element, while the forking, dashed line and each of the dotted lines represent different focusing and

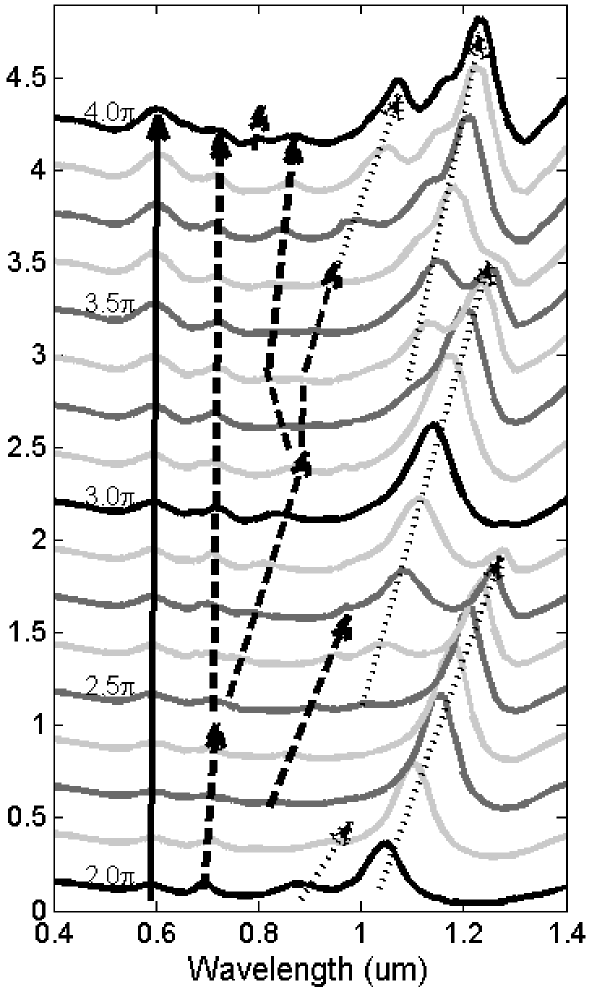

Figure 3.7: Simulated extinction spectra of spirals with winding numbers evolving from 2π to 4π in steps of π/8. The evolution of each mode is marked with arrows, solid arrow for the hourglass mode, the dashed arrow for the focusing mode, and dotted arrows for standing modes. Each spiral was excited by white light in the linear polarization aligned with the *y*-axis.

standing-wave elements, respectively. The regions defined at 4π in the preceding section persist through the entire evolution and each configuration displays its own behavior as the spiral evolves. The hourglass mode is the most stable of all the configurations with the single mode remaining spectrally stationary and the near-field pattern unmodified; as expected based on the nature of its generating mechanism. The focusing and standing-wave configurations contribute the other nine elements, four that are primarily focusing, four that are primarily standing-wave and one that transitions between the two.

The four focusing elements, which are confined to a spectral region between the hourglass resonance and approximately 900 nm, form either by spontaneous rise from the background or splitting from a relatively immobile resonance located at 700 nm. This spectrally immobile resonance can be treated as an example for all phenomena related to the evolution of a focusing element. Over the entire growth of the spiral, from 2π to 4π, the nodes of this element slowly increase in both number and size to fill the growing surface area. Some elements restrict the region of increased enhancement to a specific area, while others allow from some expansion as the spiral grows significantly larger.

Closer analysis shows that azimuthally neighboring regions can sporadically interact with the stable enhancements in the inner region by increasing enhancement through edge-to-edge NF coupling or interfering with the progressive change in placement of nodes as the spiral stretches. This illustrates how the focusing configuration controls the inner sub-section of the spiral while allowing a large amount of mobility in the outer region, illustrating the complexity of the mechanism which forms this configuration.

The four standing-wave elements exhibit much more ordered behavior with each resonance rising from the background above 1,000 nm, growing in extinction to a maximum, then decreasing until it disappears around 1,300 nm. Each of these five elements represents a resonance similar to a resonance found in a similarly sized nanorod and is distinguished from the others by a unique number of maxima and characteristic distribution of local enhancements generated by the intra-particle coupling between azimuthally neighboring regions of the nanospiral.

The strongest local field enhancements are produced by the standing-wave, however, it is also the most variegated of the configurations with the magnitude of the maximum local enhancement varying by greater than a factor of 13, as the winding number is tuned. Comparing the maximum for each element, this translates to a variation by a factor of roughly 5 between the weakest and strongest. This variation and comparison with the other configurations is presented in figure 3.8. For plasmonic applications, these elements retain the positive attributes of the numerous, spatially extended nanorod resonance, while adding higher localized field intensities, a chiral structure, and multiple, spectrally tunable elements that are not darkened due to selection rules related to higher order multipolar resonances.

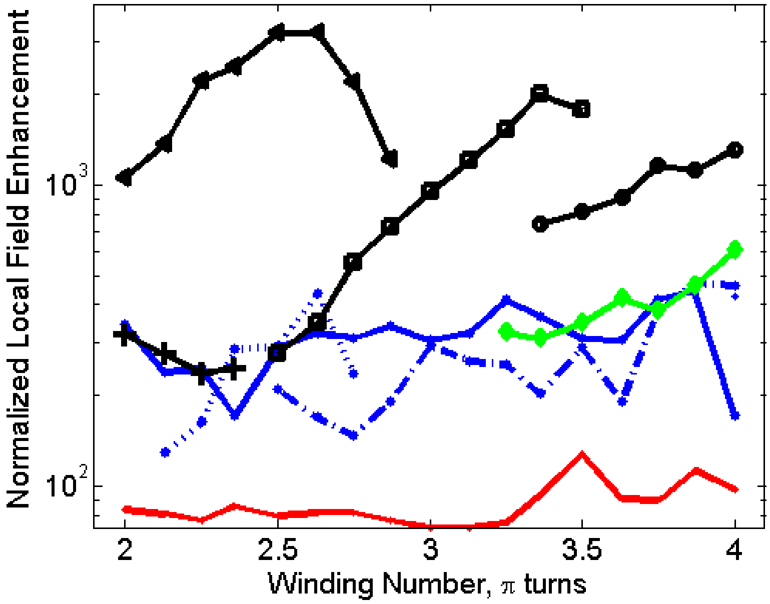

Figure 3.8: Logarithmic plot of the maximum local field enhancement within a single 2x2x2nm pixel, as a function of winding number, for each element of the nanospiral array feature in figure 3.1: the hourglass mode (solid red line), the three distinguishable focusing modes (blue lines), the four standing-wave modes (solid black lines), and the mode which transitions from focusing to standing-wave (solid green line). Each spiral was excited by white light in the linear polarization aligned with the *y*-axis.

Possibly the most interesting mode is the transition mode which traverses the 900 nm to 1,000 nm region between 3.38π and 4π. The near-field evolution of this resonance illustrates a smooth transition from a focusing mode, which is similar to the mode it splits from, to a standing-wave configuration, which is unique to all other standing-wave elements. The evolution of its maximum enhancement also follows a unique path, as displayed in figure 3.8. The importance of this element is the suggestion that spectral elements are able to traverse the focusing and standing-wave configurations, disregarding the significant difference between each mechanism and the characteristic manifestation of different organizations of the total NF enhancement. This competition between mechanisms illustrates the potential of the nanospiral geometry as a foundational model for the characterization and understanding of complex intra-particle plasmonic interactions. Understanding how these mechanisms interact will open opportunities for further development of complex systems that are tailored to specific applications.

3.3 Tuning with non-winding number parameters

The non-winding parameters a more convoluted illustration of complex plasmonic behavior and raises one of the primary concerns related to fabricating nanospirals. In order to produce nanospirals with winding numbers as large as 4π, while retaining a sub-wavelength lateral diameter, the arm width and spacing parameters become comparable to intrinsic defects, which are produced during EBL. These errors in fabrication can range from sporadic protrusions or recessions to substantial modification of the intended shape and can cause notable variation between nanospirals within the same arrays. The primary goal of this section is to illustrate that these perturbations do not irreparably distort the spiral phenomenology and discuss the limit to which these two parameters can be varied without distortion of the behavior discussed in previous sections. The issue of perturbations will be investigated by reviewing extinction spectra and computationally generated NF images of fabricated spirals, while the issue of limits will be discussed, primarily, using computer generated spirals with smooth sides to isolate it from the first issue.

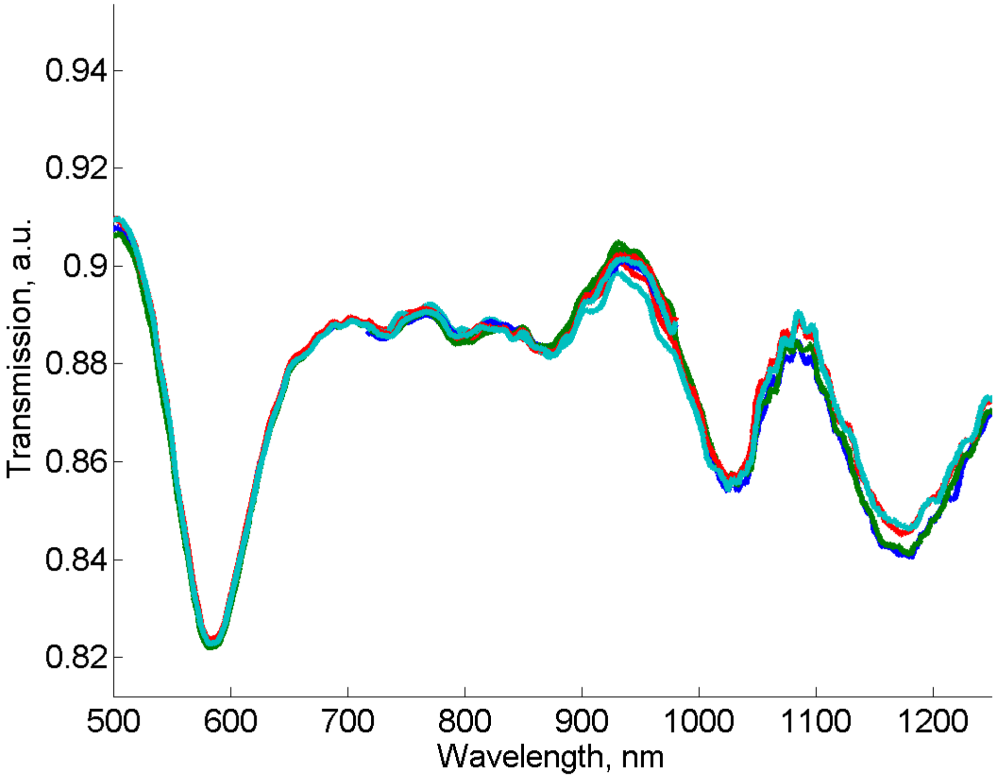

Figure 3.9: Transmission spectra of an array of ~70nm arm width, ~40nm arm spacing nanospirals taken at four locations within the array spaced 400nm apart. The array was excited by white light in the linear polarization aligned with the *y*-axis.

Localized, sporadic protrusions in more simple geometries, such as the nanostar or trimers, produce their own resonances and significantly alter the NF organization of the system. In the spiral this would be compounded with increased intra-particle coupling between azimuthally neighboring arm sections that gives preference to a localized resonant mode which is not attributed to the spiral geometry. As displayed in figure 3.1a), the sides of the spiral are definitely rough and the shape of the 0 to 1π segment is of a slightly wider shape than anywhere else on the spiral arm. As an initial verification of the necessary degree of inter-array conformity, multiple extinction spectra were acquired at interval of 400nm along the same axis of an array (figure 3.9); these showed no significant change in spectral features of nanospirals.

We then turned to intentional, small modifications to the arm width and arm spacing as well as changes to the total lateral dimension (along the longer axis), which represents a convolution of the two parameters. Nanospirals with smaller winding numbers, specifically 3π for arm width or spacing and 2π for both, are used in this discussion. This choice was made primarily because spirals with higher winding numbers have more surface area to vary, which complicates the exact value for arm width and spacing, and because of the slightly reduced number of resonances and a slightly higher extinction coefficient, which facilitate a clear presentation. However, the conclusions reached do extend to higher winding numbers

To verify experimentally that nanoscale spirals would retain their distinct plasmonic characteristics, we measured the plasmonic response of nanospirals with width and/or spacing variations smaller than ±30nm from the average design value. These limits are defined by the scale of the total structure, outside these parameters the nanospirals that can be produced with the methods and doses listed in chapter 2 become either too thin and fracture or reach the approximate limit of edge-to-edge spacing for the EBL.

We found that changes in width and spacing that result in significantly larger lateral dimensions, a gradual redshift was observed for all non-hourglass resonances, compared with laterally smaller spirals, with new focusing resonances appearing between the relatively stationary hourglass resonances and the longer-wavelength resonances. This is illustrated for the 2π spiral in figure 3.10a) where the lateral diameter at the widest point is varied between 180 and 240 nm. For smaller changes between single parameters, we were able to distinguish the boundaries between regions that are strongly *vs* weakly affected by tuning arm spacing and width, as illustrated in figure 3.10b,c for the 3π spiral. The hourglass resonance and standing-wave resonances located above 1,000 nm experience minimal spectral shifts, ±20nm and ±30nm respectively, though significant changes in the relative intensities can occur as energy is redistributed among the evolving elements. The hourglass mode is the least dependent on small changes to the non-winding parameters as it is does not disappear and experiences minor spectral shifts, <20 nm, though its relative intensity can vary significantly as shown in figure 3.10b). The standing-wave configuration is much more tunable than the others, with either parameter capable of optimizing extinction intensity.

Comparison of the 3π and 4π spirals, with consideration for the fact that the standing-wave element in the 3π is in the middle of its evolution while at 4π the longest wavelength element is end if its tuning, showed that the spectral position of the 3π standing-wave resonance is very stable to changes in non-winding parameters while the 4π standing-wave resonances are more transient and spectrally mobile. This suggests that any transient behavior of the standing-wave mode is a result of its proximity to the end of its tuning cycle. The focusing modes are strongly affected by tuning as the modes will easily disappear or sporadically form or strongly shift. These shifts are significant enough that different elements can overlap so the extent of the shifts is not clear but the spectral region of this activity is defined by the focusing configuration. From this we concluded that, although the spiral is sensitive to the arm width and spacing, the resonant behavior is robust to the expected fabrication perturbations and small changes in arm width or arm spacing.

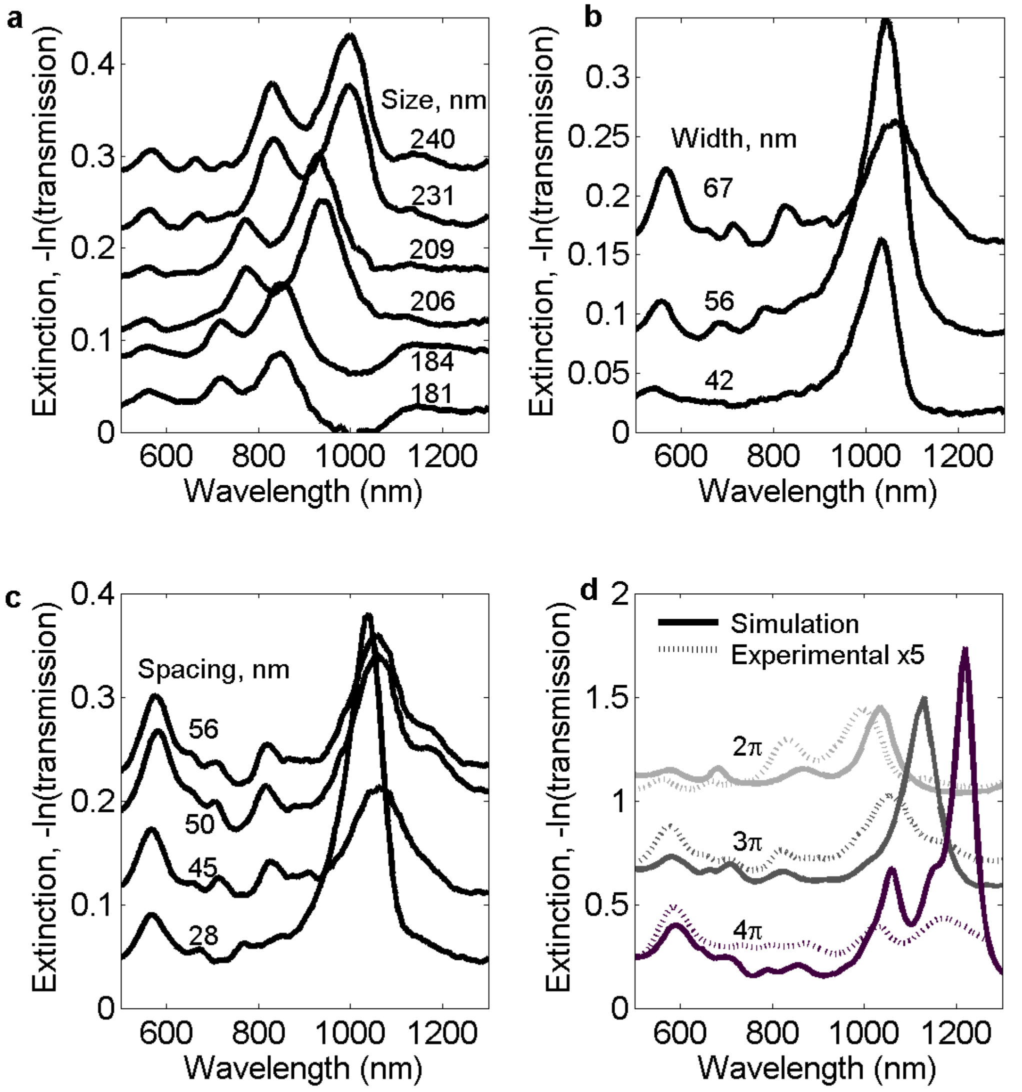

Figure 3.10: Experimentally measured extinction spectra of a**)** 2π spirals with arm spacing increasing vertically. b**)** 3π spirals with arm spacing increasing vertically. c**)** 3π spirals with arm width increasing vertically. d**)** Simulated extinction spectrum and

experimental extinction spectrum scaled by a factor of 5 for the 2π, 3π, and 4π spiral. Mismatches between the long-wavelength peaks are explained in the methods section. Each spiral was excited by white light in the linear polarization aligned with the *y*-axis.

Next we consider the issue of limits to arm width and spacing at which the observed behavior begins to deteriorate. To explore this, and avoid convolution with the previous arguments, we use computer generated spirals that have smooth edges and no perturbation at the inner sections of the spiral. The 4π nanospiral is used as the model for this study because of the large number of resonances with multiple instances of the focusing and standing-wave configurations. The parameters from the successfully fabricated nanospirals were considered the starting point and parametric sweeps were run across values that could be achieved using EBL techniques. This limits the minimum and maximum feature size to 20nm and 80nm, respectively, since this is the lower limit of EBL, without specialized developing techniques, and the upper limit before total lateral dimensions become larger than the wavelengths of multiple resonances.

Our choices of where the parameter sweeps focused were based on the assumption that excessively tight or loose spacing would result in the mechanisms related to intra-particle coupling overriding the geometric behaviors. Thus, for the variation of a single parameter we considered the nanospiral with 70nm arm width and spacing ranging from 20-40nm, and the 30nm spaced nanospiral, with width ranging from 40-80nm.

Spectrally, increasing a single parameter results in red-shifting all resonances, which correlates with the expected behavior expected when the in-plane surface area increases. The behavior observed when arm width is varied (figure 3.11a) relates to the simple mechanism of increasing damping and increasing extinction with increasing scale.

Variation of arm spacing (figure 3.11b) is a bit more complicated due to its relation to intra-particle coupling. Resonances that are primarily generated by the geometry, such as those in the 700nm to 950nm region and the one at 1200nm, act similar to varied arm width, but the hourglass and other resonances relate more strongly to localized coupling.

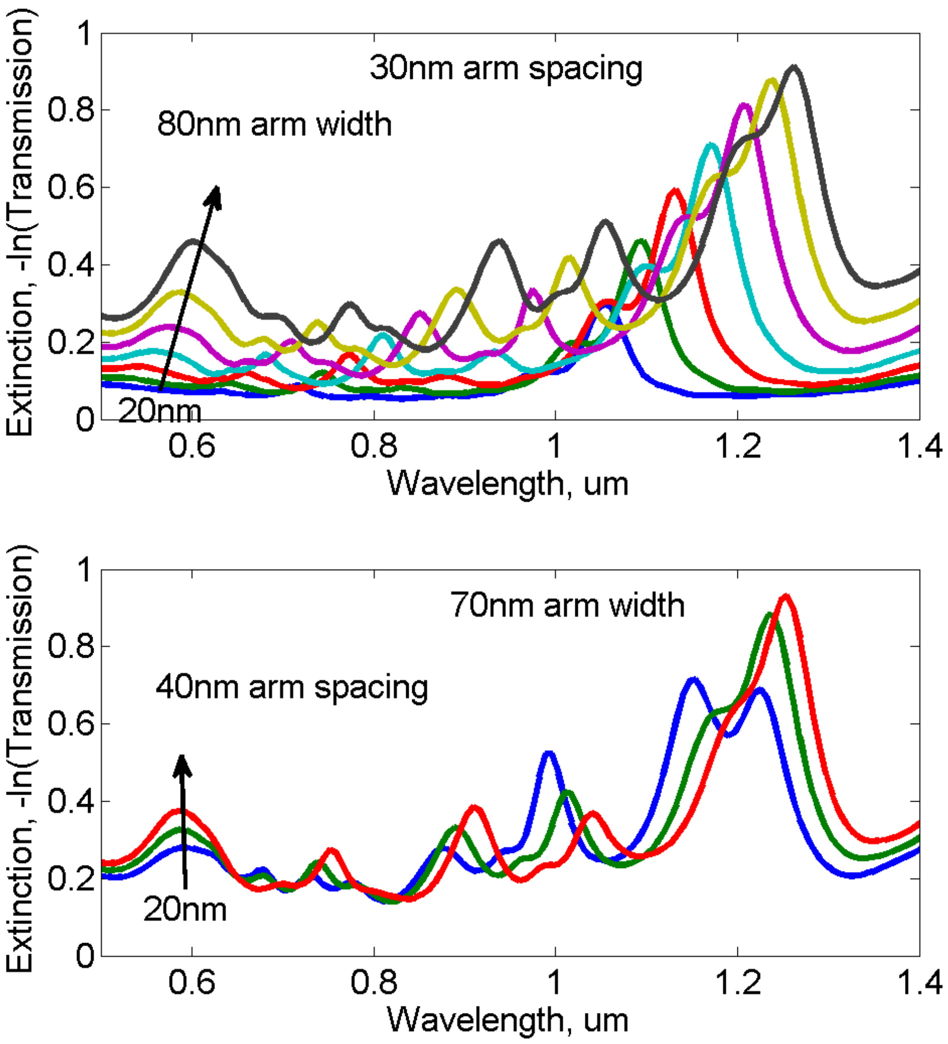

Figure 3.11: a) Sequence of extinction spectra for simulated 4π nanospiral arrays whose arm spacing is 30nm and arm width varied from 20nm to 80nm. b) Sequence of extinction spectra for simulated 4π nanospiral arrays whose arm width is 70nm and arm spacing varied from 20nm to 40nm. Each spiral was excited by white light in the linear polarization aligned with the *y*-axis.

The hourglass resonance displays a lower sensitivity because the chain-of-ellipses mechanism is primarily defined by the size of the particles as they are aligned to the polarization, which is supported by collective enhancement from long range coupling. The other resonances are enhanced or excited due to intra-particle coupling and so decrease with increased spacing.

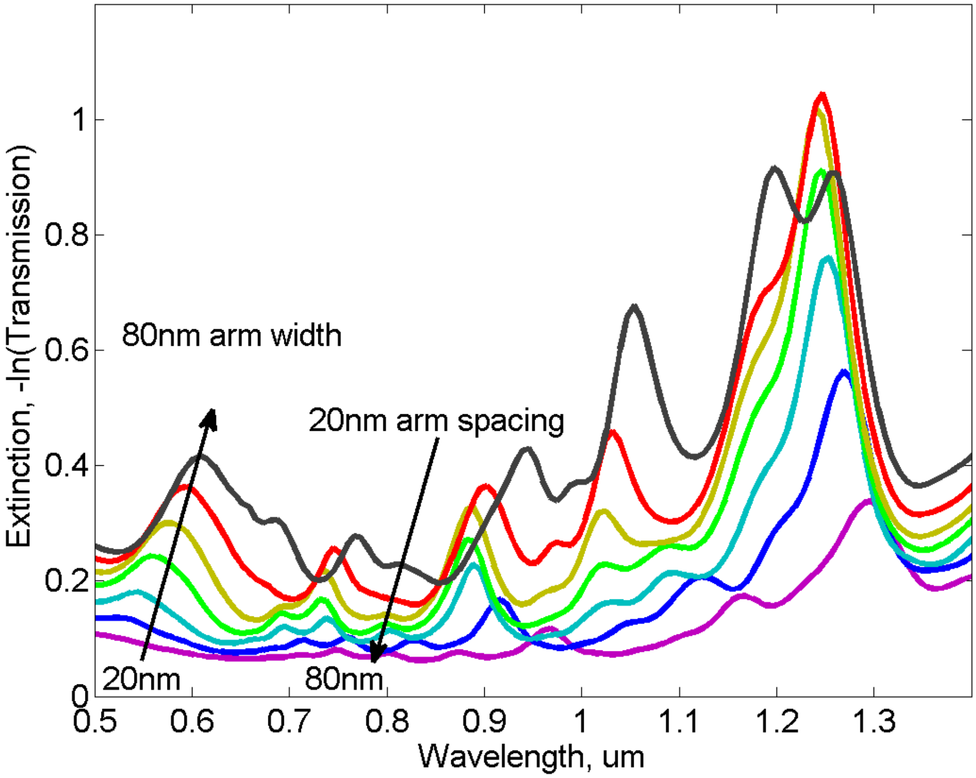

Figure 3.12: Sequence of extinction spectra for simulated 4π nanospiral in a parameter sweep of 4π spirals ranging from 30nm arm width/70nm arm spacing to 80nm arm width/20nm arm spacing, with the common relation 100nm = arm width + arm spacing. Each spiral was excited by white light in the linear polarization aligned with the *y*-axis.

While informative, the first two sets present a convolution of effects from the parameter and from a generate increase in scale, as changes in a single parameter translate to 3 and 4 times the growth in total lateral dimensions, for spacing and width respectively. To correct for this, a third set of nanospiral arrays is compared, defined by the relation 100nm = width + spacing. Without the previous complications (figure 3.12), all non-hourglass elements experience a shift that primarily to describe how the resonant organization of the nanospiral changes and do not suggest any reorganization of the previously mentioned behaviors of the characteristic NF configurations.

Turning to the NF images, we can see where the spectral definitions for where the specific characteristic configurations should be found being to alter. As mentioned previously, we expect there to be a single hourglass resonance, followed by a region where the focusing configuration is dominant, followed by a region where standing-wave resonances exist. Increase in arm width, with nothing else changed, retains the basic organization for the parameters considered, but when arm width and arm spacing get small the regions for focusing and standing-wave reverse. An example of this is the 20nm width/30nm spaced nanospiral array, which has a single standing-wave resonance at 716nm (figure 3.13a) and four focusing resonances positioned at longer wavelengths (figure 3.13b, for an example at 881nm). As the width increases, this reorganization transitions back to the previous order with resonances gradually shifting back to focusing in the lower wavelength regions and, beginning at the longest wavelengths, the region where the standing-wave configuration is dominate grows towards the shorter wavelengths.

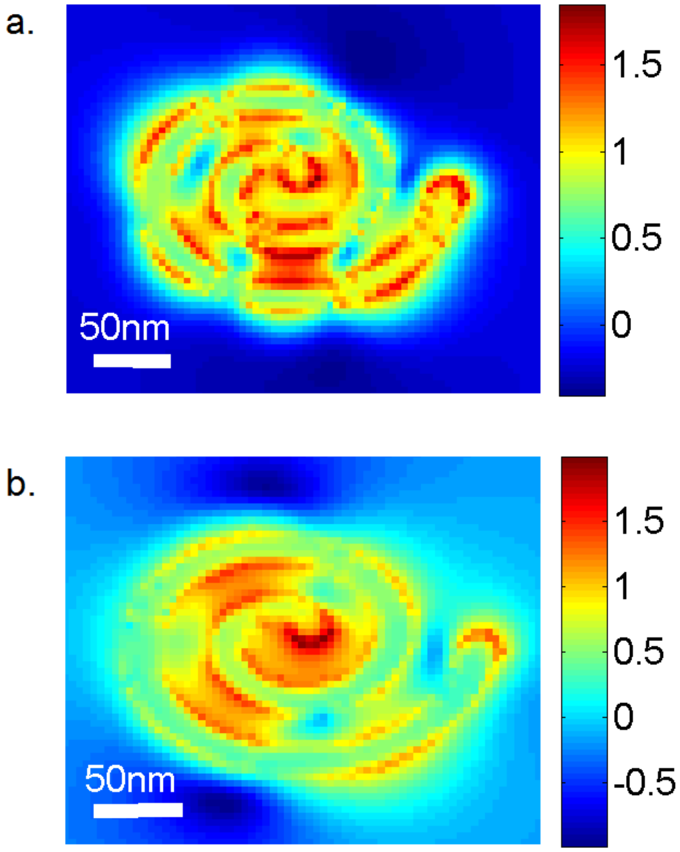

Figure 3.13: NF enhancement images of a simulated nanospiral from an array with 20nm width/30nm spacing at a resonance of a)716nm and b)881nm, showing standing-wave and focusing configurations, respectively. Each spiral was excited by white light in the linear polarization aligned with the *y*-axis.

For nanospirals with very small spacing, most resonances take on a hybrid quality due to increased coupling between neighboring sections of the arm. Figure 3.14 displays this for the resonance of the 70nm wide/20nm spaced nanospiral array at the 874nm resonance. The locations of increased intra-particle coupling are usually aligned with the incident polarization, but why one region, between 1.5π and 3.5π in the case of figure 3.14, is enhanced and not another, such as the region between 0.5π and 2.5π, is not clear. This increase in intra-particle coupling decreases rapidly, with the previously described order returning for spacing greater than 30nm.

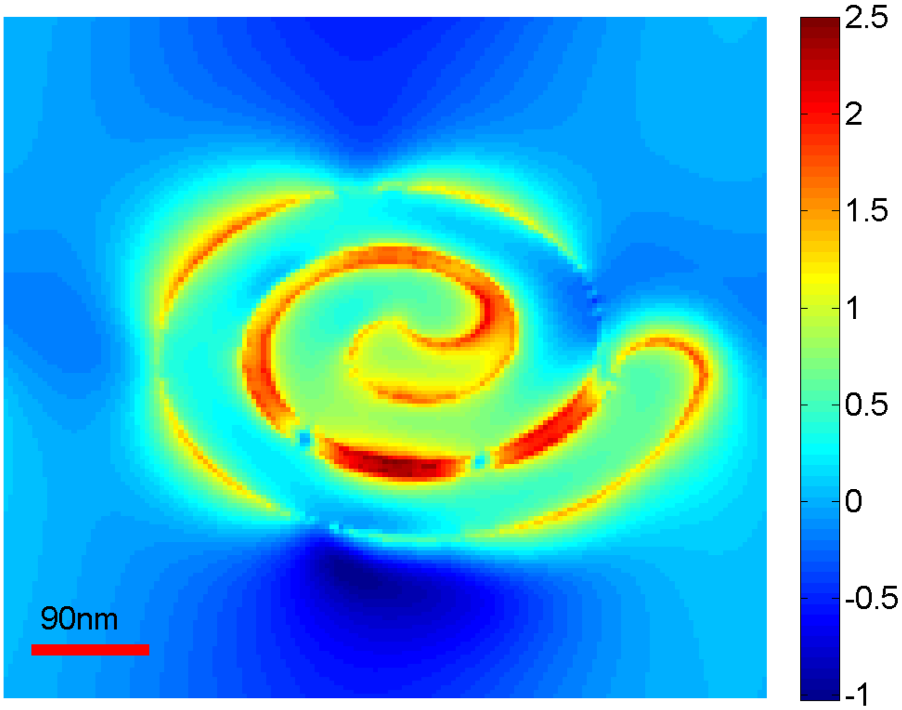

Figure 3.14: NF enhancement images of a simulated nanospiral from an array with 70nm width/20nm spacing at a resonance of 874nm. The array was excited by white light in the linear polarization aligned with the *y*-axis.

In conclusion, the nanospiral arrays retain a logical, well-behaved organization of configuration preference over a range of 30nm to 80nm arm spacing and 40nm to 80nm arm width, as long as the alternate parameter in each case is not significantly larger or smaller, respectively.

3.4 Effects of array pitch and thickness

The final parameters controllable with EBL, array pitch and thickness, affect the nanospiral arrays in the same manner as they affect more simple geometries. The thickness of any nanoparticle (NP) array defines the fundamental restoring force of the plasmonic oscillations, with thicker particles having a larger immobile ionic lattice to pull on the polarized conduction electrons. Thus, increased particle thickness relates to a more significant red-shift of all resonances, which is true for all NP arrays regardless of geometry.

Array pitch is relates to a more complicated mechanism because it mediates long range inter-particle coupling. This coupling can significantly modify the lineshape, by modifying the decay time of particular resonances, and the resonant position, by coupling to grating resonances. The response of the nanospiral array, displayed in figure 3.15 for the 60nm width/40nm spaced nanospiral, is similar with a few notable additions due to unique features of the spiral. Similar to any plasmonic array, an increase in array pitch reduces the packing density and lowers the total amount of particle interactions, especially in the case of an illuminating beam spot that is smaller than the array. Unlike most other geometries, the multiple resonances and generating mechanism of the nanospiral react differently to the alteration. The hourglass resonance, with its higher energy and strong NF coupling, is not affected while the focusing resonances are shuffled in small increments to first increasing and then decreasing wavelengths. The standing-wave resonances act similarly, but one resonance is provoked at the 650nm array pitch. This resonance is attributed to a coupling between a long range, grating resonance and a nanospiral resonance that is much weaker, to the point of being nearly dark, without the array enhancement.

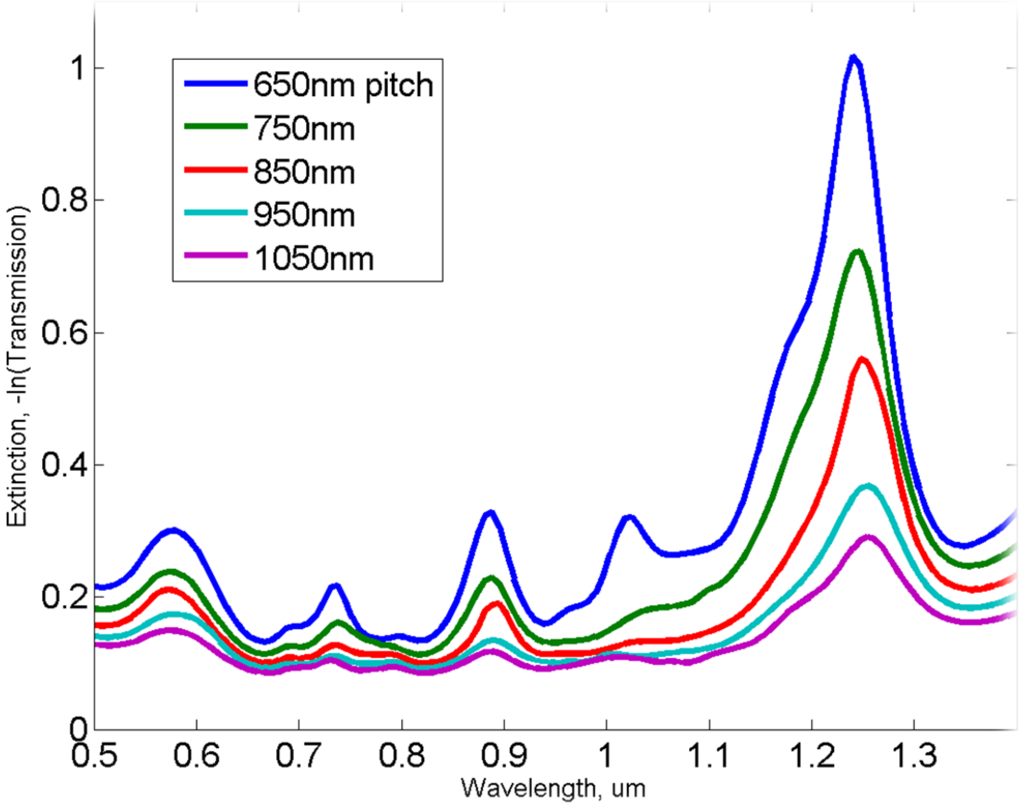

Figure 3.15: Sequence of extinction spectra for arrays of simulated 4π nanospirals with arm width of 60nm and arm spacing of 40nm and with the array pitch varied from 650nm to 1050nm, in 100nm steps. Each spiral was excited by white light in the linear polarization aligned with the *y*-axis.

3.5 Conclusion

In conclusion, we have defined the fundamental organization that is generated in arrays of Archimedean nanospirals. These arrays present complex and diverse plasmonic system, which contains the components of a useful and practical plasmonic toolbox: independently variable spectral elements together with regions of clearly identifiable near-field plasmonic field enhancements. The nanospiral supports a significant number of resonant elements that self-organize into regions that are calculable from geometric features of the spiral geometry, are spectrally tunable *via* the winding number, and remain reasonably stable under lithographic variations in arm width and spacing. Furthermore, the specific near-field structures that operate over the same *spatial* regions and adjacent *spectral* regions, allow for versatile manipulation of the time-varying surface charge distributions. For fundamental plasmonic research, the spiral is a single particle laboratory for exploring complex intra-particle interactions between modes and substructures compressed into adjacent near-field regions. For applications, the sub-wavelength spiral is large enough to be a substrate for molecular and biological interactions in which the electronic properties of sub-regions can be spectrally modulated as defined by the near-field topography of each mode. This makes the spiral geometry an ideal platform for advanced application such as a molecular manipulator/trap or spatially selective plasmon catalyst.

CHAPTER IV

QUANTITATIVE ANALYSIS OF NANOSPIRALS

4.1 Complications with spiral analysis

In the previous chapter the behaviors of the fundamental plasmonic configurations were presented in a qualitative manner; this chapter reconsiders these fundamentals in a quantitative manner by first, reducing the three-dimensional data of a near-field (NF) image to a two-dimensional data set in order to develop a tool to directly compare different resonances and second, developing a figure of merit to standardize a clear definition for the standing-wave and focusing configurations and the resonances that display a hybridization of the two configurations.

Reducing the dimensionality of the displayed data for an individual resonance serves to simplify the large amount of information contained within a single NF image, while preserving the spatial organization of NF enhancements. This is accomplished by assigning a representative enhancement value for discrete winding numbers along the spiral arm, from the inner end to the outer. This is complicated by the field enhancements from azimuthally adjacent sections of the spiral arm and the lack of a unique coordinate basis set related in a one-to-one mapping onto the winding number.

To overcome these geometric complications, an axis is defined along the center of the spiral arm, as well as a perpendicular axis at each point, that relates the representative enhancement along the inner arm to its counterpart along the outer arm, which is located at the same winding number. The representative enhancement factor is defined by the NF enhancement of pixels in close proximity to the corresponding side of the spiral arm at the respective winding number, which avoids the incorporation of enhancement from neighboring sections.

The functionality of this metric is put to further use when assigning the figure of merit that defines the degree to which a resonance is a focusing or a standing-wave configuration. As eluded to in chapter 3, the characterstic configurations establish a basis set for possible NFS. However, nanospirals within the parameters considered here are not limited to distinct manifestations of a single configuration. Superpositions of the focusing and standing-wave exist such that no clear definition can be established to group all resonances as either standing-wave or focusing. By assigning a numerical definition of each configuration, the large number of resonances generated in a single geometric or polarization parameter sweep can be directly compared and limits can be established that clarify the degree of focusing to standing-wave behavior.

This will facilitate a better understanding of the nuances and mechanisms of the nanospiral, as well as presenting another tool to precisely control the desired near-field structure (NFS) of both drawn and fabricated nanospirals. In this chapter, all methods will be presented using drawn spiral geometries.

4.2 Path definition and interpolation

The first step to reduce the dimensionality of any nanospiral NF image requires the definition of two paths, the inner and outer arm paths. Once these paths are defined, each point of the inner-arm path can be related to points along the outer-arm path and to the correct winding number. Finally, points along the path will be related to points within the

NF image, which will be summed to give the representative enhancement at a given winding number for the corresponding side (inner or outer) of the spiral arm.

Definition of the paths begins with the image of the index of refraction throughout an xy-plane that represents a cross section of the simulated nanospiral geometry, an example of which is displayed in figure 4.1. This image is loaded into a Matlab® program, along with the coordinates for the center of the spiral, and the pixels that correspond to the nanospiral are acquired by applying a high pass filter. The pixels that represent the edge of the geometry are isolated through the embedded Matlab® function, *edge(data,method)*. This function returns a two-dimensional binary array, which is the same size as the original data array, with non-zero values representing the pixel locations that are the edge of the nanospiral. For the purposes of this work, the edge pixels were found using the Canny edge detection method, which convolves the filtered image with a second filter generated from the x- and y- derivative of a Gaussian function and finds inflection points. The resulting two-dimensional, binary matrix, displayed in figure 4.2, is then converted in to a list of coordinates, which is the list of edge pixels.

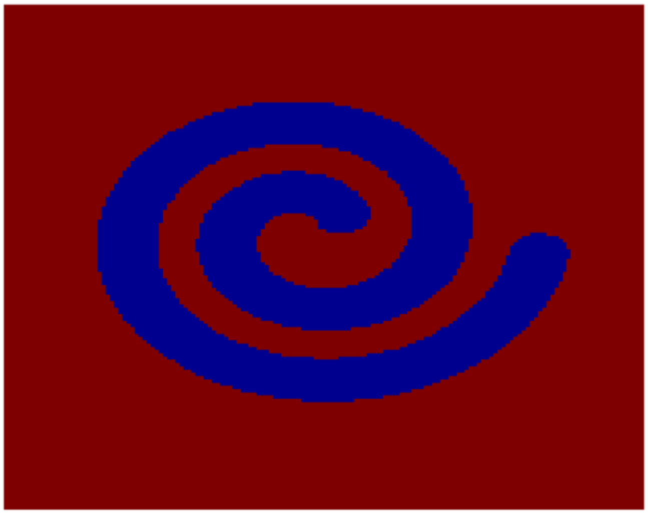

Figure 4.1: Image of the index of refraction for a simulated 60nm spaced, 40nm width nanospiral. The red region is void and the blue region is Au.

Figure 4.2: Image of the edges of the same nanospiral as in figure 4.2 using the Matlab® defined *edge* function. The white line represents the edge of the nanospiral.

At this point the coordinate list represents an unorganized group of all points that will form the inner and outer side paths. To organize this list into the two sequential paths, the pixel that is positioned at the cap of outer end of the spiral arm is located by a two-step process. This process uses additional input concerning the direction and position of the outer end, which for the purposes of this narrative about a 4π, clockwise-winding spiral, is located on the right side of the spiral and directed in the positive *y* direction. The two-step process first finds the pixel that has the highest value in the *x* direction (the right most pixel); then, using a nearest-neighbor search, the program tracks neighboring pixels in the upward (positive *y*) direction till a maximum is found. This maximum point is the terminal pixel of the outer end of the spiral arm. With the outer end established, the same nearest-neighbor search is used to track pixels, along both the inner and outer paths, towards the center in a counter-clockwise direction.

To establish the correct winding numbers for each pixel, the counter-clockwise search is broken into steps of 2π where each pixel first assigned a value from 0 to 2π in regular polar coordinates and then the polar value is corrected by adding 2π until the polar value rotates past the positive *x*-axis. As a result, two paths of pixels are now well-defined, and are displayed in figure 4.3 for the example in this chapter.

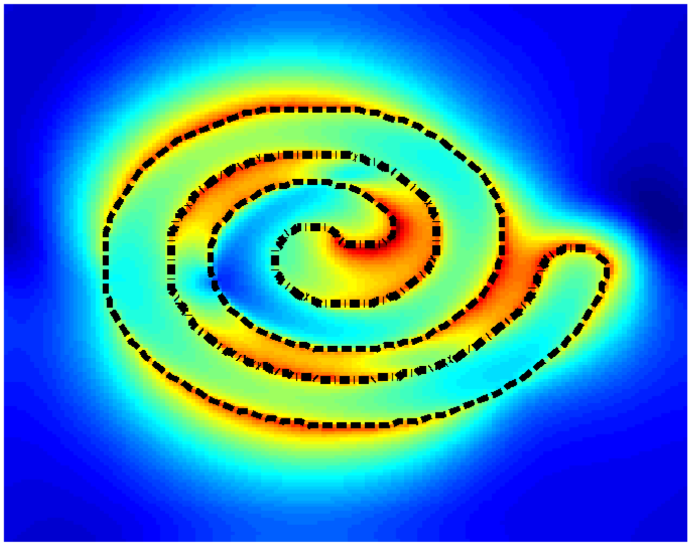

Figure 4.3: NF enhancement image of the 1240nm resonance for the nanospiral featured in figure 4.1 with lines representing the inner and outer path of the nanospiral arm, as it is seen by the path defining program. The dashed line follows the outer arm and the dash-dotted line follows the inner line.

The last step to reduce the dimensionality of the NF images requires a definition of the representative enhancement at each pixel along the path. The close proximity of neighboring sections of the arm complicates the definition, especially since this computational program must be robust against significant variations in the arm spacing parameter. To avoid the inclusion of enhancement from an azimuthally neighboring region of the spiral, a 3x3 pixel region, equivalent to a 12nm x 12nm block, was chosen.

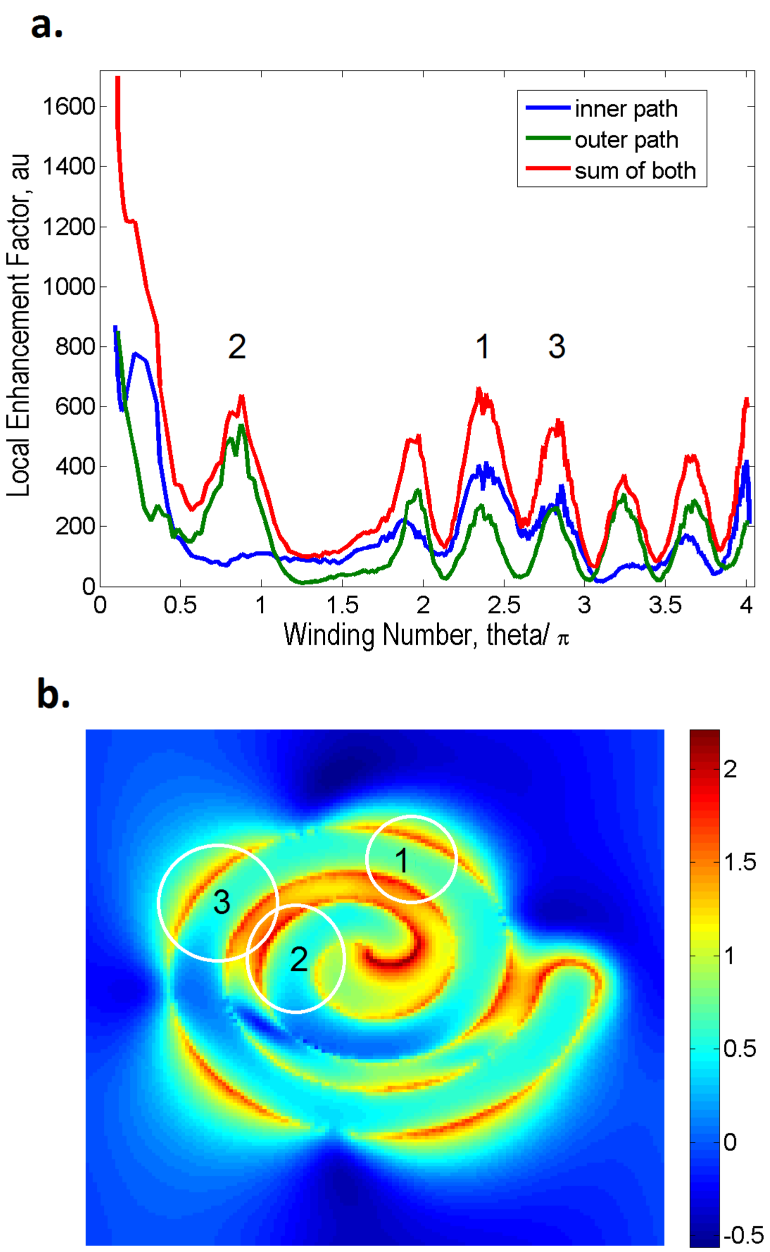

Figure 4.4: a) A line plot of the dimensionally reduced NFS of the spiral featured in figure 4.1 at the 1018nm resonance for the inner, outer and summed paths. b) A NF enhancement image of the same spiral at the same resonance.

In smaller blocks it is possible to lose the point of highest enhancement for a particular winding number, which happens if the edge finding algorithm chooses a pixel just inside the physical structure; if the area is any larger, the overlap between neighboring edge pixels becomes significant. An example of a NF image and its dimensionally reduced inner and outer path scans are shown in figure 4.4. The path composed of the sum of the inner and outer paths requires one extra step of processing, due to the larger number of resolved pixels on the outer path compared to the inner.

The primary purpose of this method is to display multiple resonances for quantitative comparison of the organization of NF enhancements on either side of the spiral arm. Separating the inner and outer paths makes it possible to more easily identify the dominant electromagnetic-field enhancement mechanism that gives rise to a particular resonance. As illustrated in figure 4.4, nodes of NF enhancement can be present at a particular winding number in either or both paths. If the node is present in both paths, this implies that the node is related to a mechanism that generates the characteristic configuration, such as a node in the standing-wave configuration as illustrated at region 1 in figure 4.4. If a node in a given region is located only on one side, this feature is generated by intra-particle coupling between neighboring azimuthal regions. This is verified by locating a corresponding node at a position on the opposing side. The nodes marked as 2 and 3 in figure 4.4 are examples of intra-particle coupling, which are identified and highlighted by this reduced-dimensionality method.

4.3 Figure of merit

The dimensionality-reduction protocol described in the previous section helps to compare specific differences between resonances of different NFSs, but a two-dimensional data set is still too detailed for comparison between all resonances of a nanospiral or for describing the evolution of a particular element across a parameter sweep. To further simplify the data set, a single numerical figure of merit that defines the degree to which a resonance is focusing or standing-wave is desired. Since the hourglass configuration appears only once for a particular nanospiral and maintains the hourglass shape, the figure-of-merit is irrelevant to that resonance and will not be calculated.

The optimal method of distinguishing, and quantitatively defining, the focusing and standing-wave configurations relies on the degree to which the majority of the summed enhancement is accumulated in the inner region of the spiral. For the case of the 4π spiral, this is the region from 0 to 2π. This figure of merit, σ, is defined as:

$$\sigma = \frac{\sum_{\omega=0}^{2\pi} ref_{inner}(\omega) + ref_{outer}(\omega)}{\sum_{\omega=0}^{4\pi} ref_{inner}(\omega) + ref_{outer}(\omega)} \tag{4.1}$$

which is the sum of all representative enhancement factors, *ref*(*ω*) along both the inner and outer paths for winding numbers from ω = 0 to 2 π, divided by the sum of all representative enhancement factors along both the inner and outer paths for winding numbers from ω = 0 to 4π. For nanospirals with smaller winding numbers, as low as 3π, this value would be the region that has an azimuthally neighboring region at a larger radius; for even smaller nanospirals, this value is roughly half the total winding number of the nanospiral.

Based on visual comparison of NF images for various resonances, the following limits establish values of σ corresponding to particular states: σ > 0.5 is totally focusing, σ < 0.43 is dominated by the standing-wave configuration, and 0.43<σ < 0.5 is a superposition of the two configurations. Figure 4.5a compares values of σ for the 60nm width/40nm spaced nanospiral array and figure 4.5b displays an example for each of the three states, whose resonances are located at 795.2nm, 888.5nm and 1018nm. The values of σ for these three resonances are 0.5657, 0.4818, and 0.3841, respectively.

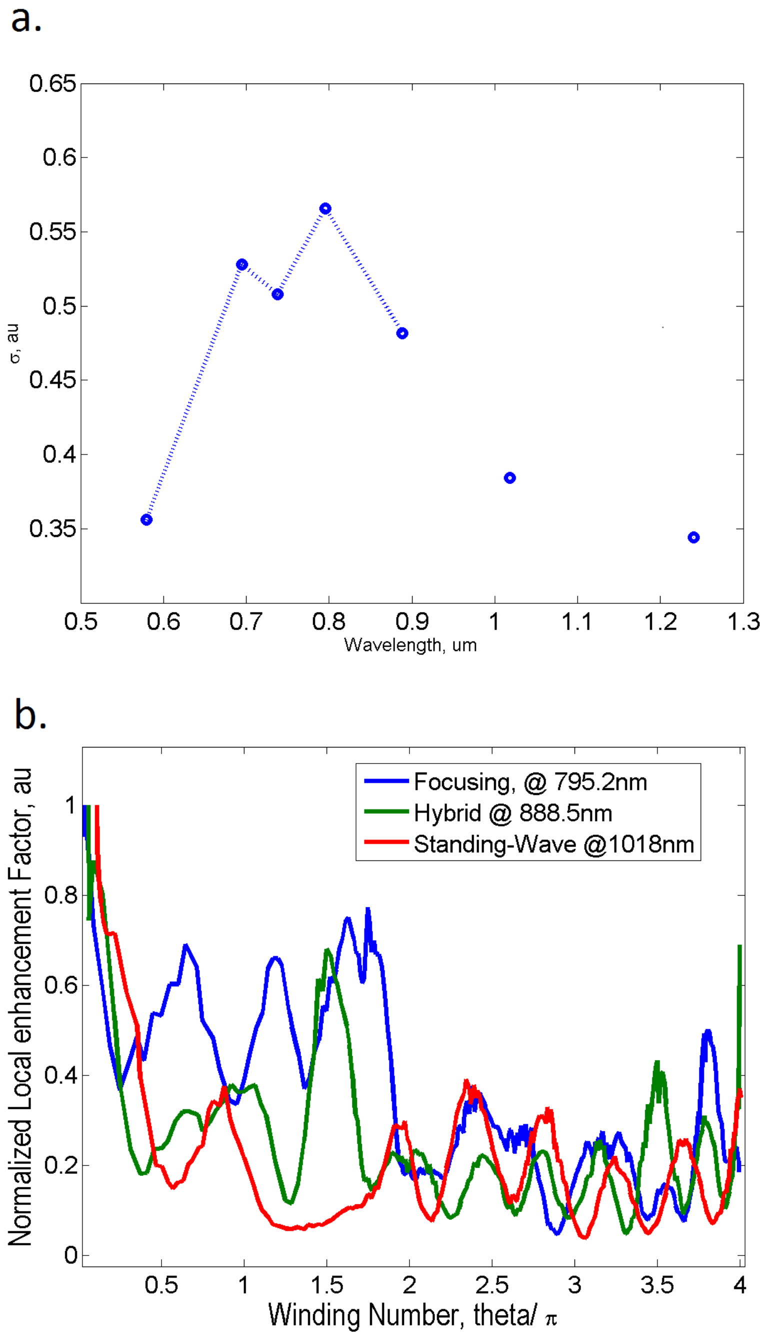

Figure 4.5: a) Values of σ for resonances generated by an array of 60nm wide, 40nm spaced nanospirals excited by linearly polarized white light aligned with the *y*-axis. b) A

line plot of the dimensionally reduced NFS of the summed paths for selected resonances featured a).

The resonances enclosed between the limits of dominant focusing or standing-wave configurations represent either a weighted superposition of focusing and standing-wave configurations, or a standing-wave configuration with a large enhancement node located at the inner end of the spiral arm. An example of the former is the resonance at 888nm, which has a σ of 0.4818, is located in figure 4.5; the distinguishing feature between to the other states is the peak at 1.5π that shifts the majority of this otherwise standing-wave configuration. The latter configuration displays much more exaggerated behavior with the cap of the inner end contributing a significant increase in enhancement. Again, this configuration is similar to a standing-wave configuration, but the perturbation is centralized such that the peak can be greater than all other locations in the spiral by more than a factor of four. An example of this state is the resonance at 1025nm for the 50nm width/50nm spaced nanospiral array, displayed in figure 4.6.

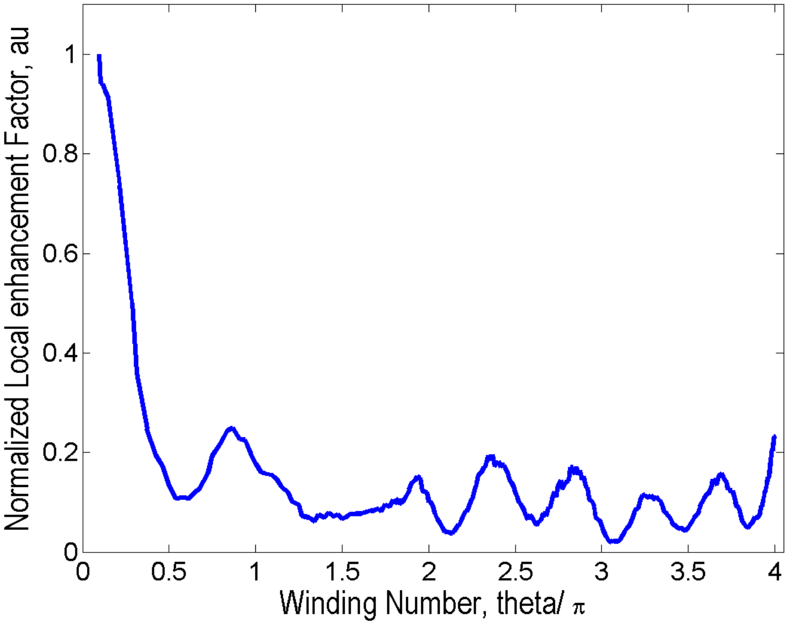

Figure 4.6: A line plot of the normalized, summed paths of a dimensionally reduced NFS for nanospiral located in an array of 50nm width, 50nm spaced nanospirals at the 1025nm resonance, excited by linearly polarized white light aligned with the *y*-axis.

4.4 Conclusion

The creation of the reduced-dimensionality method and σ are necessary tools for displaying and quantitatively analyzing resonances of the nanospiral resonances. Most popular methods and figures of merit, such as quality factor and effective mode volume, are not sensitive to the spiral geometry and are not capable of distinguishing different configurations. As an example, figure 4.7 shows the effective mode area for resonances of the sample nanospiral used in the previous sections, which is a measure of the degree of delocalization of the total enhancement from a central point. It is evident that A_{eff} is not sensitive to the differences between configurations and cannot significantly distinguish the focusing configurations, such as the similar focusing resonances located at 694nm and 738nm, and standing-wave configurations, such as the resonance located at

1018nm. The tools presented in this chapter will allow for a broader consideration of variations in both geometric and polarization parameters and will assist in precise tuning to a desired NFS in future applications.

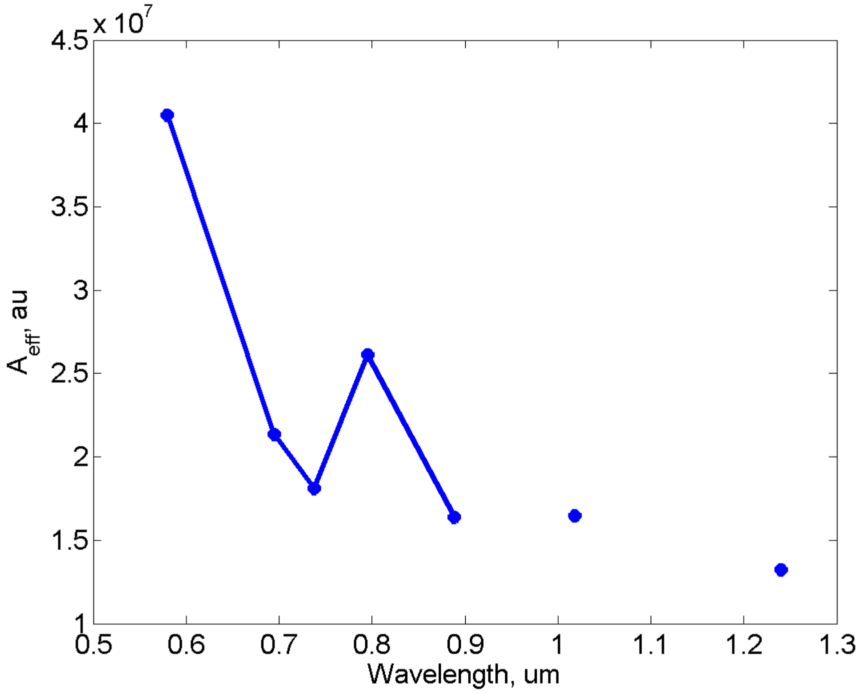

Figure 4.7: Line plot of the effective mode area, A_{eff}, for resonance generated by an array of 60nm wide, 40nm spaced nanospirals excited by linearly polarized white light aligned with the *y*-axis.

CHAPTER V

POLARIZATION MODULATION IN NANOSPIRALS

5.1 Potential of polarization control

This chapter expands the characterization of the nanospiral by investigating the changes in spectral and spatial organizations; this includes all angles of linear polarization as well as the circular polarizations. The spectral response of all the linear polarizations, when superimposed, presents the total population of possible resonances for geometry, ignoring the darkened resonances that are preferred along specific orientations. Furthermore, comparison of the near-field structure (NFS) for resonances that remain spectrally stationary at different angles will assist in connecting specific mechanism to the resonance. Illumination with circularly polarized light probes the chiral response of the systems and illustrates the advantages of the winding geometry. We observe a strong chiral dependence with the NFS fully reconfiguring and a new characteristic configuration.

Together, modulation of the angle or rotation of the incident polarization presents a method of tuning the plasmonic behavior of a single nanospiral array. This suggests applicability in systems that require fast repositioning of electric field enhancements, such as with optical computing, or systems that would enhance another process to a similar degree regardless of polarization, such as combined SERS and OA-SERS systems. Furthermore, significant tuning can be achieved with a single source and a filter, which vastly simplifies integration into existing tools/sensors.

For this work, outward circular polarization will be referred to as the circular polarization that rotates in the same direction as the spiral winds outward and the opposite circular polarization will relate to rotation oriented towards the center of the spiral. Thus, this defines left-handed circular polarization (LCP) the outward polarization and right-handed circular polarization (RCP) the inward polarization.

5.2 Rotating the linear polarization

Using both fabricated and simulated nanospiral arrays, we rotated the linear polarization in sub-15 degree steps to probe the subtle changes in broken symmetry that are produced along different axes of the nanospiral. To ensure the observed behavior is

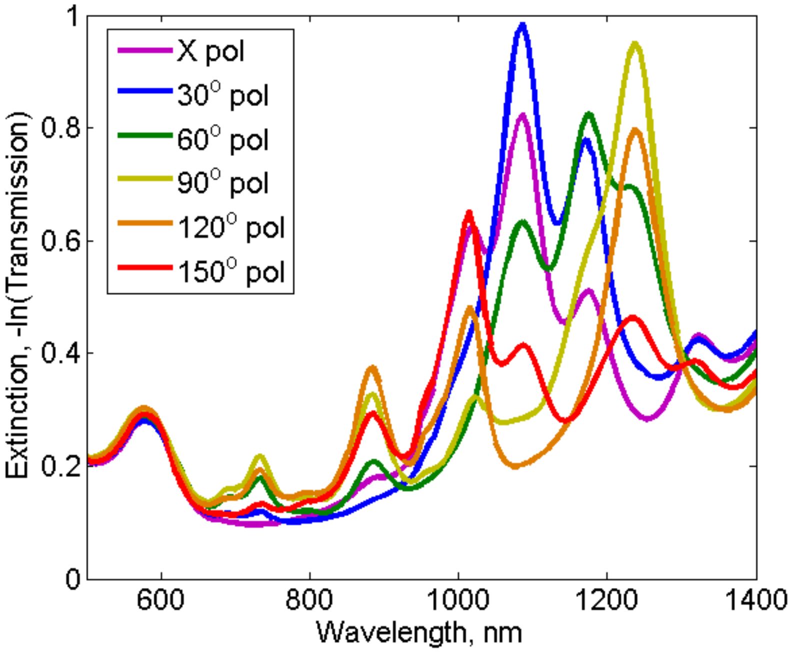

Figure 5.1: A sequence of simulated extinction spectra for a nanospiral array with arm width of 60nm and arm spacing of 40nm. The sequence steps through different alignments of the incident polarization with respect to the spiral, with 0 degrees set as the *x*-axis.

attributable to the spiral geometry and not perturbations due to the fabrication methods, we consider first the simulated spirals that are generated with smooth sides. The spectral response is displayed in figure 5.1 for an array of 60nm wide/40nm spaced simulated nanospirals.

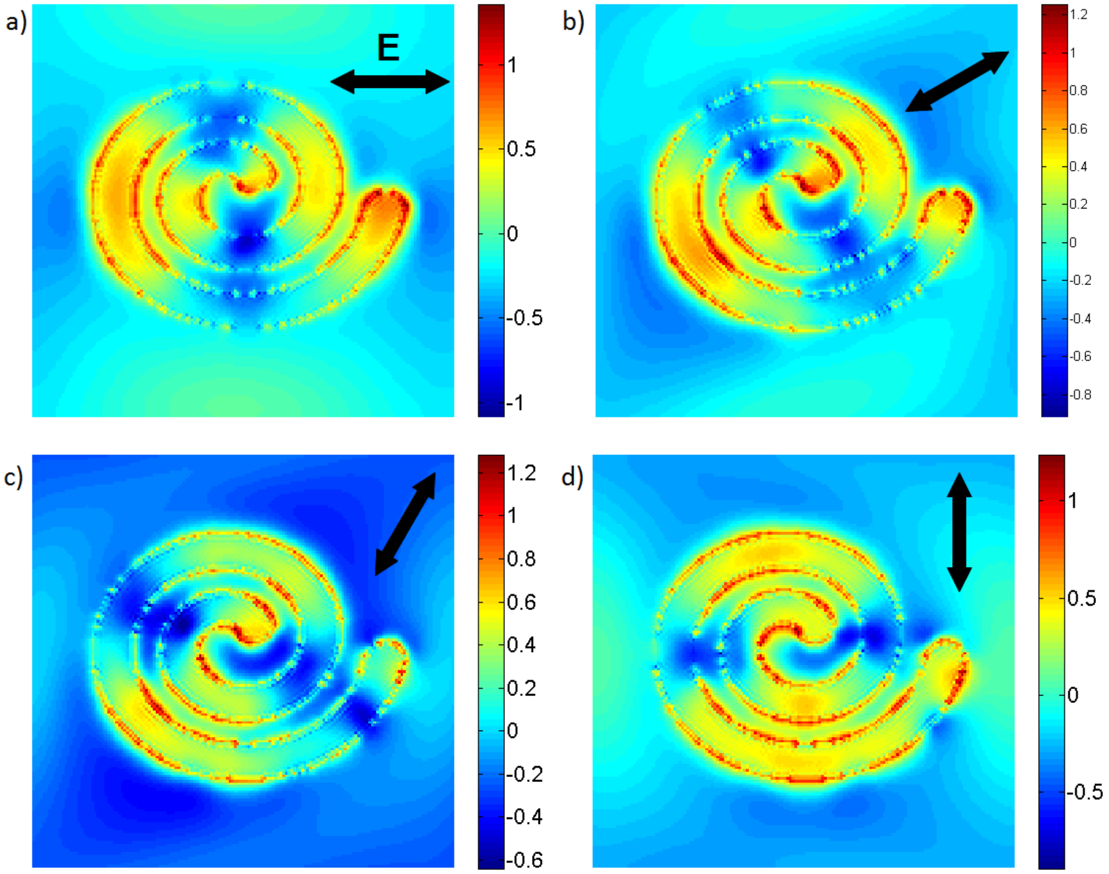

Figure 5.2: Near-field enhancement images of the hourglass resonance, located at 578nm, for the nanospiral array with arm width of 60nm and arm spacing of 40nm. The images are generated from incident polarizations at a)0 degrees, on the *x*-axis, b) 30 degrees, c) 60 degrees, and d) 90 degrees.

Two main behaviors are apparent in the extinction spectra; the hourglass resonance remains unchanged, and all other resonances remain spectrally stationary while the extinction coefficient varies dramatically. This distinction is a result of the fundamental difference between the mechanism that generates the hourglass configuration and the mechanisms for all other resonances. The intra-particle coupling between azimuthally neighboring arms treats the spiral as a near-symmetric system insuring that the spiral preserves the relative NFS of the hourglass configuration as it rotates to follow the rotation of a linearly polarized beam, as illustrated in figure 5.2.

As the polarization rotates, the hourglass reorients with little change to the total organization of the NFS, except to fill the obvious asymmetrical feature of the ends of the spiral. Both ends generate enhancements comparable to any other enhanced region of the spiral regardless of the polarization orientation. These ends should be the source of any behavior that would differ from either the mechanism of the hourglass configuration or a circularly symmetric system. This would manifest as a preferred polarization that optimally couples, resulting in an increase the maximum near-field (NF) enhancement, even if the extinction coefficient is not significantly changed. Figure 5.3 displays the maximum NF enhancement and extinction coefficient at the peak of each resonance for a few different resonances as the polarization is rotated and suggests no preference of optimal coupling along the 0^{o} axis, which includes both ends. This unexpected stability proves that the hourglass mechanism supersedes even the geometric preferences that are observed with the other configurations and explains the exceptional stability against geometric parameter variation that was observed in chapter 3.

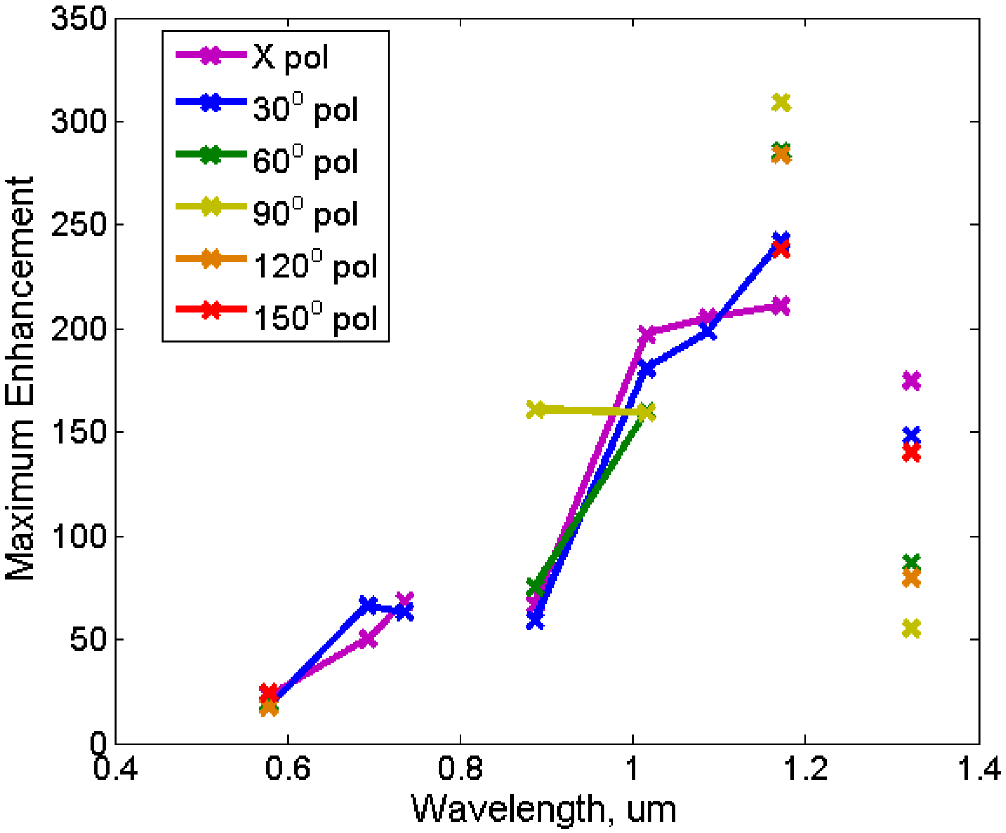

Figure 5.3: A spectrally resolved map of the maximum NF enhancement for the nanospiral array with arm width of 60nm and arm spacing of 40nm at each resonance as the incident polarization is rotated from 0 degrees, along the *x*-axis, to 150 degrees.

In sharp contrast, the other resonances do react to the rotation of the linear polarization, as expected due to the geometrically sensitive nature of their mechanisms. As shown in figure 5.1 and figure 5.3, the extinction factor and maximum NF enhancement for each resonance has an optimal alignment at a particular polarization angle, while the spectral position remains stationary, just as it would for a nanorod. The two distinct axes of symmetry in the nanorod have a preferred resonance, which maximizes both the extinction coefficient and the maximum NF enhancement, and darkens the other resonance. The nanospirals have a similar geometric darkening with resonances having optimized position dispersed along different angles, but the symmetry around the optimal position is significantly different. While the maximum NF enhancement decreases in a symmetric manner around the optimal angle, similar to a reduced symmetry geometry like the nanorod, the extinction coefficients for certain resonances decrease much faster in the counter-clockwise direction. An example of this behavior, for multiple resonances of the 60nm width/40nm spaced spiral, is illustrated in figure 5.4. The asymmetry of the extinction coefficient relates to the fundamental chirality of the spiral geometry, while the NF enhancements show a stronger connection to the near-circular symmetry that also affects the hourglass configuration.

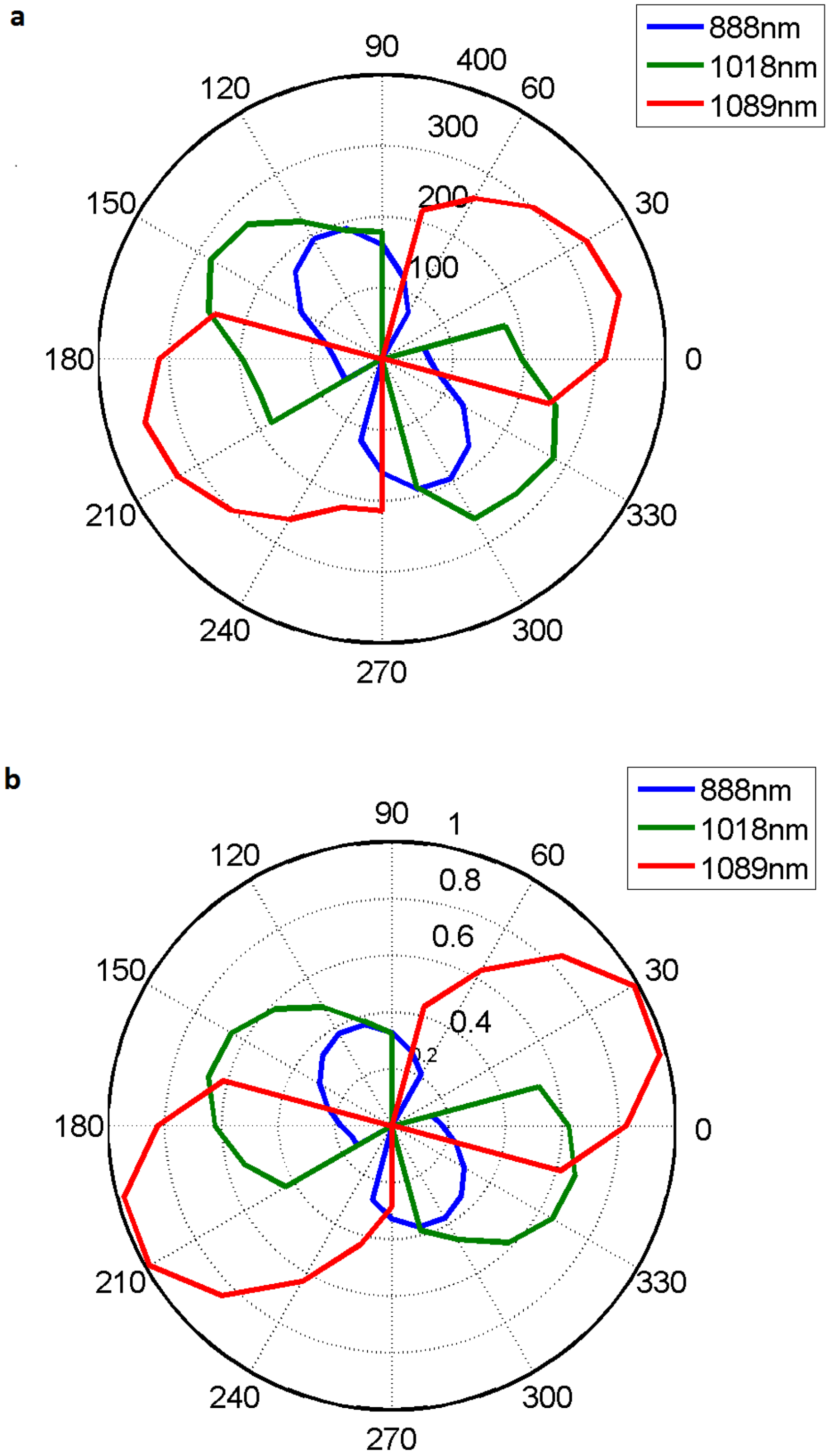

Figure 5.4: A line plot, set to the polar coordinate corresponding to the incident polarization angle, of the a)maximum NF enhancement and b) maximum extinction for the nanospiral array with arm width of 60nm and arm spacing of 40nm. Each plot presents two standing-wave resonances, at 1018nm and 1089nm, and a focusing resonance, at 888nm.

Experimental investigations illustrate that the longer wavelength resonances are actually more sensitive than the simpler geometries. We observe slight spectral shifts for certain resonances as the polarization is rotated, as illustrated in figure 5.5 for a ~65nm wide/35nm spaced experimentally observed spiral array. The shift of the ~1050 nm resonance, labeled point 1, is attributed to a sensitivity to the slight deformations during fabrication that cause regions of the spirals to have slightly different widths or spacings that, in turn, that break the near-circular symmetry, compared to the non-deformed, simulated spirals, to shift the peak position as the polarization turns.

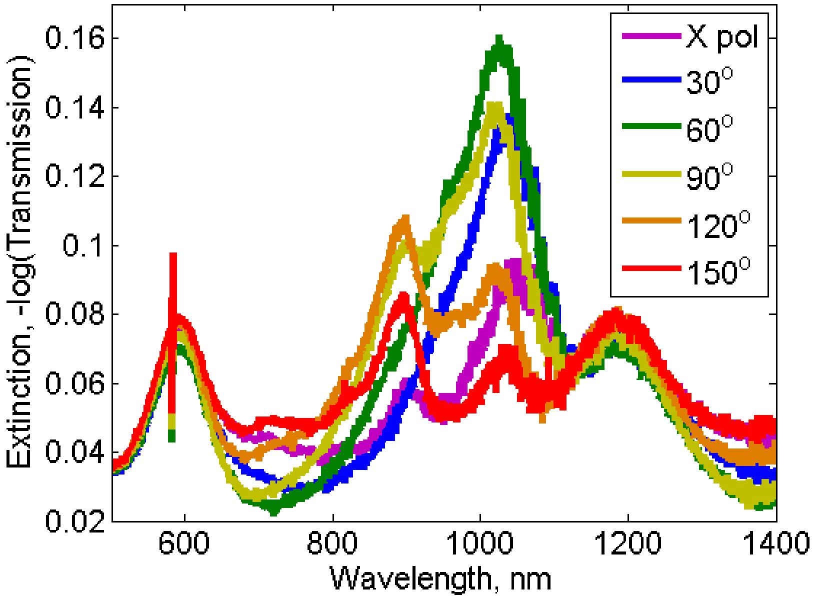

Figure 5.5: A sequence of extinction spectra for a fabricated nanospiral array with arm width of ~65nm and arm spacing of ~35nm. The sequence steps through different alignments of the incident polarization with respect to the spiral, with 0 degrees set as the *x*-axis.

In summary, the use of rotated linear polarization is a method for probing the subtleties of how the resonances of systems with no internal symmetry, but clear geometric order, are organized. Furthermore, comparing the spectra of the rotated systems to the circular polarizations, displayed in figure 5.6, we see that the circular polarizations excite all resonances. This illustrates the circular preference of the system, similar to the linear preference of the circularly symmetric systems whose extinction spectra are populated by all bright modes regardless of the orientation of the linear polarization.

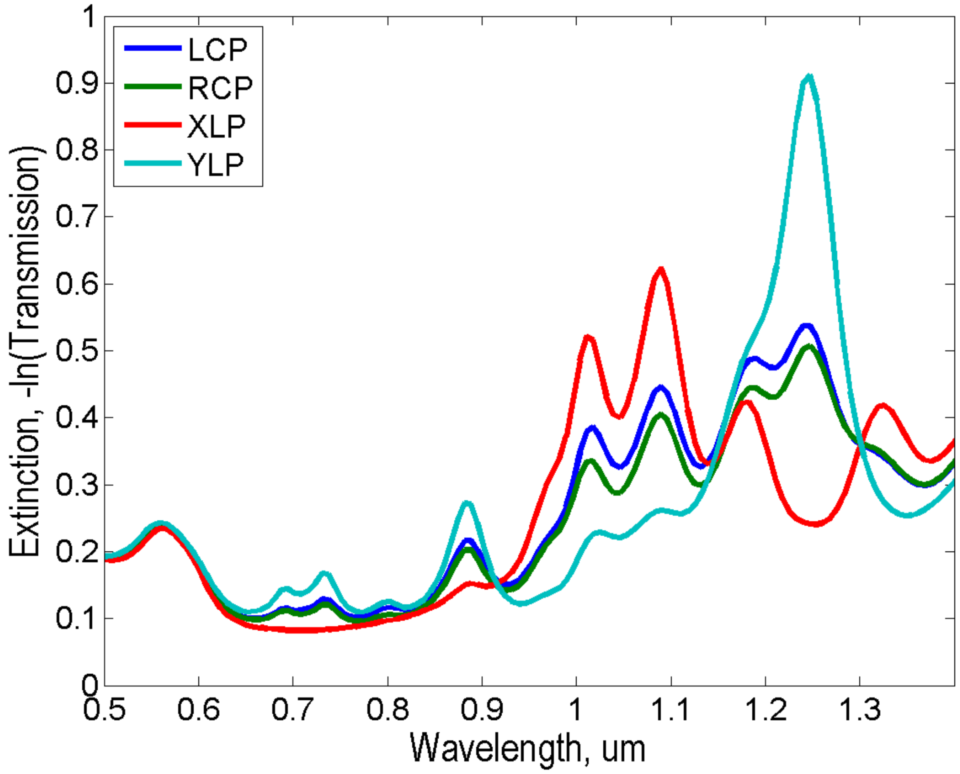

Figure 5.6: Simulated extinction spectra of the nanospiral array with arm width of 60nm and arm spacing of 40nm at both orthogonal linear polarizations and both circular polarization.

5.3 Inward circular polarization

We next consider the inwardly oriented circular polarization, RCP, to further probe the chiral behavior of the nanospiral. The excitation of all linear resonances, as illustrated in figure 5.6, suggests that circular polarizations may simply be superposition of the linear behavior. However, previous work with other chiral geometries has shown that different NFSs are generated for each circular polarization.[61, 76] Nanospirals respond similarly for RCP by significantly reconfiguring of the NFS.

The resonance that would normally produce the hourglass configuration remains with an extinction coeffiecent similar to the linearly excited resonance, but the mechanism that generates the NFS is not compatible with circular polarizations. Thus the near-field enhancements are aligned along the edges of the spiral, as displayed in figure 5.7, losing all unique organization of the hourglass configuration while changing the σ of the resonance less than 3%.

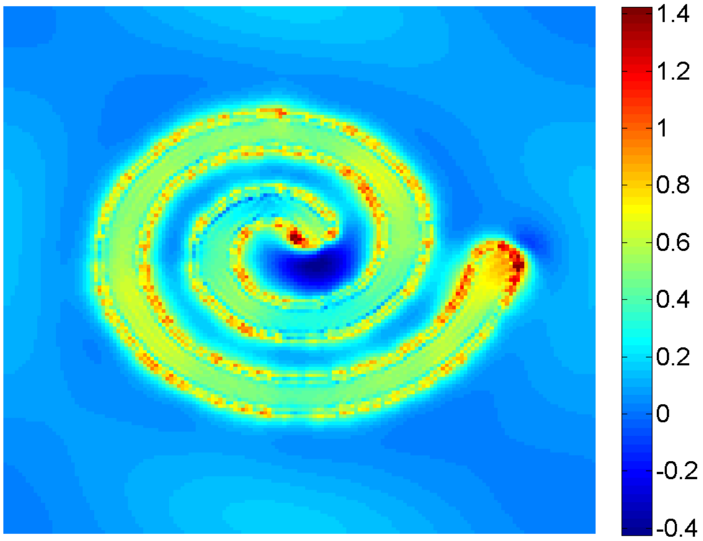

Figure 5.7: A NF enhancement image of the 578nm hourglass resonance for the nanospiral array with arm width of 60nm and arm spacing of 40nm when excited by RCP white light.

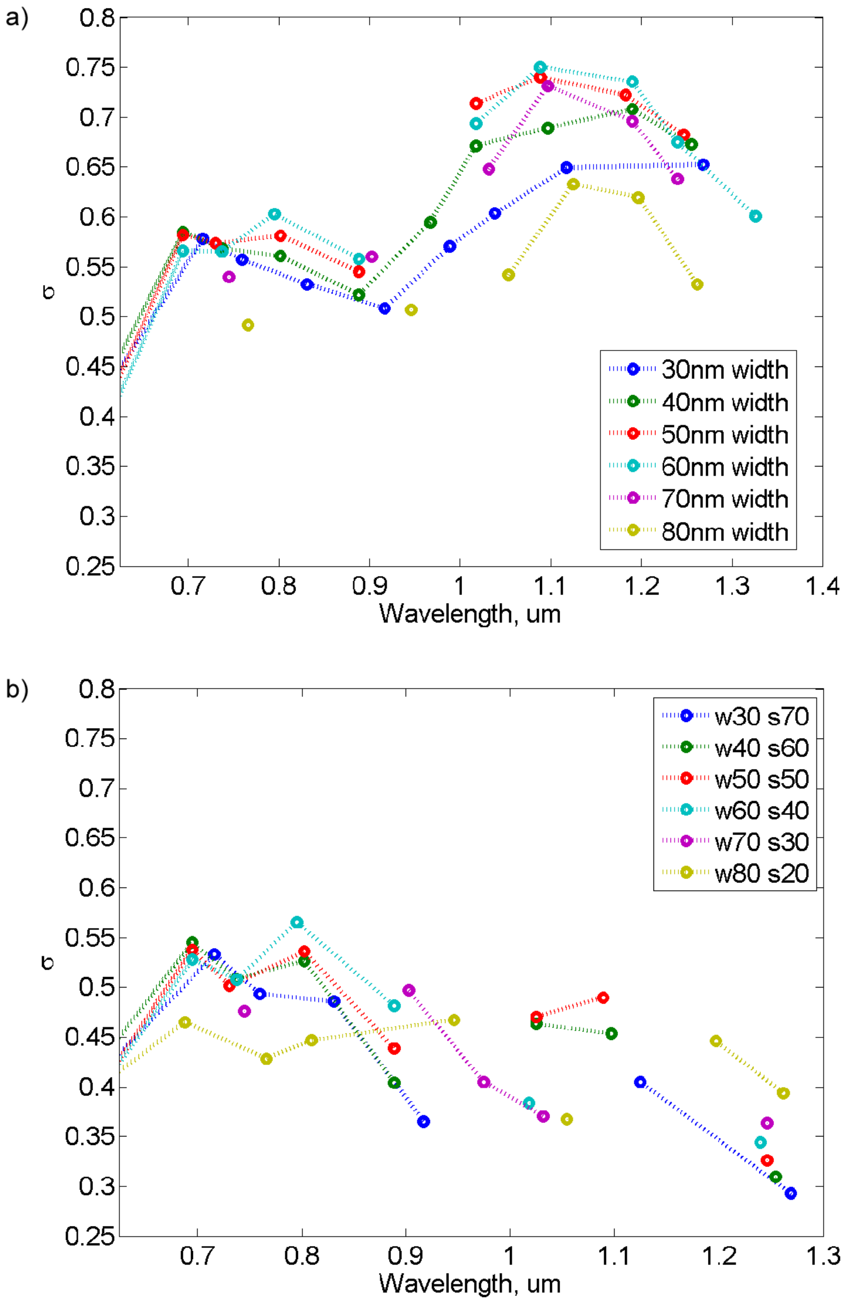

Figure 5.8: Values of σ for each resonance in a parameter sweep of 4π spirals ranging from 30nm arm width/70nm arm spacing to 80nm arm width/20nm arm spacing, with the common relation 100nm = arm width + arm spacing. Each spiral was excited by white light in the polarization state: a)RCP or b)linear aligned with the *y*-axis.

In contrast, the longer wavelength resonances reflect a must stronger chiral response. These resonances experience a reorganization that increases the preference for and the extent of focusing behavior of the NFS as compared to the linearly excited modes, as illustrated in figure 5.8. This alteration is realized by an increase in σ of ~5%, for the shortest wavelength, to a ~36%, for wavelengths past 1μm.

For resonances that have focusing behavior for linear polarizations, primarily located below 900 nm, we observed an increase in the degree of localization towards the inner 2π and a change in the magnitude of the point of maximum enhancement, which varies from a factor of 1.23 to 4. For resonances that present standing-wave behavior for linear polarizations, the modification of σ and the maximum enhancement are more drastic. These resonances switch from standing-wave or hybrid configurations to strongly focusing, with most having a σ greater than 55%. An example of this reconfiguration is illustrated in figure 5.9a, which displays the representative enhancement factors along the outer side of the 60nm width, 3nm spaced spiral for the resonance at 1.24μm for linear and right-handed circular polarizations. We note that the significant nodes located at winding numbers above 2π dwindle and the enhancements at the center increases by a factor of 3.7. Furthermore, the maximum enhancement of these resonances increases significantly. Figure 5.9b and 5.9c illustrate this trend by comparing the change in maximum enhancement for elements that exist for spirals in the geometric parameter sweep of 30-80nm width/70-20nm spacing. To clarify the magnitude of change between the similar resonances generated for both polarizations are matched by color between figures 5.9b and 5.9c. As a general trend, the longer wavelengths, which have higher

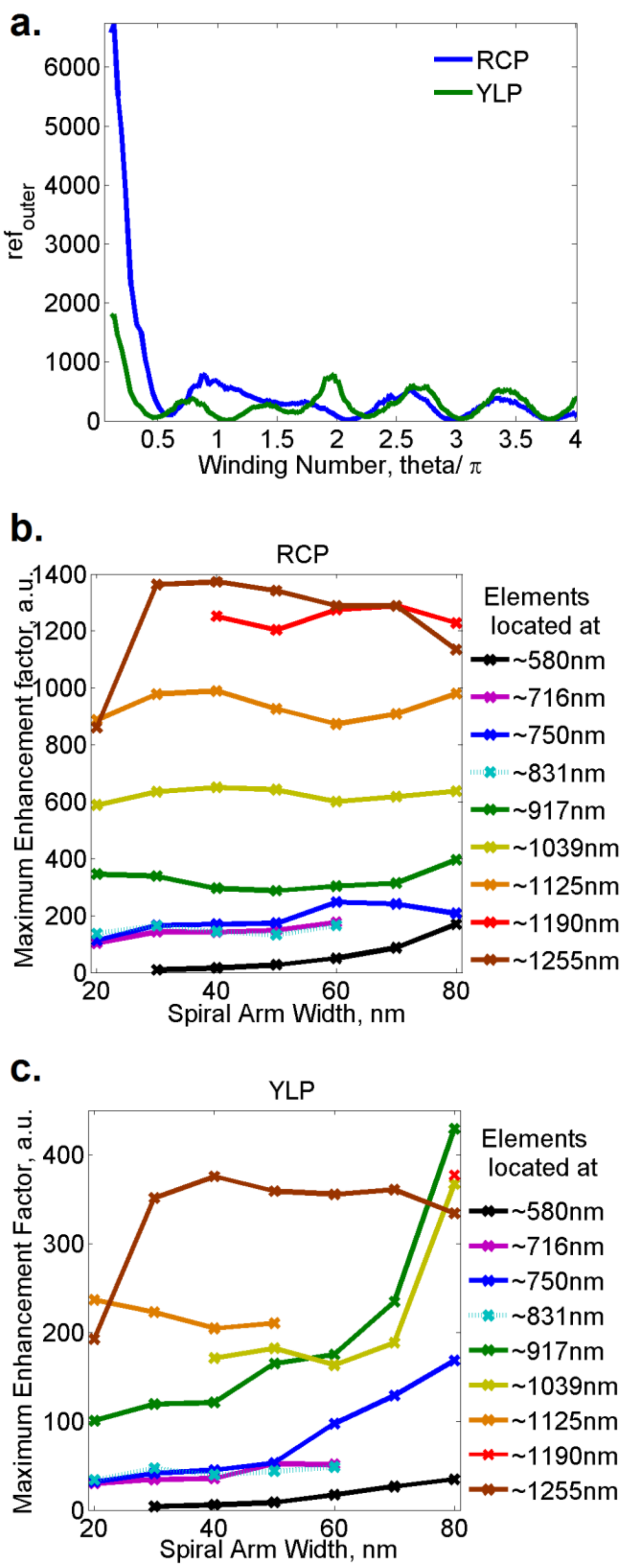

Figure 5.9: a) A line plot representing the NF structure on the outer side of the 60 nm width, 30 nm spaced spiral for the resonance at 1.24 um for linear and right-handed circular polarizations. b),c) The maximum NF enhancement for elements as a function of

the geometric parameter variation. The parameter sweep considers 4π spirals ranging from 30nm arm width/70nm arm spacing to 80nm arm width/20nm arm spacing, with the common relation 100nm = arm width + arm spacing. Each spiral was excited by white light in the polarization state: b)RCP or c)linear aligned with the *y*-axis.

maximum enhancements for linear polarizations, reflect a consistent behavior for the inward circular polarization with more significant increases in maximum enhancement.

Variation of the geometric parameters, arm width and arm spacing, do not significantly alter the focusing effect of the circular polarizations; however, when inter-arm spacing becomes low enough, the intra-particle coupling becomes more dominate and the NFS is partially dictated by this coupling. This is reflected in the far-field spectra for the lithographically fabricated spirals where the small variations in arm width and spacing result is certain resonances having greater chiral responses than displayed by the smooth, simulated spirals. Figure 5.10 illustrates an example of this behavior for the ~60nm arm width, ~30nm arm spacing spiral, in which the array excited by LCP light excites a resonance at 860nm that is dark for the RCP array and shifts the resonance around 1000nm as well as reducing the extinction coefficients for resonances at 575nm and 1179nm.

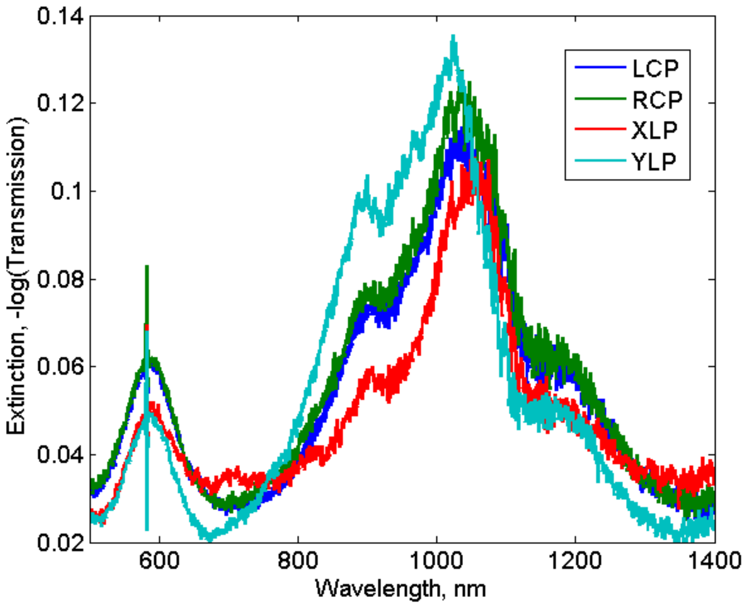

Figure 5.10: Extinction spectra from a fabricated array of 4π nanospirals with ~60 nm arm width, ~30 nm arm spacing at both circular and both orthogonal linear polarizations.

5.4 Outward circular polarization

Similar to RCP, excitation with LCP light results in an increase in total enhancement and reconfigures the NFS. However, for LCP this reconfiguration favors the standing-wave configuration with enhancement factors along the spiral arm shifting away from the central 2π. Unlike the RCP not all resonances are converted to the preferred configuration and the extent of the reconfiguration is more strongly dependent on the specific geometric parameters and wavelength. Figure 5.11 illustrates this point, where resonances below ~900nm retain some focusing behavior, though the focusing generally isn't as tight as with RCP or linear polarization, while above this limit resonances may experience a change in σ as great as 20%.

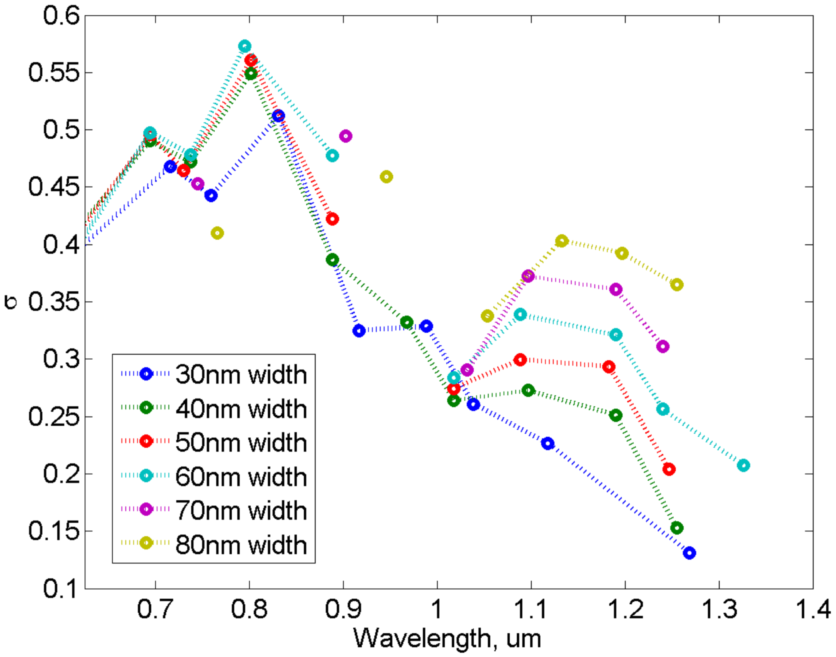

Figure 5.11: Values of σ for each resonance in a parameter sweep of 4π spirals ranging from 30nm arm width/70nm arm spacing to 80nm arm width/20nm arm spacing, with the common relation 100nm = arm width + arm spacing. Each spiral was excited by white light in the LCP state.

Similar to the RCP, LCP generates an increase in both the maximum and total enhancement compared to linear polarizations, but the significance of the increase has a much stronger correlation with geometric parameters. Using the same element grouping as in figure 5.9, figure 5.12 illustrates the dynamic range of the maximum enhancement for different elements that, in the most significant case, results in a factor of 10 increase in maximum enhancement between the most slim and the most thick spiral. As observed for all polarizations, this effect is less pronounced for shorter wavelengths.

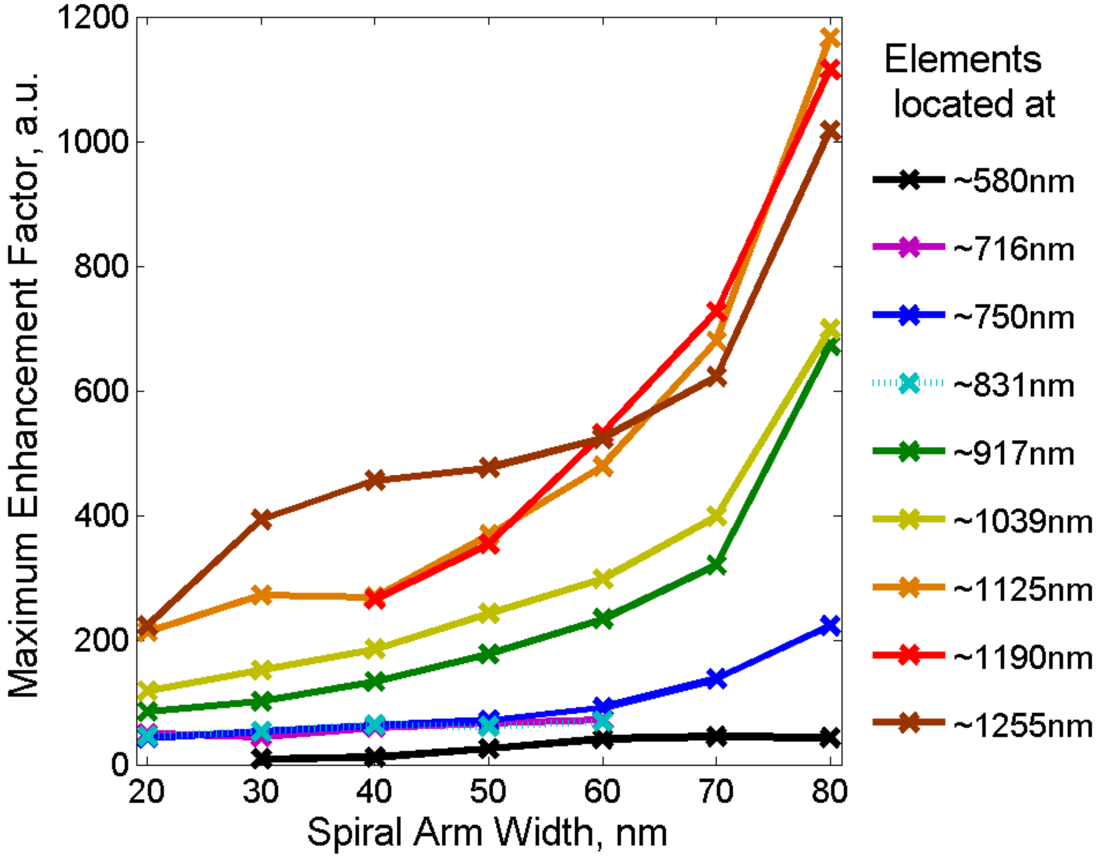

Figure 5.12: The maximum NF enhancement at each resonance, organized by elements of nanospiral arrays in the parameter sweep of 4π spirals ranging from 30nm arm width/70nm arm spacing to 80nm arm width/20nm arm spacing, with the common relation 100nm = arm width + arm spacing. Each spiral was excited by white light in the LCP state.

Furthermore, for resonances at longer wavelengths a new configuration arises, characterized by redistribution towards the outer end of the spiral. Figure 5.13 compares this new configuration to the NFS of a standing-wave configuration, which is generated by the same resonance excited by YLP, using a sum of the inner and outer arm enhancements that most distinctly illustrates the modification. The outward-oriented configuration arranges the majority of the enhancement in the region of 2π to 4π, but the placement of the enhancement points follows the organization of a standing-wave resonance. However, compared to the other characteristic configurations, this configuration is much more sensitive to internal coupling. For drawn spirals, this effect is minor but for fabricated spirals the small protrusions and variations in arm width at different winding numbers can disrupt the organization enough to make the NFS standing-wave-like. This is mostly due to the tendency for coupling within the 0 to 2π region that ensures the enhancements located in the inner region are comparable to the outer region.

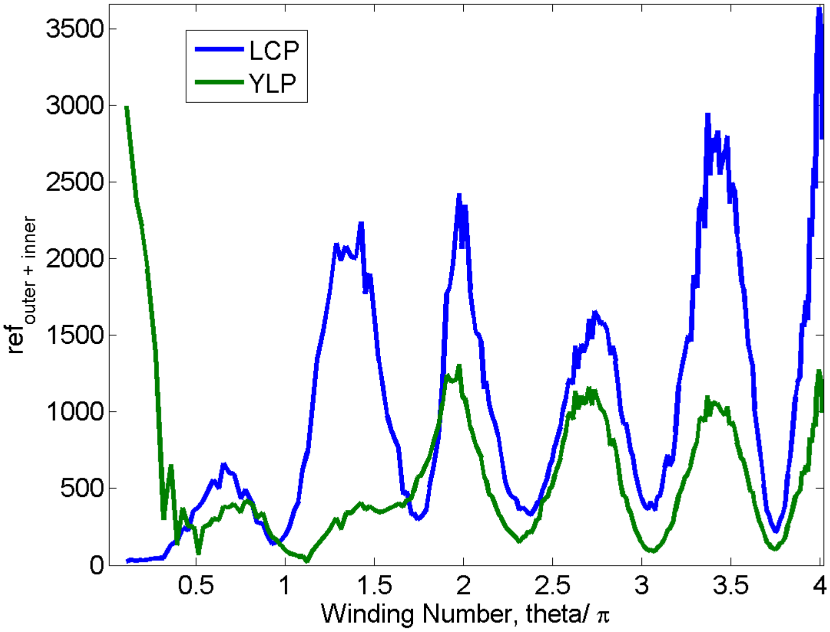

Figure 5.13: A line plot representing the sum of NF enhancement for points adjacent to the inner and outer side of the 50nm width, 50nm spaced spiral for the resonance at 1.24μm for linear, aligned to the *y*-axis, and left-handed circular polarizations.

5.5 Conclusion

In conclusion, modulation of the incident polarization presents a complete picture of the nanospiral resonances. We are able to excite all possible resonances and observe the connection between the geometric chirality of the system and its effect on the plasmonic behavior. The nanospiral exhibits a fascinating divergence between spectral behavior, where peaks remain unshifted with only differences in extinction intensity, and near-field behaviors, which significantly reorganized and vary in maximum NF enhancement. The possible reorganization and enhancement is more significant and more varied than any geometry explored to date, with the ability for NFSs to rotate, swap between characteristic configurations or reorganize to a highly enhanced version of the same configuration.

By modulating the polarization, a single, homogenous nanospiral array may be applied to multiple, techniques such as analysis of chiral molecules probing both the linear and chiral SERS response on the same structure with the same laser. Furthermore, multifunctional nanosystems present an avenue to entirely nanoscale, solid-state technologies that are capable of controlling chemical, optical and electronic behaviors all on a single particle's surface with only optical excitation. Other contemporary systems, such as those fabricated on mechanically stretchable substrates[77, 78] tunable or multilayer systems with specialize molecules[79, 80], have similar potential tunability but require complicated fabrication methods, parts which may deteriorate and macroscale control systems. The nanospiral presents a compact system with the same, or greater, complexity and tunability while following intuitive rules for manipulating the complex spectral resonances and NFSs and relatively simple fabrication methods.

CHAPTER VI

CONCLUSION AND FUTURE DIRECTIONS

6.1 Summary of characterization

The intent of this dissertation was to expand the understanding of highly complex, plasmonic geometries. The Archimedean spiral incorporates the geometric qualities of a compact, simply-connected, chiral geometry, as well as intraparticle interfaces that enrich the palette of electromagnetic near-field enhancements. As a result, it is an optimal geometry to incorporate numerous plasmonic mechanisms into a single nanostructured system. The following summarizes the major results of this research:

- The basis set of characteristic configurations of near-field (NF) enhancements was identified and defined as: *hourglass*, *focusing* and *standing-wave* configuration.
- Methods for quantitatively characterizing and studying the NF organization of nanospiral resonances were developed; including a method for visualizing and comparing multiple near-field structure (NFS) and a figure of merit to distinguish the two related configurations, focusing and standing-wave.
- The geometric parameters of the nanospiral were varied to characterize how and what resonances can be spectrally moved or extinguished and spatially reconfigured.

- The mechanisms that generate the characteristic configurations were ascertained using comparison to previously, well-characterized geometries and modulation of the polarization of the illumination source.
- The nanospiral was incorporated into ensembles with simple disks and rings to enhance specific resonances and investigate the stability of the nanospiral to perturbations from inter-particle coupling.

6.2 Initial Results For Future Work

This work focused on characterizing the nanospiral in order to illustrate the possibilities of this complex geometry, but some initial experiments were also begun to demonstrate the utility of the nanospiral for plasmonic applications. Two of these studies generated promising initial results which will be briefly reviewed.

6.2.1 Competition between resonances

Considering the complexity of the nanospiral, whose distinct NFSs organize into mutually incompatible configurations, it is possible for there to be interference between simultaneously excited resonances. Geometries with axes of symmetry are not expected to exhibit significant interference between resonances: They are either separated spectrally by polarization dependence, which allows excitation only of resonances aligned along the axis of polarization and darkens others; or they relatively comparable in spatial structure, for example, by higher harmonics of the same resonance. The nanospiral has NFSs that cannot be superimposed without significant interference and are generated by distinctly different mechanisms.

In this study, an array of fabricated nanospirals, whose extinction spectrum is displayed in figure 7.1, was excited with two sources, whose bandwidths correspond to distinct spiral resonances. Each source was composed of a tungsten lamp, a bandpass filter, and a separate optical fiber that were combined within the microscope at a beamsplitter. The bandpass filters have 40nm bandpass regions whose transmission varies from < 0.01%, out of band, to ~58%, in band. Extinction measurements were taken with the same methodology as previously described in chapter 2.

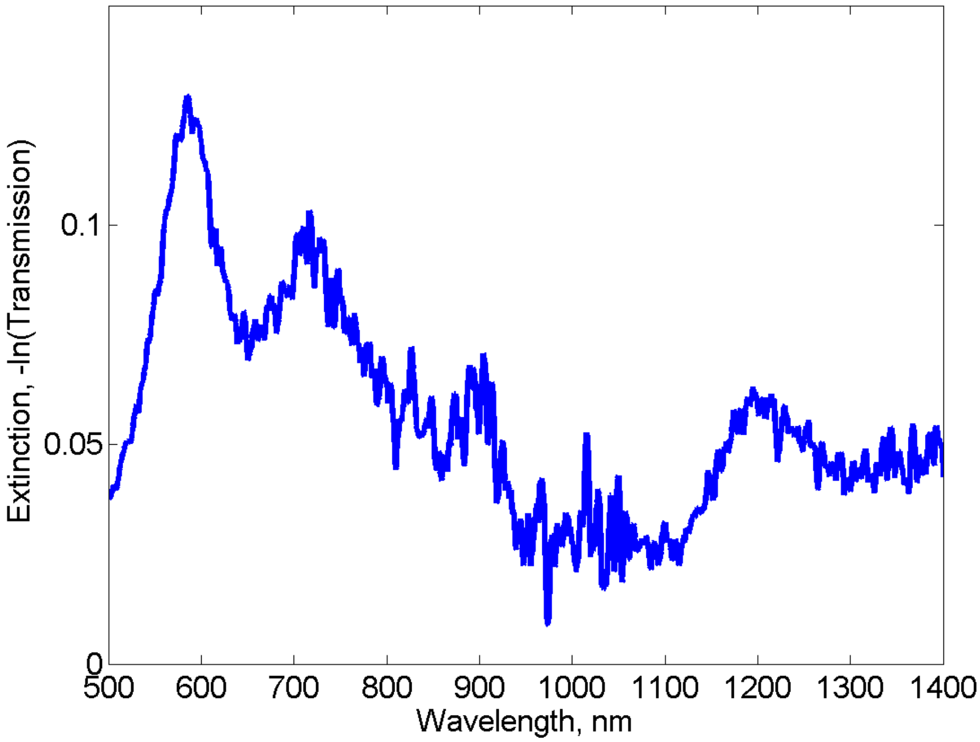

Figure 6.1: Extinction spectrum of a 4π array of nanospirals with an arm spacing of ~40nm and arm width of ~50nm.

Initial results, displayed in figure 7.2, demonstrate a variation in the maximum plasmonic extinction by as much as 20% depending on the resonance and the fiber used to excite it. In all cases, one resonance retains the same maximum extinction while the other varies. Experimental complications within the fiber coupling system and the filter system altered the spectral position of the maximum extinction and the line shape of the isolated resonances that account for the non-Gaussian peaks.

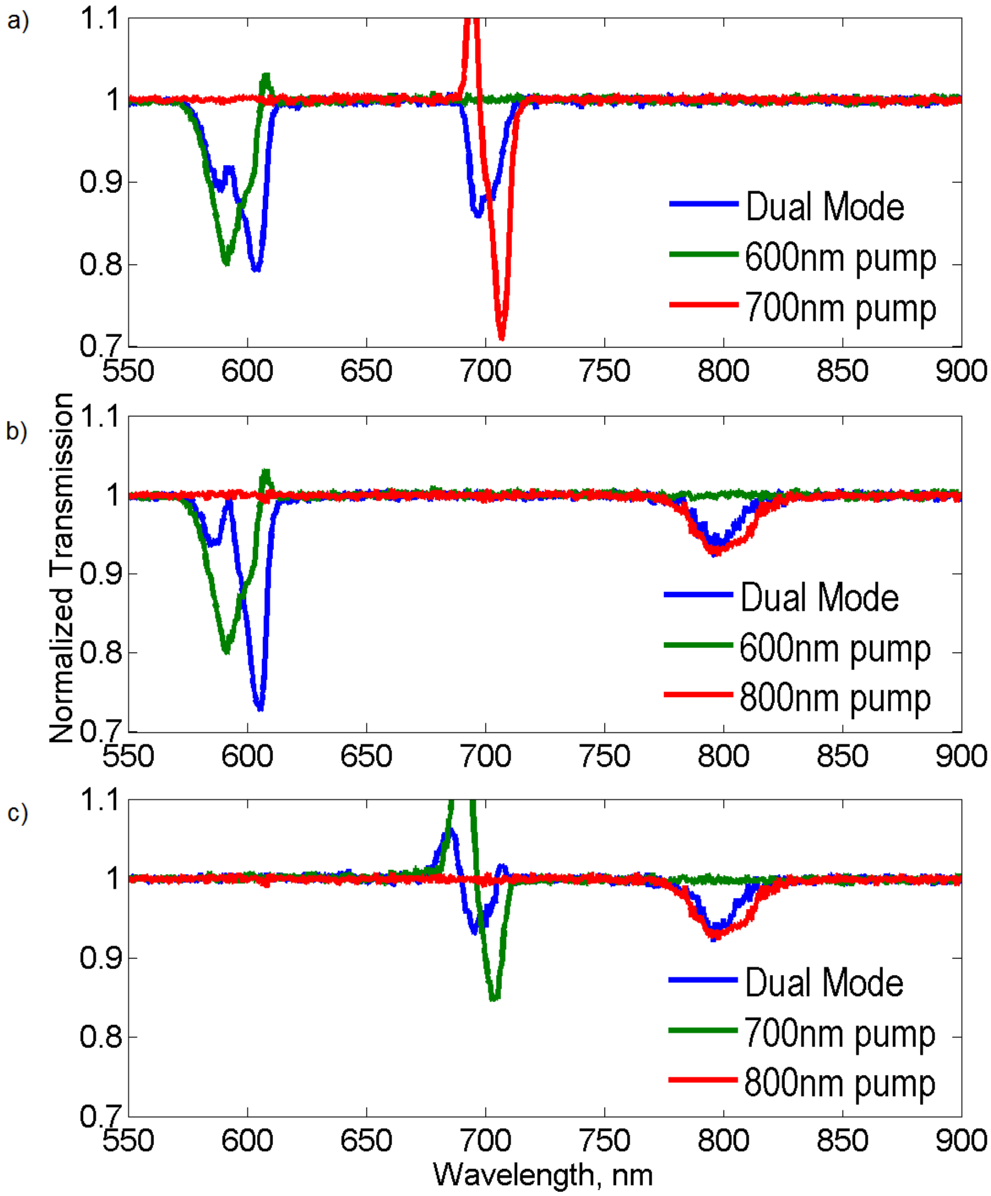

Figure 6.2: Experimental transmission spectra for an array of nanospirals, normalized with transmission through the substrate. The exciting light was polarized along the *y*-axis of the array and filtered to transmit 50nm peaks centered at 600nm, 700nm, and 800nm. Each peak is transmitted individually and collinearly with one other.

Future work can use a bifurcated fiber and a high quality, tunable filter set to eliminate the spectral shifting of the maximum extinction, and variable intensity sources can investigate the dependence of illumination intensity on the degree of extinction tunability. With this adjustment and a comparison of the dynamic plasmon oscillations from simulations, this methodology will give a clearer picture of how plasmonic resonances may compete in the restricted surface area of a nanoparticle.

6.2.2 Spatial addressing via spectral modulation

Many possible applications of the nanospiral arrays involve the incorporation of additional NPs. Chapter 6 presented the plasmonic behavior of arrays that include a second NP geometry with the nanospiral, and this line of research was expanded with initial studies of interactions between the nanospiral and non-plasmonic NPs. Altering the NF environment of a plasmonic particle with dielectric NPs can significantly alter the spectral and spatial organization. These initial investigations demonstrated the altered behavior of nanospirals when perturbed by dielectric nanodisks positioned at different locations along the spiral arm.

The disks were made to be 40nm thick and 120nm in diameter so that the 20nm thick spiral arm could be completely covered by the disk; PMMA was chosen for its well-defined material properties and its widespread use in electron beam lithography. An array of simulated nanospirals, generated by SEM images of a 4π, 70nm spaced/40nm width nanospiral, was used as a model system. Five systems were modeled with a disk of PMMA positioned at five different locations along the spiral arm. Three were aligned with the polarization of the exciting white light, which was polarized along the y-axis, at winding numbers of 0.5π, 1.5π, and 2.5π and two were aligned at 2.75π and 3.75π to consider perturbations along the outer region of the spiral of the spiral. These locations are marked on the spiral in figure 7.3.

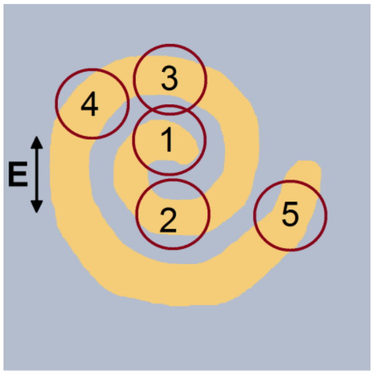

Figure 6.3: Schematic of the nanospiral with the lateral position of each nanodisk of PMMA disk and the incident polarization used for all simulations.

The extinction spectra for each physical alteration, as displayed in figure 7.4, demonstrate varied response depending on where the resonances are spectrally positioned for the unaltered nanospiral. The hourglass resonance at roughly 600 nm is not significantly altered, while the region where focusing resonances are located is highly sensitive to the presence of the PMMA, with resonances being fully extinguished or shifted, regardless of the disk location. The standing-wave resonances spectrally shift but persist, with the exception of the 2.5π position where a new resonance is generated at 1276nm. Visualization of the NFSs for these resonances shows significant changes in the enhancement values and significant enhancements at the edge of the disks, but the positions of enhanced spatial regions generally remains similar to those the unaltered nanospiral.

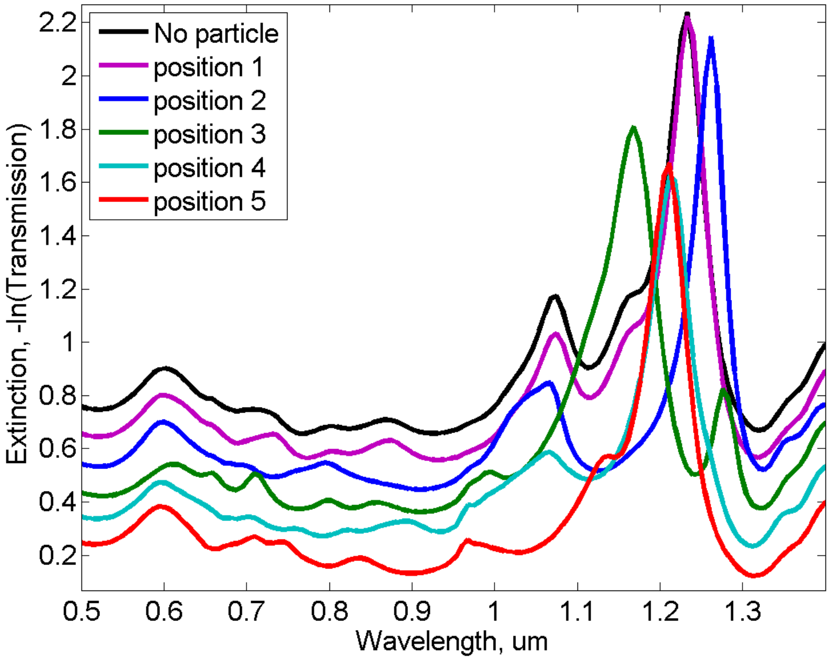

Figure 6.4: Calculated extinction spectra for nanospirals with a single PMMA nanodisk at each location specified in figure 6.3 and without a nanodisk. Each spectrum is offset by 0.1.

Further investigation is needed to characterize the specific alterations of the NFS and the parametric scope of investigation must expand to different sizes and the other positions. However, this initial work displays the promise of a spatially sensitive detector that would operate by correlating the spectral position of the long wavelength resonances, to the location of the perturbing particle. Thus the extinction spectrum of an altered nanospiral can be used as a tool to locate the position of the particle without the normal cumbersome equipment of nanoscale imaging techniques.

6.3 Outlook

Particle plasmons have proven to be one of the most exciting and technologically useful phenomena to be discovered at the nanoscale. The simplicity with which a resonance can be excited and tuned makes the PPR easy to apply to specific problems and to studies of fundamental near-field phenomena. Furthermore, the multitude of fabrication methods and the large chemical reactivities of the most popular material which generates plasmons — gold — has allowed for rapid progress in exploring the mechanisms that generate, and are generated by, plasmons. Already, plasmonic particles have been applied in biomedical devices, solar collection technologies and signal-enhancement and detection schemes in various spectroscopies.

As technology progressively reduces the size of devices, plasmonics presents one of the most promising routes to novel technologies. Applications such as optical computers, nanoscale mechanical manipulators and multistage drug delivery systems will require nanoparticles that have multiple states that can be tuned without macroscopic controllers. These requirements are currently being met with techniques such as that use exotic molecules that are bound to the NPs, quantum dots placed in close proximity and alloy NPs, but geometries and deterministically defined arrays limit the complexity of fabrication while generating widely variable behaviors and phenomenologies.

The nanospiral is an especially attractive example of the potential for specialized plasmonic geometries. It incorporates multiple tools in the form of the characteristic configurations, with logical tunability from a large range of parameters and stability to perturbations in the geometry and from neighboring systems. As more geometries in this class are discovered, the full potential of PPRs may be realized.

REFERENCES

1. Kreibig, I. and M. Vollmer, *Optical Properties of Metal Clusters*1995, Berlin: Springer-Verlag.
2. Bohren, C.F. and D.R. Huffman, *Absorption and Scattering of Light by Small Particles*1983, New York: Wiley-Interscience.
3. Knight, M.W., et al., *Substrates Matter: Influence of an Adjacent Dielectric on an Individual Plasmonic Nanoparticle.* Nano Letters, 2009. **9**(5): p. 2188-2192.
4. Johnson, R.C., et al., *Hyper-Rayleigh scattering studies of silver, copper, and platinum nanoparticle suspensions.* Chem. Phys. Lett., 2002. **356**(Copyright (C) 2011 American Chemical Society (ACS). All Rights Reserved.): p. 534-540.
5. Mie, G., *Contributions to the Optics of Turbid Media, Especially Colloidal Metal Solutions.* Ann. Phys. (Weinheim, Ger.), 1908. **25**(Copyright (C) 2011 American Chemical Society (ACS). All Rights Reserved.): p. 377-445.
6. Ung, T., L.M. Liz-Marzan, and P. Mulvaney, *Optical Properties of Thin Films of Au@SiO2 Particles.* J. Phys. Chem. B, 2001. **105**(Copyright (C) 2011 American Chemical Society (ACS). All Rights Reserved.): p. 3441-3452.
7. Prodan, E., et al., *A hybridization model for the plasmon response of complex nanostructures.* Science (Washington, DC, U. S.), 2003. **302**(Copyright (C) 2011 American Chemical Society (ACS). All Rights Reserved.): p. 419-422.
8. Nehl, C.L., et al., *Scattering spectra of single gold nanoshells.* Nano Letters, 2004. **4**(12): p. 2355-2359.
9. Hao, F., et al., *Plasmon resonances of a gold nanostar.* Nano Letters, 2007. **7**(3): p. 729-732.
10. Zoric, I., et al., *Gold, Platinum, and Aluminum Nanodisk Plasmons: Material Independence, Subradiance, and Damping Mechanisms.* Acs Nano, 2011. **5**(4): p. 2535-2546.
11. Link, S. and M.A. El-Sayed, *Spectral properties and relaxation dynamics of surface plasmon electronic oscillations in gold and silver nanodots and nanorods.* Journal of Physical Chemistry B, 1999. **103**(40): p. 8410-8426.
12. Sonnichsen, C., *Plasmons in metal nanostructures*, in *Physics*2001, Ludwig-Maximilians-University of Munich.
13. Sonnichsen, C., et al., *Drastic reduction of plasmon damping in gold nanorods.* Physical Review Letters, 2002. **88**(7).
14. Prescott, S.W. and P. Mulvaney, *Gold nanorod extinction spectra.* Journal of Applied Physics, 2006. **99**(12).
15. Verellen, N., et al., *Dark and bright localized surface plasmons in nanocrosses.* Optics Express, 2011. **19**(12): p. 11034-11051.
16. Gersten, J. and A. Nitzan, *Electromagnetic Theory of Enhanced Raman-Scattering by Molecules Adsorbed on Rough Surfaces.* Journal of Chemical Physics, 1980. **73**(7): p. 3023-3037.
17. Liao, P.F. and A. Wokaun, *Lightning Rod Effect in Surface Enhanced Raman-Scattering.* Journal of Chemical Physics, 1982. **76**(1): p. 751-752.
18. Haes, A.J., et al., *A localized surface plasmon resonance biosensor: First steps toward an assay for Alzheimer's disease.* Nano Lett., 2004. **4**(Copyright (C) 2011 American Chemical Society (ACS). All Rights Reserved.): p. 1029-1034.
19. Murray, W.A., J.R. Suckling, and W.L. Barnes, *Overlayers on Silver Nanotriangles: Field Confinement and Spectral Position of Localized Surface Plasmon Resonances.*

Nano Lett., 2006. **6**(Copyright (C) 2011 American Chemical Society (ACS). All Rights Reserved.): p. 1772-1777.

20. Felidj, N., et al., *Multipolar surface plasmon peaks on gold nanotriangles.* J. Chem. Phys., 2008. **128**(Copyright (C) 2011 American Chemical Society (ACS). All Rights Reserved.): p. 094702/1-094702/5.
21. Marty, R., et al., *Charge distribution induced inside complex plasmonic nanoparticles.* Optics Express, 2010. **18**(Copyright (C) 2011 U.S. National Library of Medicine.): p. 3035-44.
22. Hao, E. and G.C. Schatz, *Electromagnetic fields around silver nanoparticles and dimers.* Journal of Chemical Physics, 2004. **120**(1): p. 357-366.
23. Olk, P., et al., *Distance dependent spectral tuning of two coupled metal nanoparticles.* Nano Letters, 2008. **8**(4): p. 1174-1178.
24. Haynes, C.L., et al., *Nanoparticle optics: The importance of radiative dipole coupling in two-dimensional nanoparticle arrays.* Journal of Physical Chemistry B, 2003. **107**(30): p. 7337-7342.
25. Lamprecht, B., et al., *Metal nanoparticle gratings: Influence of dipolar particle interaction on the plasmon resonance.* Physical Review Letters, 2000. **84**(20): p. 4721-4724.
26. Rechberger, W., et al., *Optical properties of two interacting gold nanoparticles.* Optics Communications, 2003. **220**(1-3): p. 137-141.
27. Bouhelier, A., et al., *Electromagnetic interactions in plasmonic nanoparticle arrays.* Journal of Physical Chemistry B, 2005. **109**(8): p. 3195-3198.
28. Dahmen, C., B. Schmidt, and G. von Plessen, *Radiation damping in metal nanoparticle pairs.* Nano Letters, 2007. **7**(2): p. 318-322.
29. Jain, P.K., W. Huang, and M.A. El-Sayed, *On the Universal Scaling Behavior of the Distance Decay of Plasmon Coupling in Metal Nanoparticle Pairs: A Plasmon Ruler Equation.* Nano Lett., 2007. **7**(Copyright (C) 2011 American Chemical Society (ACS). All Rights Reserved.): p. 2080-2088.
30. Nordlander, P., et al., *Plasmon hybridizaton in nanoparticle dimers.* Nano Letters, 2004. **4**(5): p. 899-903.
31. Lassiter, J.B., et al., *Close encounters between two nanoshells.* Nano Letters, 2008. **8**(4): p. 1212-1218.
32. Yang, Z.-J., et al., *Twinned Fano interferences induced by hybridized plasmons in Au-Ag nanorod heterodimers.* Appl. Phys. Lett., 2010. **96**(Copyright (C) 2011 American Chemical Society (ACS). All Rights Reserved.): p. 131113/1-131113/3.
33. Encina, E.R. and E.A. Coronado, *Near Field Enhancement in Ag Au Nanospheres Heterodimers.* J. Phys. Chem. C, 2011. **115**(Copyright (C) 2011 American Chemical Society (ACS). All Rights Reserved.): p. 15908-15914.
34. Brown, L.V., et al., *Heterodimers: plasmonic properties of mismatched nanoparticle pairs.* Acs Nano, 2010. **4**(Copyright (C) 2011 U.S. National Library of Medicine.): p. 819-32.
35. Banaee, M.G. and K.B. Crozier, *Gold nanorings as substrates for surface-enhanced Raman scattering.* Optics Letters, 2010. **35**(5): p. 760-762.
36. Slaughter, L.S., et al., *Effects of Symmetry Breaking and Conductive Contact on the Plasmon Coupling in Gold Nanorod Dimers.* Acs Nano, 2010. **4**(8): p. 4657-4666.
37. Brown, L.V., et al., *Heterodimers: Plasmonic Properties of Mismatched Nanoparticle Pairs.* Acs Nano, 2010. **4**(2): p. 819-832.
38. Fan, J.A., et al., *Fano-like Interference in Self-Assembled Plasmonic Ouadrumer Clusters.* Nano Letters, 2010. **10**(11): p. 4680-4685.
39. Lassiter, J.B., et al., *Fano Resonances in Plasmonic Nanoclusters: Geometrical and Chemical Tunability.* Nano Letters, 2010. **10**(8): p. 3184-3189.

40. Sonnefraud, Y., et al., *Experimental Realization of Subradiant, Superradiant, and Fano Resonances in Ring/Disk Plasmonic Nanocavities.* Acs Nano, 2010. **4**(3): p. 1664-1670.
41. Li, K., M.I. Stockman, and D.J. Bergman, *Enhanced second harmonic generation in a self-similar chain of metal nanospheres.* Phys. Rev. B: Condens. Matter Mater. Phys., 2005. **72**(Copyright (C) 2011 American Chemical Society (ACS). All Rights Reserved.): p. 153401/1-153401/4.
42. Zhang, Z., et al., *Manipulating Nanoscale Light Fields with the Asymmetric Bowtie Nano-Colorsorter.* Nano Letters, 2009. **9**(12): p. 4505-4509.
43. Bergman, D.J. and M.I. Stockman, *Surface plasmon amplification by stimulated emission of radiation: Quantum generation of coherent surface plasmons in nanosystems.* Physical Review Letters, 2003. **90**(2).
44. Boriskina, S.V., et al., *Formation of colorimetric fingerprints on nano-patterned deterministic aperiodic surfaces.* Optics Express, 2010. **18**(Copyright (C) 2011 U.S. National Library of Medicine.): p. 14568-76.
45. Shugayev, R., *Surface plasmon field enhancements in deterministic aperiodic structures.* Optics Express, 2010. **18**(Copyright (C) 2011 U.S. National Library of Medicine.): p. 24946-60.
46. Trevino, J., H. Cao, and L. Dal Negro, *Circularly Symmetric Light Scattering from Nanoplasmonic Spirals.* Nano Letters, 2011. **11**(5): p. 2008-2016.
47. Pors, A., et al., *From plasmonic nanoantennas to split-ring resonators: tuning scattering strength.* Journal of the Optical Society of America B-Optical Physics, 2010. **27**(8): p. 1680-1687.
48. Clark, A.W., et al., *Tuneable visible resonances in crescent shaped nano-split-ring resonators.* Applied Physics Letters, 2007. **91**(9).
49. Nielsen, M.G., et al., *Demonstration of scattering suppression in retardation-based plasmonic nanoantennas.* Optics Express, 2010. **18**(14): p. 14802-14811.
50. Sheridan, A.K., et al., *Multiple plasmon resonances from gold nanostructures.* Applied Physics Letters, 2007. **90**(14).
51. Wang, H., et al., *Symmetry breaking in individual plasmonic nanoparticles.* Proceedings of the National Academy of Sciences of the United States of America, 2006. **103**(29): p. 10856-10860.
52. Ding, P., et al., *Tunable plasmonic properties and giant field enhancement in asymmetric double split ring arrays.* Photonics and Nanostructures - Fundamentals and Applications, 2011. **9**(1): p. 42-48.
53. Meng, T., et al., *Fabrication of metallic split-ring arrays for metamaterials using silica particle templates anchored on a silicon substrate.* Jpn. J. Appl. Phys., 2008. **47**(Copyright (C) 2011 American Chemical Society (ACS). All Rights Reserved.): p. 8109-8112.
54. Jelinek, L., R. Marques, and M.J. Freire, *Accurate modeling of split ring metamaterial lenses for magnetic resonance imaging applications.* J. Appl. Phys., 2009. **105**(Copyright (C) 2011 American Chemical Society (ACS). All Rights Reserved.): p. 024907/1-024907/10.
55. Schneider, A., et al., *Electrically excited inverse electron spin resonance in a split-ring metamaterial resonator.* Physical Review Letters, 2009. **103**(Copyright (C) 2011 U.S. National Library of Medicine.): p. 103907.
56. Powell, D.A., et al., *Metamaterial tuning by manipulation of near-field interaction.* Phys. Rev. B: Condens. Matter Mater. Phys., 2010. **82**(Copyright (C) 2011 American Chemical Society (ACS). All Rights Reserved.): p. 155128/1-155128/8.
57. Lopez, M.A., et al., *Nonlinear split-ring metamaterial slabs for magnetic resonance imaging.* Appl. Phys. Lett., 2011. **98**(Copyright (C) 2011 American Chemical Society (ACS). All Rights Reserved.): p. 133508/1-133508/3.

58. Clark, A.W., et al., *Plasmonic split-ring resonators as dichroic nanophotonic DNA biosensors.* J. Am. Chem. Soc., 2009. **131**(Copyright (C) 2011 American Chemical Society (ACS). All Rights Reserved.): p. 17615-17619.
59. Lahiri, B., et al., *Asymmetric split ring resonators for optical sensing of organic materials.* Opt. Express, 2009. **17**(Copyright (C) 2011 American Chemical Society (ACS). All Rights Reserved.): p. 1107-1115.
60. Liu, M., et al., *Light-driven nanoscale plasmonic motors.* Nature Nanotechnology, 2010. **5**(8): p. 570-573.
61. Fedotov, V.A., et al., *Asymmetric transmission of light and enantiomerically sensitive plasmon resonance in planar chiral nanostructures.* Nano Letters, 2007. **7**(7): p. 1996-1999.
62. Miao, J., et al., *Plasmonic Lens with Multiple-Turn Spiral Nano-Structures.* Plasmonics, 2011. **6**(2): p. 235-239.
63. Ohno, T. and S. Miyanishi, *Study of surface plasmon chirality induced by Archimedes' spiral grooves.* Optics Express, 2006. **14**(13): p. 6285-6290.
64. Yang, S., et al., *Miniature circular polarization analyzer with spiral plasmonic lens.* Opt. Lett., 2009. **34**(20): p. 3047-3049.
65. Drezet, A., et al., *Optical chirality without optical activity: How surface plasmons give a twist to light.* Optics Express, 2008. **16**(17): p. 12559-12570.
66. Yee, K.S., *Numerical Solution of Initial Boundary Value Problems Involving Maxwells Equations in Isotropic Media.* Ieee Transactions on Antennas and Propagation, 1966. **Ap14**(3): p. 302-&.
67. Taflove, A., *Review of the Formulation and Applications of the Finite-Difference Time-Domain Method for Numerical Modeling of Electromagnetic-Wave Interactions with Arbitrary Structures.* Wave Motion, 1988. **10**(6): p. 547-582.
68. Johnson, P.B. and R.W. Christy, *Optical constants of the noble metals.* Phys. Rev. B, 1972. **6**(Copyright (C) 2011 American Chemical Society (ACS). All Rights Reserved.): p. 4370-9.
69. Okamoto, H. and K. Imura, *Near-field imaging of optical field and plasmon wavefunctions in metal nanoparticles.* Journal of Materials Chemistry, 2006. **16**(40): p. 3920-3928.
70. Krenn, J.R., et al., *Design of multipolar plasmon excitations in silver nanoparticles.* Applied Physics Letters, 2000. **77**(21): p. 3379-3381.
71. Zou, S.L., N. Janel, and G.C. Schatz, *Silver nanoparticle array structures that produce remarkably narrow plasmon lineshapes.* Journal of Chemical Physics, 2004. **120**(23): p. 10871-10875.
72. Maier, S.A., P.G. Kik, and H.A. Atwater, *Observation of coupled plasmon-polariton modes in Au nanoparticle chain waveguides of different lengths: Estimation of waveguide loss.* Applied Physics Letters, 2002. **81**(9): p. 1714-1716.
73. Jiao, X.J., et al., *Localization of Near-Field Resonances in Bowtie Antennae: Influence of Adhesion Layers.* Plasmonics, 2009. **4**(1): p. 37-50.
74. Smolyaninov, I.I., Y.J. Hung, and C.C. Davis, *Imaging and focusing properties of plasmonic metamaterial devices.* Physical Review B, 2007. **76**(20).
75. Li, K.R., M.I. Stockman, and D.J. Bergman, *Self-similar chain of metal nanospheres as an efficient nanolens.* Physical Review Letters, 2003. **91**(22).
76. Konishi, K., et al., *Circularly Polarized Light Emission from Semiconductor Planar Chiral Nanostructures.* Physical Review Letters, 2011. **106**(5).
77. Chiang, Y., *Mechanically tunable surface plasmon resonance based on gold nanoparticles and elastic membrane polydimethylsiloxane composite.* Appl. Phys. Lett., 2010. **96**(4): p. 041904.

78. Pryce, I.M., et al., *Highly Strained Compliant Optical Metamaterials with Large Frequency Tunability*. Nano Letters, 2010. **10**(10): p. 4222-4227.
79. Smitha, S.L., et al., *Gold nanorods with finely tunable longitudinal surface plasmon resonance as SERS substrates*. Nanotechnology, 2011. **22**(26).
80. Motl, N.E., et al., *Au-Cu Alloy Nanoparticles with Tunable Compositions and Plasmonic Properties: Experimental Determination of Composition and Correlation with Theory*. Journal of Physical Chemistry C, 2010. **114**(45): p. 19263-19269.